2005

Numerical Modeling of Synthetic Jets in Quiescent Air with Moving Boundary Conditions

Nicholas D. Castro
Virginia Commonwealth University

NUMERICAL MODELING OF SYNTHETIC JETS IN QUIESCENT AIR WITH
MOVING BOUNDARY CONDITIONS

A thesis submitted in partial fulfillment of the requirements for the degree of
Master of Science in Engineering at Virginia Commonwealth University

by

NICOLAS D. CASTRO
Bachelor of Science in Mechanical Engineering, Virginia Commonwealth University,
2002

Director: KARLA MOSSI
ASSISTANT PROFESSOR, MECHANICAL ENGINEERING

Virginia Commonwealth University
Richmond, Virginia
August, 2005

Acknowledgement

I would like to thank my advisor Dr. Karla Mossi, Co-advisor Dr. Ali Rostami, member of my committee, Dr. Robert Bryant, and the entire faculty in the Department of Mechanical Engineering for all their support throughout my education and research at VCU. I would also like to acknowledge my co-workers Makram Mouhli and Byron Smith for their prompt willingness to provide me with crucial input and feedback whenever it was necessary. A special thanks to Ms. Poorna Mane who was always there to share my frustrations and achievements on a day-to-day basis whether she wanted to or not, and for the many hours she devoted to provide me with the experimental data to give this paper substance. This work would not be possible without the financial support of NASA Langley Research Center and VCU.

Table of Contents

Nomenclature

H_c Cavity Height (m)

H_o Orifice Height (m)

D_o Orifice diameter (m)

D_D Diaphragm diameter $(m$

t_D Diaphragm thickness (m)

t_{Dc} Diaphragm ceramic thickness (m)

r Radial coordinate (m)

z Axial coordinate (m)

L_o Slug Length (m)

A_D Diaphragm area (m^2)

A_o Orifice area (m^2)

$\delta(r,t)$ Diaprhagm displacement (m)

δ_C Pk-Pk diaphragm center disp. (m)

t time (sec)

Δt time step (sec)

f Actuation Frequency (Hz)

ω Radial Frequency (rad)

T Period of oscillation (sec)

u_D Diaphragm velocity (m/s)

M_c Cavity fluid mass (kg)

V_c Cavity volume (m^3)

ΔV_D .Change in diaphragm volume

$\cup$ ....Voltage (Volts)

$u_o(t)$ Jet spatial average velocity (m/s)

U_o Time averaged velocity (m/s)

$\overline{U_o}$ Spatial& time average vel (m/s)

U_{peak} Jet peak velocity (m/s)

Re   Reynolds Number

St Strouhal Number

S Stokes Number

P_b ....Diaphragm blocking pressure

P_o Ambient Pressure (N/m^2)

Π_z Axial Pressure Gradient

μ Fluid Viscosity (m^2/s)

v Kinematic Viscosity (m^2/s)

∇ Laplacian Operator

ρ Fluid density (kg/m^3)

R Gas constant (Nm/kgK)

$\delta(r,t)$ Diaphragm displacement profile

List of Figures

Abstract

NUMERICAL MODELING OF SYNTHETIC JETS IN QUIESCENT AIR
WITH MOVING BOUNDARY CONDITIONS

By Nicolas D. Castro, M.S.

A thesis submitted in partial fulfillment of the requirements for the degree of
Master of Science in Engineering at Virginia Commonwealth University

Virginia Commonwealth University, 2005

Director: Dr. Karla Mossi
Co-Advisor: Dr. Ali Rostami

Flow control is a key factor in optimizing the performance of any vehicle moving through fluids. Particularly, in aerodynamics there are many potential benefits for implementing synthetic jets to achieve aircraft designs with less moving parts, super-maneuverability, and separation control for fuel economy. Piezoelectric synthetic jets are of special interest because of their lightweight and low power consumption. Numerous publications on such jets are available. Actuator properties and boundary conditions relevant to this particular application however are often overlooked.

The focus of this project is to numerically model synthetic jets in quiescent air to study the influence of cavity geometry and boundary conditions of the piezoelectric diaphragm on jet velocity. Numerical simulation is performed for two synthetic jet cavities of different height and orifice diameter. The numerical modeling utilizes a turbulent RNG

$\kappa - \varepsilon$ model and a moving boundary condition with two oscillating deflection profiles, parabolic and logarithmic, applied to the diaphragm.

The actuators modeled are typical Bimorph and Thunder piezoelectric actuators. The initial conditions for the actuators are obtained experimentally resulting in 0.396mm and 0.07mm respectively when driven with a sinusoidal wave input at 1524 V/m and 4064 V/m. Although the velocity boundary numerical model gave overall better results than the current moving-boundary numerical model, the moving-boundary model is more accurate since it better approximates the movement of the diaphragm. From an optimizing viewpoint the moving boundary is more suitable to attempt to optimize the design because displacement magnitude of the diaphragm can be measured directly from experiments.

For the higher displacement Bimorph actuator, a logarithmic profile matches the experimental results, whereas the parabolic profile provided better results for the relatively small displacement Thunder actuator. It is thus hypothesized that both tested actuators, Bimorph and Thunder, oscillate according to the specified logarithmic and parabolic profile respectively.

Cavity height was briefly investigated for the Bimorph actuator. Results show that cavity height did not make a difference in the centerline velocity for the numerical model. The model fails to consider the important effect of the dynamic coupling of the actuator displacement and the pressure that develops inside the cavity. The pressure values obtained are comparable to the theoretical blocking pressure for the Bimorph in the cavity.

The results of this study show that jet formation and development has unique characteristics for each actuator and cavity configuration. The smaller orifice cavity

configuration produced a faster, longer, thinner jet with larger vortices than the bigger orifice. During max expulsion, t = 0.25T, and max ingestion, t = 0.75T, a low-pressure area localized at the corners of the orifice, inlet and exit respectively, were observed. All cavity configurations passed all three known jet formation criterions that include, $L_o/D_o>1$, Re > 50, and $Re/S^2 > 0.16$.

Chapter 1 Introduction

Flow control is a key factor in optimizing the performance of any vehicle moving through a fluidic medium [1]. Particularly, in aerodynamics there are many potential benefits for the implementation of synthetic jets for the purpose of flow control such as improved aircraft designs with less moving parts, super-maneuverability, longer range, increase in lift, increased payload, separation control and reduction in skin-friction drag for efficient fuel saving flight. There is still some doubt as to the exact cause of high skin friction associated with a turbulent boundary layer but recent and ongoing understanding of turbulence triggered by "hairpin" vortices and "low-speed" streaks near the wall known as coherent structures has added to the motivation behind developing synthetic jets. It is hypothesized that an array of MEMS synthetic jets can be used to interrupt or provoke coherent structures to reduce or increase turbulence. For all these reasons, synthetic jets are the focused of this project.

1.1 Synthetic Jet Background

In the past active flow control methods have included such methods as the application of steady boundary layer suction to remove low momentum fluid, wall heat transfer to modify the viscosity of the fluid, moving walls in order to use the no-slip condition at the surface to energize the fluid close to the wall, momentum addition to the boundary layer by steady blowing, and more recently oscillatory blowing and suction through synthetic jets. Although synthetic jets as flow separation control actuators have

demonstrated great potential their lack of compactness, efficiency, control authority and required power prevents them from leaving the laboratory to function in realistic full-scale conditions [2-19].

Synthetic jets are generated as a result of volumetric displacement within a fluid filled cavity due to alternate current electric field actuation of a piezo-electrically, electromagnetic or electro statically driven diaphragm. As the actuated diaphragm oscillates back and forth it alternately draws in and blows out the ambient fluid in and out of either a high aspect ratio slit or a small axisymmetric circular orifice on the cavity. The synthetic jet complete operation cycle is therefore divided into the suction part of the cycle and an ejection part of the cycle. During the suction cycle the diaphragm is moving away from the orifice drawing in ambient fluid to fill the increasing volume within the cavity. During the ejection cycle, if the impulse imparted on the fluid by the actuator moving toward the orifice is large enough, then the pressure drop developed across the orifice will cause the vortices that are created at the edges of the high aspect ratio slit or circular orifice to travel sufficiently far during the ejection cycle to escape re-entrainment during the suction cycle allowing them to escape and propagate away from the orifice due to self-induced velocity resulting in a synthetic jet with a net momentum and a zero net mass flux[2-5]. Both experimental and numerical investigations of synthetic jets have shown that during the ejection cycle the ejected fluid separates and rolls into a pair of vortices in the case of a 2-dimensional high aspect ratio slit and into a vortex ring in the case of an axisymmetric circular orifice [2-4].

Unlike traditional continuous jets or pulsed jets that require a fluid supply for net mass injection, a key trait of synthetic jets is that the fluid needed to synthesize the jet during expulsion is supplied by the intermittent suction of the same working fluid in which the synthetic jet is deployed. Synthetic jets therefore have the ability to transfer linear momentum to the surrounding ambient without the necessity of a net mass flux. Their current use includes mixing of fluids and removing heat from electronic devices such as laptops, mobile phones, telecom switches and military equipment, all of which are getting smaller with growing power demands. The use of synthetic jet blowing and suction interaction with a cross flow boundary layer over an aerodynamic surface for the purpose of aerodynamic flow control is also an application that has been looked at very closely over the last couple of years [3-19]. The zero-net-mass flux self-contained characteristic of synthetic jets means the device requires only an applied voltage for actuation making them favorable over steady or pulsed jets for flow control applications where the reduction of space and weight are of significant importance. The synthetic jet designs being investigated in this study are intended for the purpose of aerodynamic flow control applications.

Changing parameters such as the amplitude, frequency, and drive signal of the oscillating diaphragm or the orifice and cavity geometry can alter the shedding, advection and interaction of the shedding discrete vortices [2]. Zero net mass flux synthetic jets can thus be created over a large range of length and time scales with unique spatial and temporal evolution attributes not possible with steady suction or blowing that makes them appealing for various flow control applications [2-18]. Amitay and Glezer[2-4] have shown

that synthetic jets can interact with an external cross flow to displace the local streamlines to induce an apparent or virtual change on the surface to produce flow changes on length scales one to two orders of magnitude larger than the characteristic length scale of the synthetic jet. It has been experimentally and numerically established that oscillatory blowing and suction is highly effective in separation control when compared to steady or pulsed blowing and suction. Amitay et al.[4] used planar diaphragm cavity actuators to successfully control the lift and drag forces of a cylinder. They showed that the interaction of the synthetic jet resulted in a closed re-circulation region and an apparent modification to the flow boundary. When operated at a timescale well below the timescale of the base flow, they also discovered that near the surface a formation of a quasi-steady interaction domain with a favorable pressure gradient resulted in a thinner boundary layer downstream capable of overcoming larger pressure gradients that is capable of preventing or delaying separation.

1.2 Purpose of Research

The focus of this project is to numerical model synthetic jets in quiescent air to study the influence of cavity geometry and the piezoelectric diaphragm on jet velocity. Detailed information on the numerical models, methodology, geometry development, mesh generation, data acquisition, and post-processing is provided. After developing the numerical model that is validated against experimental data, the model can be used to

predict results for various conditions that are not experimentally feasible to measure. The objectives of the current research are:

1. To develop a numerical model of piezoelectric synthetic jet actuators, SJA, in quiescent air using the geometry and mesh generator GAMBIT, and numerical fluid modeling software FLUENT version 6.1.

2. Compare and validate numerical results of velocity profiles to the experimental data of various tested designs

1.3 Piezoelectric Actuators

Piezoelectricity is a property of certain classes of crystalline materials such as Rochelle Salt and Tourmaline which are natural crystals of Quartz. Piezoelectric materials can also be manufactured into ceramics such as Barium Titanate and Lead Zirconate Titanates (PZT) or plastics such as polyvinylidene fluoride (PVDF). When a mechanical pressure is applied to any of these materials, the crystalline structure produces a voltage proportional to the pressure. Conversely, when an electric field is applied, the structure changes shape producing dimensional changes in the material. Piezoelectric materials can thus be used as either an actuator or a sensor. Their applications range from simple buzzers and furnace igniters to cell phones, vibration dampening and medical imaging devices. New designs, materials, and refined fabrication process for manufacturing have improved the performance of these devices.

The constant improvement of piezoelectric technology has been advantageous for the development of synthetic jet actuators [20-24]. When compared to other conventional possible control devices such as air pumps and voice coils, the use of piezoelectric devices have the advantages of having faster response, good reliability, low cost, and a reduction in weight and space [20-24]. Chen et al.[7,8] have attained a maximum air jet velocity of approximately 40 m/sec using a 23mm diameter Murata piezoelectric type 7BB-50M-1 bonded to a 50mm diameter brass shim driven with a sine wave at a frequency of 1160 Hz. Their study shows that for limiting cases the jet velocity may be scaled by the peak-to-peak displacement of the actuator.

Studies such as the ones mentioned above and many others that utilize a sinusoidal wave drive input require relatively high frequencies to match the actuators resonance frequency or the cavity's Helmholtz frequency. Helmholtz frequency is the natural frequency that fluid tends to oscillate into and out of a container dependent on the area opening, cavity volume and length of the opening port. The high frequencies required to form a synthetic jet however consume more power and also physically limit the oscillation amplitude of the diaphragm that in turn limits the amount of air volume displaced. Furthermore the operating frequency is limited to a narrow resonance peak to give enough actuator displacement. Because of these limitations low frequency pre-stressed actuators capable of achieving large displacements at non-resonating frequencies have been the subject of this study.

The performance of three piezoelectric actuators is currently being explored by Mossi et al[21-24], they are the Bimorph, Thunder® and RFD. These actuators are similar in

that they are circular with a diameter of 6.35 cm and use the same active element, Lead Zirconate Titanate (PZT) type 5A. The geometry and overall free displacement characteristics of these piezoelectric actuators make them easy to implement into a relatively simple design. The focus of this study is based on the two actuators, Bimorph and Thunder.

The Bimorph model T216-A4NO-573X manufactured by Piezo Systems Inc., has the largest capacitance of 130nF and is 4.1 mm thick consisting of two bonded piezoelectric layers with nickel electrodes. Thunder® is a pre-stressed curved Unimorph composed of three layers that include a 0.254mm thick layer of stainless steel, a 0.254mm thick layer of PZT type 5A and a .0254 layer of perforated copper, laminated with a polyimide adhesive between each layer [21-24]. The resulting actuator, Thunder is saddle shaped with a capacitance of 80nF.

Many studies are available on synthetic jets, Bimorphs, and Thunder actuators. The next section provides an overview of the behavior and work performed on these areas.

1.3.1 Experimental Literature Review

The promising potential of piezoelectric synthetic jets for flow control has motivated researchers at various universities and governmental institutions to continue to invest time, and effort to experimentally shed insight into their functionality. Ever since the early nineties research has continued in order to characterize and understand the development and interaction of both planar and round orifice synthetic jets [3-19, 25-29]. All of

these investigations have used similar compact designs with the orifice on the surface of a rather shallow cavity in which the flow is driven by a diaphragm built into one of the cavity walls.

Amitay et al.[2-4] have by far performed the most thorough and influential early experimental studies. Using several methods such as particle imaging velocimetry, phase locked Schlieren imaging, smoke visualization and hot-wire anemometry to measure the flow field, they were able to accurately determine basic synthetic jet parameters as well as their ability to affect the cross-flow over aerodynamic surfaces. They were also able to observe the time-periodic formation, interaction and development of discrete vortices near the jet exit plane noting that the vortical structures that develop become turbulent, slow down, and lose coherence. Amitay et al.[4] also investigated the interaction between adjacent synthetic jets as well as their use for vectoring conventional jets. Their study showed that the resulting jet direction could be modified through the phase timing of synthetic jet actuation.

Zhong, et al.[29] also investigated directionality matters by performing, particle image velocimetry or PIV measurements of synthetic jets in quiescent conditions for rectangular orifices of different aspect ratios and circular orifices of different inclination angles. They found that increasing the aspect ratio initially increases the exit jet velocity. These high aspect ratio rectangular orifices initially begin as two-dimensional but quickly become three-dimensional and unstable due to "Axis Swapping" of the vortex pair between the major and minor axis. For circular orifice jets it was observed that increasing the

inclination angle also make the vortex rings less stable, resulting in a rapid reduction in axial momentum and vorticity dissipation.

The effectiveness of the synthetic jet device in most experimental studies has been maximized by driving the diaphragm and cavity at a coupled resonance that depends on both the structural characteristics of the diaphragm and the cavity geometry. As previously mentioned, the high resonant frequencies necessary constrict the operating frequency, consume more power, degrade the actuator, and also physically limit the oscillation amplitude of the diaphragm that in turn limits the amount of air volume displaced. Because of these limitations, low frequency pre-stressed actuators, capable of achieving large displacements necessary to synthesize a jet at non-resonating frequencies, have been the subject of ongoing experimental and numerical studies [3-19, 24-43].

1.3.2 Numerical Studies Literature Review

Numerical modeling can be used to readily provide data that is experimentally unavailable. An integral process for the development of functional synthetic jet numerical modes will require validation against existing experimental data. Increased numerical power and improved algorithms will also be necessary to improve CFD capability to accurately model the entirety of synthetic jet complex time dependent flows. Most numerical modeling studies of synthetic jet devices have simplified the simulation by omitting the effects of the cavity, specifying only an oscillating velocity inlet boundary condition applied at the orifice exit that is adjusted until the time-average velocity at the jet centerline is matched.

The 2004 CFD validation workshop for synthetic jets and turbulent separation control held in Williamsburg, VA [30] asked 75 researchers representative of 7 countries to attempt to model one of three cases experimentally tested at NASA Langley Research Center. These cases included: 1) synthetic jets in quiescent air, 2) synthetic jet in a turbulent boundary crossflow, and 3) flow over a hump model with no crossflow. Until this CFD workshop, most CFD validation efforts of experimental results have been and continue to be rather isolated making it difficult to accurately determine the reliability of synthetic jet CFD modeling.

For case one, synthetic jets in quiescent air, participants at the workshop were given the experimental jet velocity as a function of time near the center of the orifice exit and were granted the choice of applying arbitrary boundary conditions, grid, and method of solution to attempt to numerically reproduce the results. Since no guidelines were given regarding particular boundary conditions, grids or methods of solution to encourage broad participation it inevitably introduced a source of uncertainty when attempting to evaluate and compare the various CFD results amongst one another [30].

For the quiescent flow case believed to be mostly laminar or transitional, there were 8 participants that submitted 25 separate numerical models that included large eddy simulation (LES), reduced order models, 2D blended RANS-LES, laminar Navier Stokes and unsteady Reynolds Average Navier-Stokes (RANS). Most of the numerical cases were 2D with a few 3D models that used periodicity in the direction aligned with the slot's long axis. The vast majority of participants simulated the diaphragm motion via a transpiration condition imposed on the diaphragms neutral surface. A transpiration condition is one that

applies either an assumed oscillating fluid velocity profile or pressure oscillation to emulate the effects of the oscillating diaphragm within the cavity. Others participants further simplified the cavity by imposing a transpiration condition not at the neutral surface but at the bottom of the slit's neck or directly on the slit's exit, thus neglecting the effects of the cavity itself. In this current study the entire cavity is modeled with an oscillating boundary condition for the actuator.

Results of the workshop showed significant variation among the proposed CFD techniques and established that no one method in particular clearly excelled above the others. It was also established that there are still inconsistencies not only with the numerical models but also between the different experimental time-dependent flow measurement techniques, Particle Image Velocimetry (PIV), hot-wire probes, and Laser Doppler Velocimetry (LDV). The greatest variation in the experimental measurements was mostly attributed to the piezoelectric diaphragms observed performance time degradation, which further complicated validation of the various CFD models.

In this study, the piezoelectric diaphragm experimental performance is coupled with the CFD code to reduce variations due to the diaphragm itself. Numerical and experimental results are merged in this work as described in the following section.

1.4 Scope of the thesis

An introduction and a literature review of the characteristics, flow control potential, and basic fluid dynamic of synthetic jet actuators is presented in chapter one. Next, chapter two deals with the governing parameters and formulation of synthetic jets. It also considers the modeling of each of the components that comprise the device, diaphragm, cavity and

orifice. An analysis of the numerical model developed and the parameters used for simulations are discussed and presented in chapter three. It furthermore presents the details of the tested experimental models and the development of the numerical mesh for each case. A discussion of the numerical results and comparison with experimental measurements is presented in chapter 4. Finally, Chapter 5 consists of the summary and conclusions from this study and recommendations for future studies.

Chapter 2 Synthetic Jet Components and Formulation

2.1 Diaphragm

The electrostictive induced diaphragm motion is the forcing mechanism in piezoelectric actuators. Extensive work in the area of modeling piezoelectric composite circular plates has been mainly on bimorph actuators that contain layers that are symmetrical about the midplane and thus have no bending-extension coupling. Suryanarayana et al.[44] have used classical laminated plate theory to derive the equations of equilibrium for circular laminated plates composed with one or more transversely isotropic piezoelectric layers via lumped-element modeling. The model for a piezoelectric Unimorph® actuator developed by Suryanarayana et al.[44] provides a reasonable prediction of the first resonant frequency of the actuator.

Successful CFD synthetic jet flow fields and prediction simulations that incorporate the oscillating piezoelectric diaphragms actuators' performances will depend heavily on accurate approximation of the oscillating diaphragm's displacement profile, including the instantaneous deflections and shape mode. One of the earliest studies by Rathnasingham and Breuer[41] modeled the oscillating diaphragm as a simple rigid piston to approximate volumetric changes in the cavity without considering the actual temporal and spatial displacement profile of the oscillating diaphragm. This approach does not guarantee an accurate description of the instantaneous volumetric changes.

The deflection mode and amplitude of the diaphragms displacement at a given instant may have an effect on the amount of fluid volume displaced which determines the

pressure gradient that is developed to affect the details of the instantaneous flow field through the orifice and the formation of the synthetic jet.

2.1.1 Experimental Determination of the Diaphragm Displacement

Peak-to-peak displacement of the actuators clamped on a cavity and driven by a sinusoidal wave is experimentally measured. These values are used on the numerical simulations as an input. The equipment utilized in the experiments included a 9350L LeCroy oscilloscope, PZD700 TREK amplifier with a feedback damping system, HP33120 signal generator, and a dual channel Angstrom Resolver model 201R with a fiber optic sensor. The output voltage from the Angstrom Resolver and the amplifier were monitored with the oscilloscope that is controlled through a PC equipped with a National Instruments data acquisition card that allows the data to be recorded using LabView® software

The cavity housing 8.89 x 8.89 x 1.91 cm, was composed of two identical rectangular plastic pieces that have a 0.318 cm deep circular groove with a circular aperture as shown in Figures 1a and 1b.
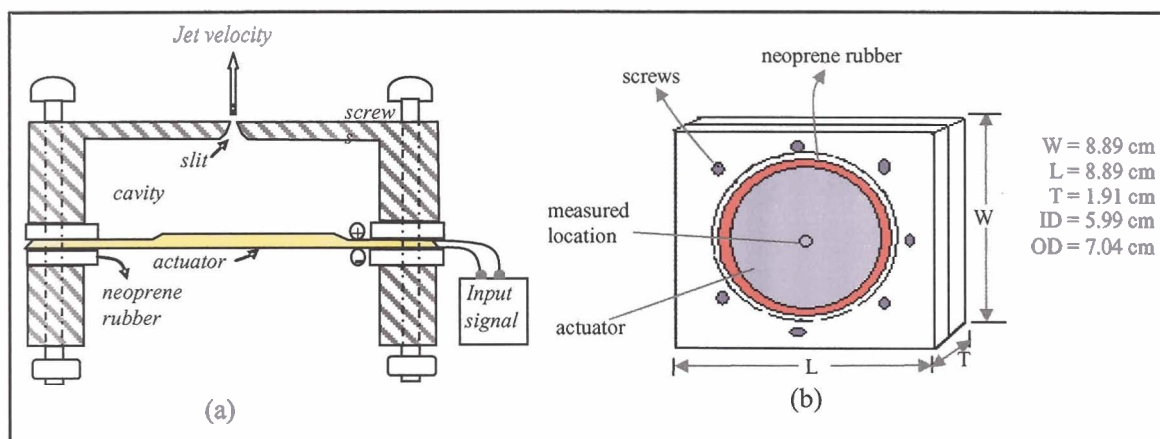
Figure 1 Synthetic Jet Cavity, (b) Posterior View of the Synthetic Jet Cavity

The actuator was placed between the described pieces with neoprene rubber around the perimeter of the actuator on either side. Seven 0.318 cm screws hold the two plastic pieces together and clamp the actuator in place. The assembled cavity was mounted onto an adjustable height gauge with the actuator's surface perpendicular to the fiber optic sensor used to measure displacement at the indicated location.

An AC electric field of 1524 V/m and 4064 V/m peak-to-peak was applied to the Bimorph and Thunder respectively. For the two model actuators, Bimorph and Thunder the peak-to-peak center amplitudes, δ_C ,are 0.396mm and 0.07mm respectively.

2.1.2 Numerical Diaphragm Boundary Conditions

In this study the instantaneous oscillatory motion profile due to a sinusoidal wave input signal as a function of time and radial position, $\delta(r\ t)$, is approximated by a logarithmic profile and a parabolic profile. It is known that the two actuators, Bimorph and Thunder have a zero peak-to-peak displacement around their perimeter where they are clamped and a maximum peak-to-peak displacement at their center. Both profiles chosen thus have a zero displacement boundary condition at the perimeter of the oscillating diaphragm and a maximum peak-to-peak deflection to match the experimentally measured displacement at the center of the diaphragm.

The current two-dimensional model does not take into account asymmetry that is likely to occur in three dimensions especially for the odd shaped Thunder actuator. Both profiles chosen thus serve as a first step approximation of the actuators movement.

Without accurate spatial and temporal experimental data for the description of the entire actuator, the logarithmic profile is a good approximation. Tang and Zhong[45] applied the same profile to a piezoelectric actuator with a thin steel shim, but as a transpiration velocity input condition on the neutral position of the diaphragm and not as a moving wall boundary condition as is done in the present study. Furthermore the logarithmic profile is a well known profile derived from the theory of plates and shells [46].

For the logarithmic profile the instantaneous displacement is shown below by equation 1.

$$\delta(r,t) = \frac{\delta_C}{2}\left[1 - \frac{4r^2}{D_D^2} + \frac{8r^2}{D_D^2}\ln\left(\frac{2r}{D_D}\right)\right]\sin(2\pi f t) \qquad \text{Equation 1}$$

Where δ_C is the diaphragm center peak-to-peak displacement, r is the radial distance from the center of the diaphragm, D_D is the diaphragm diameter and f is the actuation frequency. Differentiating equation 1 to obtain the instantaneous logarithmic diaphragm velocity,

$$u(r,t) = \pi\delta_C f\left[1 - \frac{4r^2}{D_c^2} + \frac{8r^2}{D_c^2}\ln\left(\frac{2r}{D_c}\right)\right]\cos(2\pi f t) \qquad \text{Equation 2}$$

For the parabolic profile the instantaneous displacement is described by equation 3.

$$\delta(r,t) = \left[\int u(t) - \int u(t) \left(\frac{r}{(D_D/2)} \right)^2 \right] \qquad \text{Equation 3}$$

Where the time dependent velocity is $u(t) = f\pi\delta_C \cos(2\pi f t)$. Differentiating we obtain the instantaneous parabolic velocity.

$$u(r,t) = \left[u(t) - u(t) \left(\frac{r}{(D_D/2)} \right)^2 \right] \qquad \text{Equation 4}$$

Although the two displacement profiles in this study, logarithmic and parabolic described by equations 2 and 4 serve as a fairly accurate approximation of the actuators movement, a complete description of the vibration modes of these diaphragms may be required. Coupling with finite element analysis models may be necessary to accurately predict the displacement of these devices especially if they are subjected to pressure fluctuations inside the cavity. Furthermore, the initial shape of the actuators is very complex and models like the one proposed by Hyer and Shultz[21] are still under development and many times under-predicts the devices performance.

With the diaphragms motion described, next the physical characteristics of the cavity can be defined.

2.2 Cavity

Most numerical studies simplify synthetic jet modeling by neglecting diaphragm and cavity interactions effects by applying a prescribed oscillating velocity or pressure boundary condition either at the orifice inlet or at the orifice exit [30]. The approach utilized

on these models involves specifying the velocity or pressure boundary conditions so as to match the measured centerline jet velocity. According to Rizzeta et al.[43] however, significant differences in velocity time history at the centerline could occur when the cavity flow and its effects are neglected.

The variables involved when considering the cavity are the fluid volume and mass within the cavity. With the equation of state the pressure variations within the cavity due to density changes is given by equation 5.

$$P_c = \rho_c R T_c \qquad \qquad \text{Equation 5}$$

Where R is the gas constant, T_c is the cavity temperature, and ρ_c is the density in the cavity given by

$$\rho_c = \frac{M_c}{V_c} \qquad \qquad \text{Equation 6}$$

The oscillating diaphragm profile determines the evolution of the cavity volume, V_c, while the mass of fluid, M_c, in the cavity is governed by the mass conservation relationship.

$$\frac{dM_c}{dt} = \dot{M}_{out} - \dot{M}_{in} \qquad \qquad \text{Equation 7}$$

Where $\dot{M}_{out}$, is the mass flow rate across the orifice. Neglecting particle motion and assuming a static cavity, where fluid inside the cavity is not dynamically compressive (i.e. density and pressure variations are felt uniformly and instantaneously) the mass flow rate out and volumetric changes in integral form are respectively expressed as follows

$$\frac{dM_c}{dt} = \dot{M}_{out} = -\rho_1 \int_{A_o} u_1 dA \qquad \text{Equation 8}$$

$$\frac{dV_c}{dt} = -\int_{A_d} u(r,t) dA \qquad \text{Equation 9}$$

Where the subscript '1' signifies values at the cavity orifice interface and $u(r,t)$ is the diaphragm velocity.

The next section shows how the pressure fluctuations in the cavity create a pressure gradient across the orifice.

2.3 Orifice

2.3.1 Orifice Parameters and Analytical Solution

The pressure fluctuations in and out of the cavity caused by the diaphragms oscillatory volumetric fluid displacement creates a pressure gradient across the orifice that drives the fluid to form a jet. Rathnasingham and Breuer[41] approximated the orifice flow

using the one-dimensional inviscid unsteady Bernoulli equation while Crook et al.[9]

modeled the orifice flow using a quasi-steady Poiseuille (incompressible laminar flow)

solution. Both of these models are highly simplified approximations. A complete solution

would involve solving the entire three dimensional, unsteady, viscous, and compressible

Navier–Stokes equations in the orifice as well as the cavity at every time step. This type of

accurate modeling would require excessive numerical power that is not economically and

computationally feasible when considering that ultimately the synthetic jet flow will have

to be coupled to a cross flow boundary layer. It is thus inevitable to have to make certain

approximations to the Navier–Stokes equations. In deriving the analytical orifice solution

presented in this paper the following approximations are made: (1) Parallel flow out the

orifice (velocity in z direction only); (2) Fluid is isothermal and Newtonian; (3) The flow is

laminar and steady; (4) One dimensionality similar to incompressibility by assuming linear

density, pressure and boundary conditions that vary with axial (z) direction only.

With the proposed assumptions the continuity and momentum equations are

expressed as.

$$\text{Continuity: } \frac{\partial \rho}{\partial t} + \frac{\partial (\rho u^2)}{\partial z} = 0 \qquad\qquad \text{Equation 10}$$

$$\text{Momentum: } \frac{\partial (\rho u)}{\partial t} + \frac{\partial (\rho u^2)}{\partial z} = -\frac{\partial (p)}{\partial x} + \mu \nabla^2 u \qquad \text{Equation 11}$$

Where, ρ is the fluid density, μ is the viscosity of the fluid, P is the pressure and ∇ is the

Laplacian Operator defined in equation 12 for cylindrical coordinates as

$$\nabla^2 \equiv \left[\frac{1}{r}\frac{\partial}{\partial r} + \frac{\partial^2}{\partial r^2} \right]$$
Equation 12

Combining the continuity equation (10) and momentum equation (11) to obtain.

$$\rho\frac{\partial u}{\partial t} + \rho u\frac{\partial u}{\partial z} = -\frac{\partial p}{\partial z} + \mu\nabla^2 u$$
Equation 13

The velocity, density, and pressure are defined linearly to simplify the combined

equation (13) of the continuity and momentum equation.

$$u = u_1 + \frac{z}{H_o}(u_2 - u_1)$$
Equation 14

$$\rho = \rho_1 + \frac{z}{H_o}(\rho_2 - \rho_1)$$
Equation 15

$$p = p_1 + \frac{z}{H_o}(p_2 - p_1)$$
Equation 16

Where H_o, is the depth of the orifice and the subscripts '1' and '2' refers to values inside

and outside the cavity respectively. Evaluating equation 13 at z = 0 yields a one-

dimensional equation with only velocities $u_1(r,t)$ and $u_2(r,t)$ as unknowns since pressure and density values are known boundary conditions.

$$\rho_1 \frac{\partial u_1}{\partial t} + \frac{\rho_1 u_1 (u_2 - u_1)}{H_o} = -\frac{p_1 - p_2}{H_o} + \mu \nabla^2 u_1 \qquad \text{Equation 17}$$

Integrating the continuity equation with respect to z over the length of the orifice we get an expression for u_2 in terms of u_1.

$$u_2 = \frac{\rho_1 u_1}{\rho_2} - \frac{H_o}{2\rho_2} \frac{\partial \rho_1}{\partial t} \qquad \text{Equation 18}$$

The density at 2 is constant with respect to time since there are no compressible flow effects outside the cavity. Substituting equation 18 into equation 13 we can express the Navier Stokes equation as:

$$\underbrace{\frac{\partial u_1}{\partial t}}_{} + \underbrace{\left(\frac{\rho_1}{\rho_2} - 1 \right) \frac{u_1^2}{H_o}}_{} - \underbrace{\frac{u_1}{2\rho_2} \frac{\partial \rho_1}{\partial t}}_{} = \underbrace{\frac{p_1 - p_2}{H_o \rho_1}}_{} + \underbrace{\frac{\mu}{\rho_1} \nabla^2 u_1}_{} \quad \text{Equation 19}$$

Terms: I   II   III   IV   V

Where the terms in equation 19 are as follows:
   I.   Inertial term—accounts for temporal unsteadiness
   II. Nonlinear damping term—expansion and compression of fluid
   III. Nonlinear damping term—time dependent compression of fluid inside the cavity.

IV. Forcing term—Pressure gradient

V. Linear damping term—source of viscous resistance

2.3.2 Orifice Numerical Solution

This section of the report includes the details of the orifice flow solution to equation 19 derived in the previous section and the boundary conditions used for the problem including the inlet velocity profile.

Neglecting the nonlinear terms (II and III), an implicit solution to the orifice equation is attained by evaluating between new, u^{n+1}, and current, u^n, time step that results in the form shown in Equation 20.

$$\left(\frac{1}{\Delta t} - \frac{\mu}{2\bar{\rho}_1} \nabla^2 \right) u^{n+1} = \frac{\bar{p}_1 - \bar{p}_2}{l\bar{\rho}_1} + \left(\frac{1}{\Delta t} - \frac{\mu}{2\bar{\rho}_1} \nabla^2 \right) u^n \quad \text{Equation 20}$$

Where a bar over a variable expresses the mean value between n and $n+1$. The Laplacian operator, ∇^2, defined in equation 12 can be approximated using centered difference.

$$\nabla^2 \Delta u_i = \left(\frac{1}{r} \frac{\partial}{\partial r} + \frac{\partial^2}{\partial r^2} \right) \Delta u_i = \frac{\Delta u_{i+1} - \Delta u_{i-1}}{2r\Delta r} + \frac{\Delta u_{i+1} + \Delta u_{i-1} - 2\Delta u_i}{\Delta r^2} \quad \text{Equation 21}$$

The resulting set of equations that result for equation 20 can be put into tri-diagonal form and solved using the tri-diagonal matrix algorithm known as the Thomas algorithm that efficiently uses an order of m operations to forward multiply an $(m \times m)$ tri-diagonal matrix.

Inclusion of the nonlinear terms complicates the solution for the orifice flow by preventing organization of the equations into tri-diagonal form. In order to deal with this problem the values in equation (3.18) are expressed with the addition of incremental values,

$$u_i^{n+1} = u_i^n + \Delta u_i \qquad \text{Equation 22}$$

Where i, is the radial grid point and Δu, is an increment value. The advantage of expressing values at the new time step in this manner is that Δu^2 terms will have magnitudes in order of truncation error that can be neglected. Evaluating the orifice equation at $t = t^n + \Delta t / 2$ gives the numerical approximation in incremental form:

$$\left(\frac{1}{\Delta t} - \frac{1}{4\rho_2} \frac{\overline{\partial \rho_1}}{\partial t} + \left(\frac{\overline{\rho_1}}{\overline{\rho_2}} - 1 \right) \frac{u_1}{l} - \frac{\mu}{2\overline{\rho_1}} \nabla^2 \right) \Delta u_i = \frac{\overline{p_1} - \overline{p_2}}{l\overline{\rho_1}} + \left(\frac{1}{2\rho_2} \frac{\overline{\partial \rho_1}}{\partial t} - \left(\frac{\overline{\rho_1}}{\overline{\rho_2}} - 1 \right) \frac{u_1}{l} + \frac{\mu}{\overline{\rho_1}} \nabla^2 \right) u_i$$

Equation 23

The Laplacian operator in equation 12 and equation 23 can be put into tri-diagonal form and solved using a Thomas algorithm. In order to describe the pertinent boundary conditions the radial points are defined as:

$$r = \frac{(i-1)R}{(N-1)} \quad \textit{For } i = 1 \textit{ to } N \qquad \text{Equation 24}$$

Where N corresponds to the radial point at the wall. The two boundary conditions for the orifice are:

1. No slip condition; zero velocity at wall

$$u_N = 0$$

2. Radial symmetry at the center of the orifice (von Neumann condition) is enforced using Taylor series expansion (near center of orifice r=0) shown below for velocity.

$$u(\Delta) = u(0) + \Delta u'(0) + \frac{\Delta^2}{2} u''(0) + \frac{\Delta^3}{6} u'''(0) + \vartheta(\Delta^4) \qquad \text{Equation 25}$$

$$u(2\Delta) = u(0) + 2\Delta u'(0) + 2\Delta^2 u''(0) + \frac{8\Delta^3}{6} u'''(0) + \vartheta(\Delta^4) \qquad \text{Equation 26}$$

Where Δ, is the radial grid spacing. Imposing symmetry condition at r = 0.

$$u'(0) = u'''(0) = 0 \qquad \text{Equation 27}$$

We can combine equations 25 and 26 to give

$$u(0) = \frac{4}{3} u(\Delta) - \frac{1}{3} u(2\Delta) + \vartheta(\Delta^4) \qquad \text{Equation 28}$$

Which can be expressed as a boundary condition on velocity

$$u_1 - \frac{4}{3}u_2 + \frac{1}{3}u_3 = 0 \qquad\qquad \text{Equation 29}$$

Incorporation of this boundary condition with the centered approximation for the Laplacian operator center difference approximation and equation 23 can be combined to produce an off tri-diagonal matrix that can be modified by appropriate factorization to recover a desired tri-diagonal form to be solved with Thomas' algorithm.

2.4 Governing Parameters

Two dimensionless parameters govern both axisymmetric and two-dimensional slot synthetic jets. These parameters are the Reynolds number, Re, and the dimensionless stroke length, L_o / D_0, based on what has been termed the "slug model" [2-4], where L_o is the distance that a "slug" of fluid travels during the ejection stroke which is half the time period defined as

$$L_o = \frac{1}{D_o} \int_0^{T/2} u_o(t)\,dt \qquad\qquad \text{Equation 30}$$

In the experimental study by Smith and Swift[17] it was determined that for a given geometry there exists a minimum dimensionless stroke length, $L_o / D_o = U_o /(fD_o)$, below which no jet is formed. The time average velocity, U_0, during the ejection cycle is related to the frequency f, and slug length L_o by,

$$U_o = fL_o = f \int_0^{T/2} u_o(t)dt \qquad \text{Equation 31}$$

Where $T = 1/f$ is the period, D_o is the width of the 2D slit or the diameter of an axisymmetric circular orifice, and $u_o(t)$ is the spatial averaged velocity at the exit. Using the time averaged velocity the Reynolds number is defined as,

$$\text{Re} = \frac{U_o D_o}{\nu} \qquad \text{Equation 32}$$

Where ν is the kinematic viscosity. The Reynolds number can also be defined in terms of the spatial and time-averaged exit velocity, $\overline{U}$, during the expulsion stroke defined as,

$$\overline{U} = \frac{2}{T} \frac{1}{A_o} \int_{A_o} \int_0^{T/2} u_o(t,r)dtdA = 2U_0 \qquad \text{Equation 33}$$

Where A_o, is the orifice exit area and r, is the cross stream radial coordinate. It can be seen that the dimensionless stroke length, L_o/D_o, is closely related to the inverse of the Strouhal number, St, which as seen in equation 34 is equivalent to the Reynolds number divided by the Stokes number, S, squared.

$$\frac{1}{St} = \frac{\overline{U}}{\omega D_o} = \frac{\overline{U} D_o / v}{\omega D_o^2 / v} = \frac{\text{Re}}{S^2} \qquad\qquad \text{Equation 34}$$

Where $\omega = 2\pi f$ is the radian frequency of oscillation of the diaphragm and the Stokes

number, S, is defined as,

$$S = \sqrt{\frac{\omega D_o^2}{v}} \qquad\qquad \text{Equation 35}$$

Using these parameters, Utturkar et al.[32] derived a synthetic jet formation criterion

through an order of magnitude analysis with the premise that a jet forms if the induced

velocity of the vortices is larger than the suction velocity and with the assumption of a

sinusoidally varying exit velocity profile of the following form

$$u = u_0 \sin(\omega t) f(r) \qquad\qquad \text{Equation 36}$$

Where $f\left(r = |d/2|\right) = 0$ (no slip at the walls), and $f\left(r = |0|\right) = 1$ at the center of the orifice.

The derived jet formation criterion of Utturkar et al.[32] is applicable to relatively thick

orifice plates $(H_o/D_o > 2)$ that satisfy the assumption of nearly fully developed orifice flow

and is determined by the condition

$$\frac{\text{Re}}{S^2} > \frac{K'}{N^2}$$ Equation 37

Where K' is a constant and N is defined as

$$N = \frac{u_o}{\overline{U}}$$ Equation 38

It was concluded by Utturkar et al.[32] that the jet formation criterion for an axisymmetric orifice and two-dimensional slot defined respectively by equations 39 and 40 as,

$$\text{Re}/S^2 > 0.16 \text{ Axisymmetric}$$ Equation 39

$$\text{Re}/S^2 > 2 \text{ Two-dimensional}$$ Equation 40

The resulting equations, 37 and 38, show that the jet formation criterion is dependent on the velocity profile. Since a velocity profile is assumed to be completely in phase across the orifice this approximation is only valid at low Stokes numbers when the velocity profile is parabolic. For an axisymmetric orifice and two-dimensional slot, N was found to be equal to 2 and 1.5 respectively. The higher N axisymmetric orifice value means that a jet will form at lower Reynolds number than a two-dimensional slot orifice.

To verify the accuracy of the jet formation criterion derivation, Utturkar et al. [32] proceeded to numerically model the synthetic jet geometry that was inclusive of the cavity

and moving diaphragm on a stationary Cartesian mesh over a range of Reynolds and Stokes number with an oscillating diaphragm boundary condition. The numerical results determined a constant of $K = 1$. Data from Smith and Swift[18] was then converted to Reynolds and stokes number and showed good agreement with the jet formation criterion established of $Re/S^2 > 2$ for axisymmetric jets. Calculations of the Reynolds number, Strouhal number and Stokes number of the current synthetic jet numerical models will be presented in the results to further verify this derived jet formation criterion.

Chapter 3 Numerical Modeling

This chapter is divided into two sections. The first section describes the development of the 2-dimensional geometry and the mesh used to model the synthetic jet actuator. Section two of this chapter will describe the details of the FLUENT setup.

A schematic of the piezoelectric synthetic jet actuator design configuration tested is shown in Figure 2.
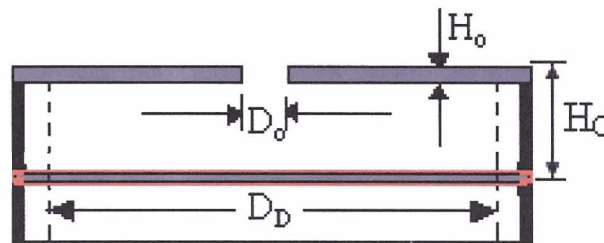

Figure 2 Synthetic Jet Cavity Dimensional Parameters

3.1 Geometry and Mesh

Using Gambit 2.1 the cavity is formed from three boxes that comprise the cavity, the orifice, and the ambient air into which the jet exits. The three boxes are translated and united as shown below in Figure 3 to form a single face.
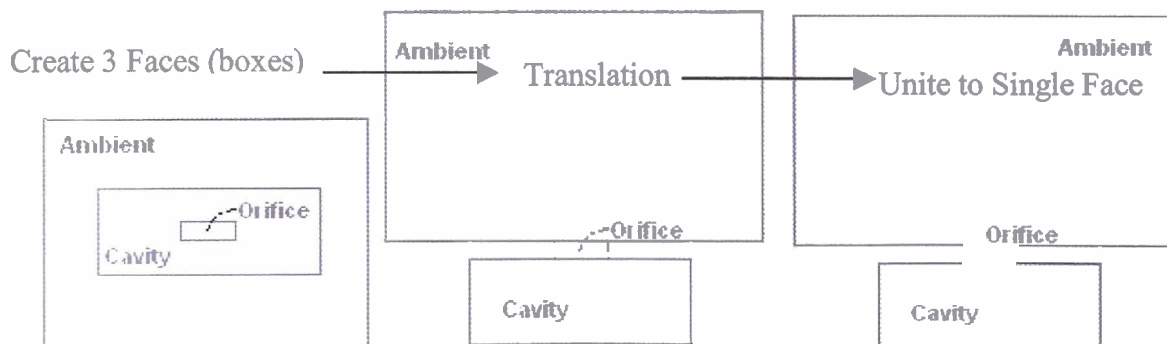

Figure 3 Synthetic Jet Geometry Development

31

Boundary conditions are then specified for each of the edges that comprise the cavity and the ambient fluid into which the jet is expelled. As shown in Figure 4, the diaphragm and cavity are walls; the ambient is specified with 4 pressure inlets and one pressure outlet. The diaphragm is defined separately from the rest of the walls so that the user-defined function to describe its movement can be applied to the diaphragm separately.
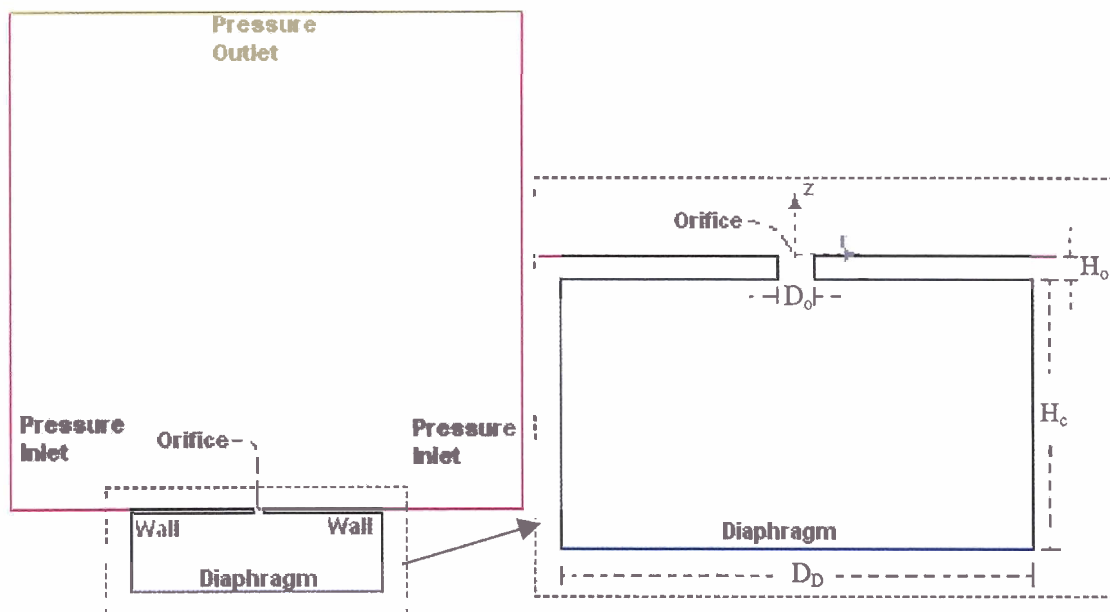
Figure 4 Synthetic Jet Geometry Boundary Conditions and Dimensions.

To improve the computational efficiency of the numerical simulation a reduction in the total number of grid points in the mesh can be achieved by taking advantage of the cavities symmetry by applying a symmetric axis to model only half the cavity. FLUENT requires the axis of symmetry to be in the x-axis direction, which we have designated as the z-axis as shown in Figure 5. The cavity is thus partitioned in half and rotated 90

degrees clockwise. The origin of the coordinate system is at the center of the exit orifice where r is the radial axis and z is the axial axis as shown below in Figure 5.
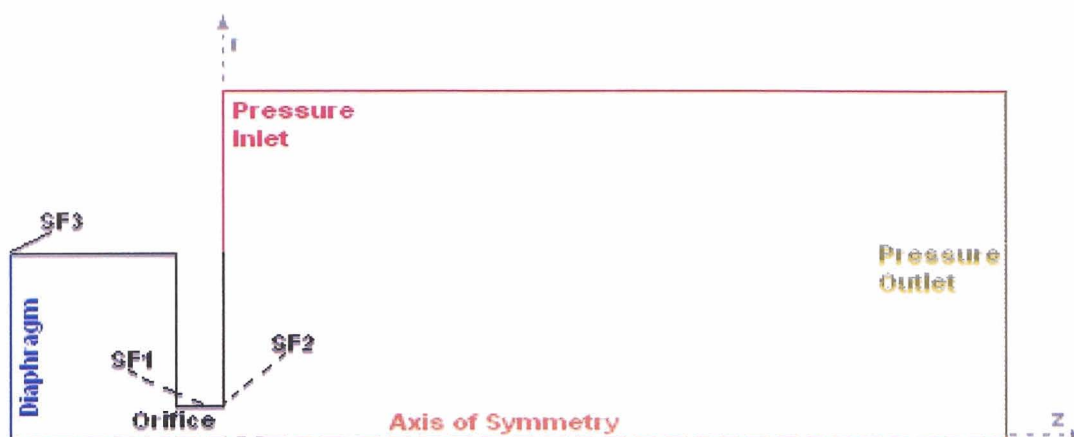

Figure 5 Synthetic Jet Axisymmetry Conditions and Mesh Sizing Functions

Size functions to control and specify the size of the mesh spacing intervals between nodes are specified. Size functions control the mesh characteristics in the proximity of the entities to which they are attached. The three sizing functions are shown in Figure 5 as SF1, SF2, and SF3. They are attached to the orifice edge, orifice exit vertex, and the diaphragm upper left vertex respectively. The start size and growth rate values for the size functions for the geometries tested are shown in Appendix A.

After application of the size functions the face is meshed using the tri-pave unstructured scheme that results in the following mesh shown in Figure 6. The tri-pave unstructured scheme is chosen to allow for relative displacement among the nodes on the diaphragm that is necessary and not possible with the structured quadrilateral scheme[47].
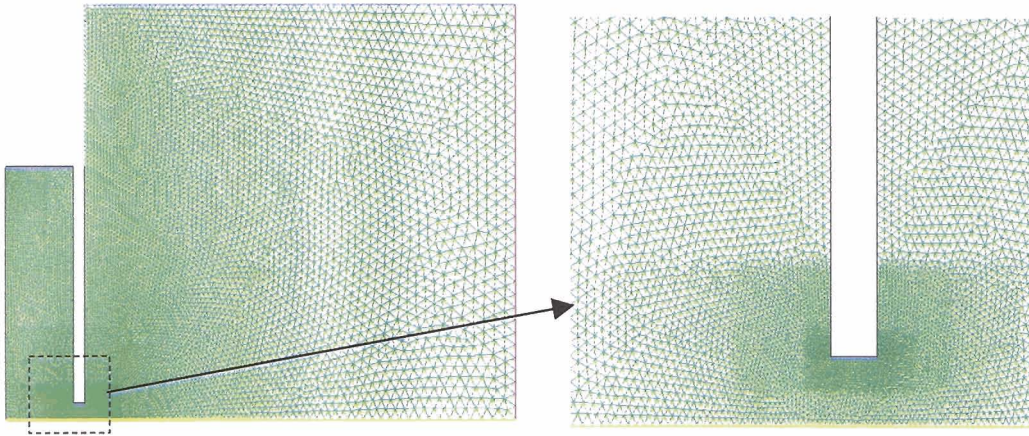
Figure 6 Synthetic Jet Mesh

The relevant mesh parameters and domain extents for the various geometries tested are given in Appendix B.

3.2 FLUENT Set Up

The mesh developed in Gambit is exported into FLUENT, which uses a control-volume-based technique to convert the governing Navier-Stokes differential equations at each node cell into algebraic equations that can be solved through iteration. Values are stored at the cell center and the face values needed for the convective term (see equation 13) are interpolated from center values. Diffusion terms are central-differenced and are always second-order accurate.

The segregated, unsteady, axysimmetric solver is chosen with first order implicit time scheme that is unconditionally stable with respect to time step size. The segregated solver mainly used for incompressible flows solves the resulting algebraic equations sequentially as opposed to the coupled solver that solves the algebraic equations

simultaneously. Solution of the energy equation is activated. Next the viscous model is chosen.

FLUENT has several viscous models to choose from to model turbulence. A brief outline description of each is included in Appendix C. The two models used in this study are the laminar model and the turbulent kinetic energy-dissipation rate, $\kappa - \varepsilon$, RNG "renormalization group" model. The RNG turbulent model is one that is derived using a rigorous statistical technique called renormalization group theory and has an additional term in its dissipation rate, ε, equation that significantly improves the accuracy for rapidly strained flows.

FLUENT provides three pressure-velocity coupling algorithms options: SIMPLE, SIMPLEC, and PISO. The latter of these three, Pressure-Implicit with Splitting of Operators (PISO) based on a higher degree of approximate relation between the iterative corrections for pressure and velocity is chosen. Whereas the SIMPLE and SIMPLEC algorithms new velocities and corresponding fluxes do not satisfy the momentum balance after the pressure-correction equation is solved, the PISO algorithm uses the "neighbor correction" option that updates velocities to satisfy both the continuity and momentum equations more closely. Although the PISO algorithm requires more CPU time it greatly improves transient calculations as concluded by Tang and Zhong[45] . This algorithm also significantly reduces convergence difficulties associated with a highly distorted skewed mesh with approximately the same number of iterations that would be required for a more orthogonal mesh. Second order upwind spatial discretization is used for the momentum, turbulent kinetic energy, turbulent dissipation rate, and energy. Due to the nonlinearity of

the equation set, it is necessary to control the calculated value change to assure proper convergence. Under-relaxation parameters are used to reduce changes during iterations. The default under-relaxation parameters were kept at 0.3, 1.0, and 0.7 for pressure, density and momentum respectively. These default values are set near optimal for the largest possible number of cases [47].

Remeshing and smoothing are activated and set for the dynamic mesh parameters. For remeshing the size remesh interval is set to 1 to check for remeshing after each time step, the maximum skewness was set through trial and error to 0.6 and the "must improve skewness" option is chosen. Minimum and maximum cell area values are set to 1E-12m and 1E-4 respectively. The minimum cell area values were chosen to be an order of magnitude smaller than the initial smallest cell to prevent both unnecessary remeshing of smaller cells. The minimum was large enough however to prevent a negative cell volume as the diaphragm moves. The maximum cell area was simply chosen to be any value larger than the largest initial mesh cell area. In the smoothing option a spring constant factor of 0.7, boundary node relaxation of 0.5, convergence tolerance of 1E-5 and max iterations of 20 is set. Similar to the maximum cell skewness, the smoothing option and spring constant factor were chosen through trial and error.

The three macros available for defining a dynamic mesh with a moving boundary are DEFINE_CG_MOTION, DEFINE_GEOM, and DEFINE_GRID_MOTION. Neither DEFINE_CG_MOTION nor DEFINE_GEOM allow for the motion of each node to be specified independently. The DEFINE_GRID_MOTION macro does allow for the position of each node to be updated independently so that it is possible to specify the relative motion amongst the

nodes that occurs with the deforming diaphragm motion. The user defined function (UDF) written in C with the logarithmic velocity profiles described by equation 2 to specify the oscillatory diaphragms movement with code explanation is attached in Appendix D. The UDF profile for the parabolic profile (equation 4) is similar to the logarithmic profile with only a change to the velocity function. The UDF is loaded as a compiled function and attached to the diaphragm.

The solution is then initialized at the diaphragm with initial guess of zero for the gauge pressure, axial velocity and radial velocity. For the turbulent $\kappa - \varepsilon$ RNG model turbulent specifications for the pressure inlet and outlet boundary are set using the intensity and length scale with values of 2% intensity and a length scale of 0.35mm and the initial guess for turbulent kinetic energy and turbulent dissipation rate are set to 0.05 m^2/s^2 and 0.05 m^2/s^3 respectively. The default of 20 maximum iterations per time step is kept. A time step is chosen based on the actuation frequency to allow for 200 time steps per cycle as shown in equation 48.

$$\Delta t = \frac{1}{f * 200}$$
Equation 41

Chapter 4 Results and Discussion

This section includes the numerical results in terms of velocity profiles and pressure distributions obtained for the tested cavity configurations shown in table 1. The control case, is a cavity that utilizes a magnetic shaker to drive a diaphragm as described by Tang and Zhong.[45], and it is utilized to verify parameters used for the code utilized in this study. Cavity I and Cavity II dimensions are utilized for the simulations and are validated with experimental work by Mane et al [48].

Table 1 Synthetic Jet Cavity Geometry

	Control Case	Cavity I	Cavity II
Hc (mm)	10	9.55	5.5
D_0 (mm)	45	60	60
H_0 (mm)	5	1.6	1.6
D_0 (mm)	5	3.67	2
δ_C (mm)	0.5, 0.8	0.396, 0.07	0.396, 0.07
f (Hz)	50	5 to 100	5 to 100

For the control case cavity tested by Tang and Zhong[45], two diaphragm amplitudes of 0.5mm and 0.8mm were studied at a single frequency of 50 Hz. At this frequency, Tang and Zhong conducted several experiments and collected Particle Image Velocimetry (PIV) and hot wire data for varying peak-to-peak center diaphragm amplitudes, δ_C, between 0.3mm and 1.1mm. However, only two cases corresponding to a center peak-to-peak diaphragm displacement, δ_C, of 0.5mm and 0.8mm were studied in detail. Furthermore, only the logarithmic velocity profile (Equation 2) is used to describe diaphragm

movement. For cavities I and II, two diaphragm displacements of 0.396mm and 0.07mm that correspond to the Bimorph and Thunder actuators respectively were tested at frequencies ranging from 5 to 100 Hz as described in section 2.1.1. For each of the cavities, both a logarithmic and parabolic velocity profile (equations 2 and 4) were used. A discussion of the obtained numerical results and validation through experimental results is presented in the following sections.

4.1 Control Case Cavity Results

Experimental and numerical data courtesy of Tang and Zhong [45] were used for the control case as a basis to validate the model utilized for this study. By performing experiments at a frequency, f, of 50 Hz, using a Particle Image Velocimetry (PIV), hot wire, and smoke flow visualization Tang and Zhong concluded that for the smaller δ_C values, i.e., 0.5mm, the ensuing jet was predominantly laminar, and for a $\delta_C = 0.8$ mm the resulting jet was mainly turbulent. Numerically, she applied a velocity boundary condition and a displacement profile, described by Equation 3, at the neutral position of the diaphragm. Using this velocity boundary condition, she studied a laminar case and four turbulent cases; the standard $\kappa - \varepsilon$, RNG $\kappa - \varepsilon$, standard $\kappa - \omega$, and the Reynolds stress model, RSM. Her work concluded that the RNG $\kappa - \varepsilon$, and the standard $\kappa - \omega$ models produced the best results.

Based on the results of Tang and Zhong, a value of $\delta_C = 0.5$mm for a laminar case, and $\delta_C = 0.8$mm for a turbulent case with a RNG $\kappa - \varepsilon$ turbulence model was chosen for this study. In this study, a moving boundary is utilized instead of a velocity boundary. The

following results compare the experimental and numerical data of Tang and Zhong to the numerical approach used on this study.

Figures 7a and 7b show the experimental and numerical velocity magnitude results for one jet cycle at the center of the exit orifice for the laminar case and the turbulent case respectively.
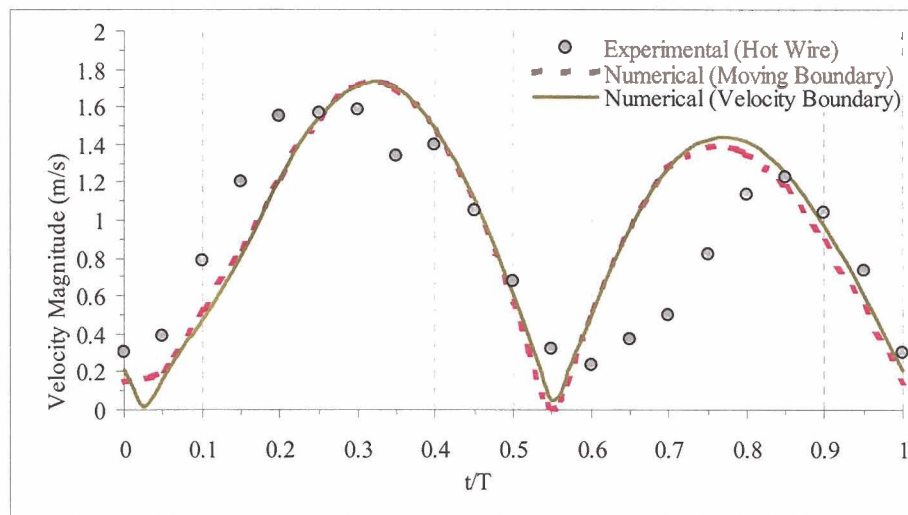
(a)
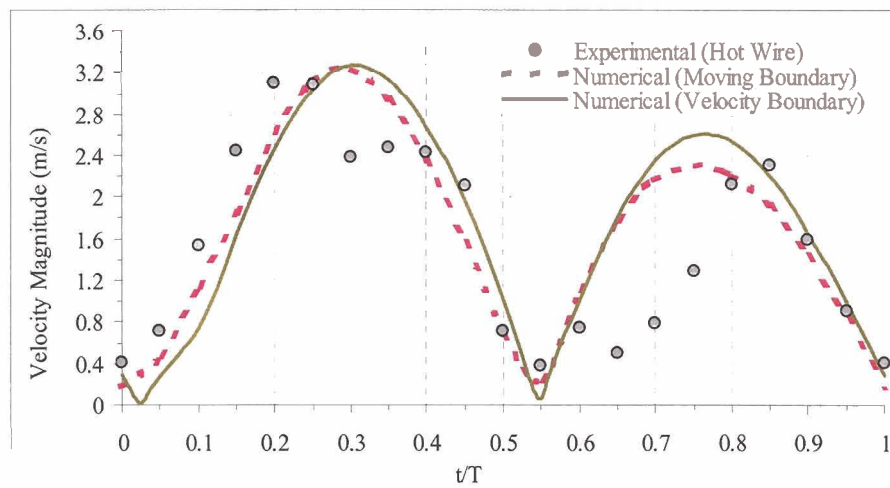
(b)

Figure 7 Control case, velocity magnitude at r = 0mm, z=0mm a) Laminar case, and b) Turbulent Case

The velocity magnitude at the center of the exit orifice predicted by both the velocity boundary and the moving boundary numerical models are in good agreement with the experimental hot wire data with a slight phase difference. In both, the laminar and turbulent case, the numerical models lag the experimental data during the blowing portion of the cycle (t = 0 to 0.5T) while for the suction cycle (t = 0.5T to t = 1T) the numerical data leads the experimental data. For the laminar case both numerical models are nearly identical with the maximum predicted velocity approximately 10% larger than the experimentally measured maximum velocity. For the turbulent case the only significant difference between the two numerical models appears to be during the suction cycle where the velocity boundary model gives approximately 8% larger maximum suction velocity than the moving boundary numerical model.

The instantaneous centerline velocities at a sample value of t = 9/16T up to an axial distance of five diameters for the oscillating diaphragm numerical model is compared with PIV experimental data collected by Tang and Zhong[45], and the velocity boundary numerical model for the laminar case in Figure 8.

The results shown in Figure 8 indicate that the moving boundary model gives significant larger velocity values than both the experimental data, and the velocity boundary numerical model data. Although the moving boundary model lags the experimental data by approximately half a diameter (2.5mm) it does capture the three distinct peaks measured which correspond to consecutive vortex rings.
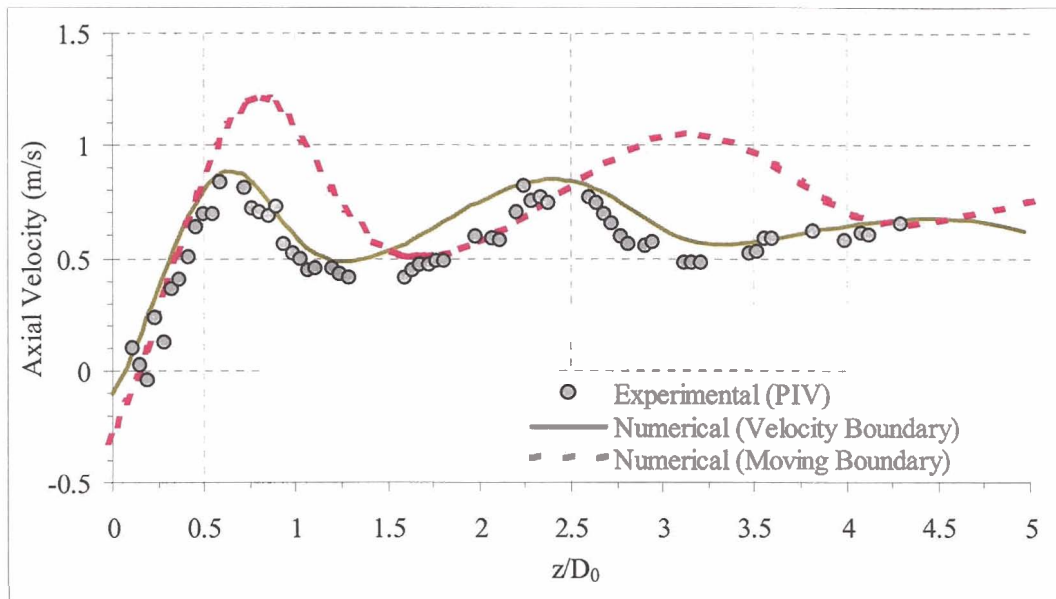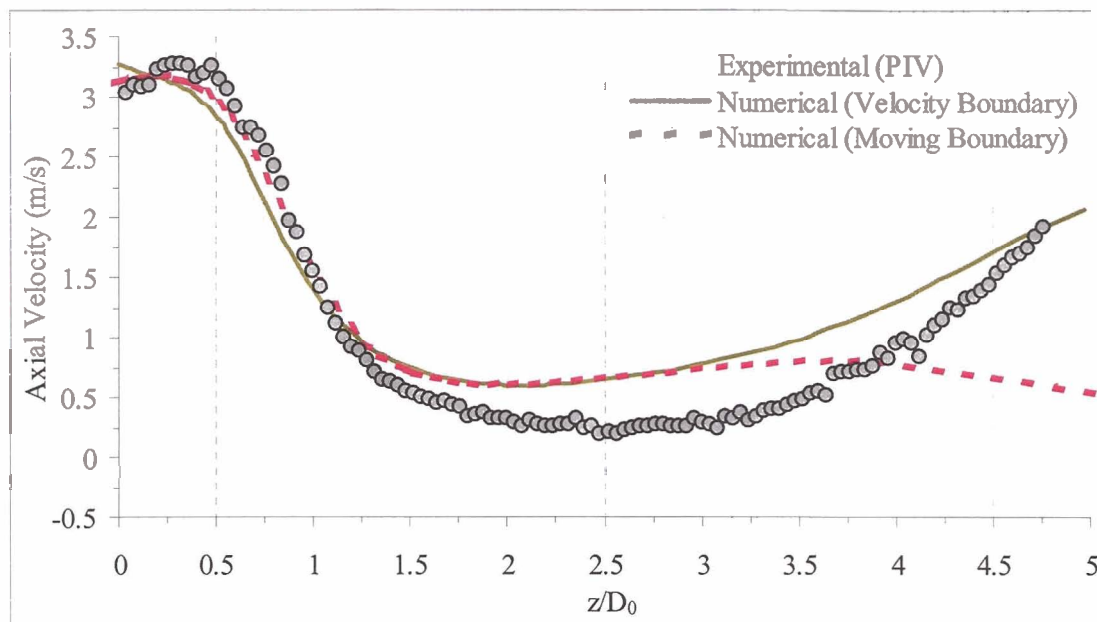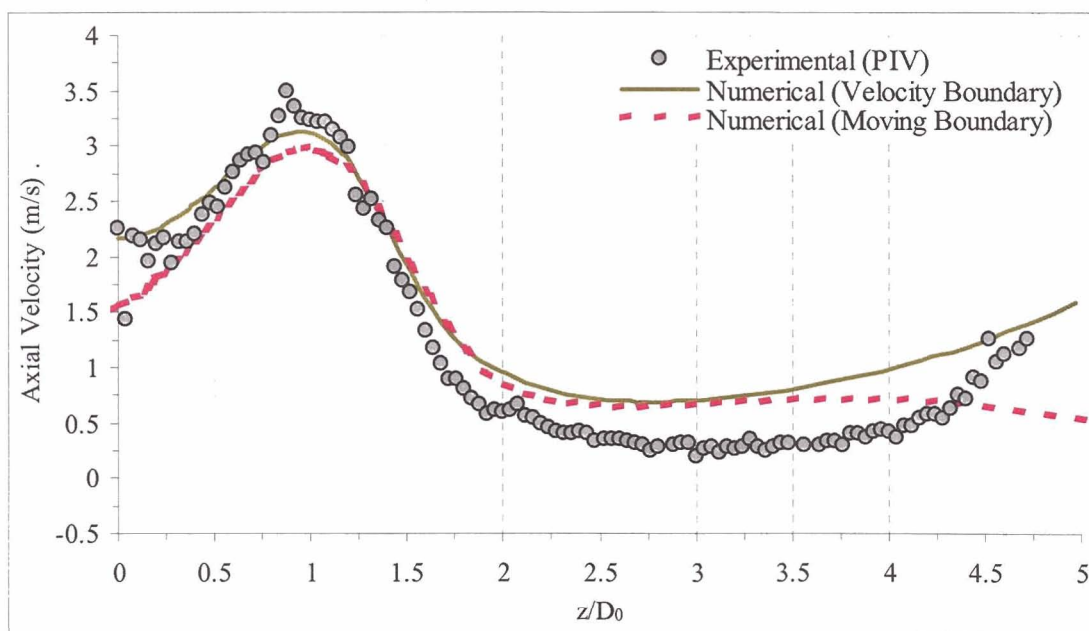
Figure 8 Laminar flow control case centerline axial velocity at t/T = 9/16

The instantaneous centerline velocities at selected times $t/T = 5/16$ and $t/T = 7/16$ up to an axial distance of $5D_o$ for the two numerical models are compared with PIV data for the turbulent case in Figures 9a and 9b respectively. Up to an axial distance of approximately $1.5D_o$ both numerical models accurately predict the centerline jet velocity for both $t/T = 5/16$ and $t/T = 7/16$. After a distance of $1.5D_o$ however both models over predict the experimentally measured velocity. It can be seen that both the velocity and the moving boundary models are nearly identical up to approximately $3D_o$ where the oscillating moving boundary model plunges under-predicting the second peak of the experimentally measured velocity. The under prediction of jet velocity in the far field suggest that the numerical moving boundary model does not accurately represents the momentum of the slug of fluid. One possibility for the inaccuracy could be dissipation due to viscous effects or turbulent diffusion. The difference could also be due to the fact that the model does not couple the displacement and pressure within the cavity which could

effect the shape of the actuator profile and thus change the total volume of air that is displaced.


(a)

(b)

Figure 9 Turbulent flow control case, cavity centerline axial velocity a) t/T = 5/16, b) t/T = 7/16

An instantaneous velocity profile at a selected time of t/T = 14/16 across the span of the jet at an axial distance of 5mm for the laminar case is shown in Figure 10. It can be seen that at this distance and time the oscillating diaphragm numerical model over predicts the maximum velocity by approximately 20%. The shape and width of the jet however are in good agreement with the experimental data.
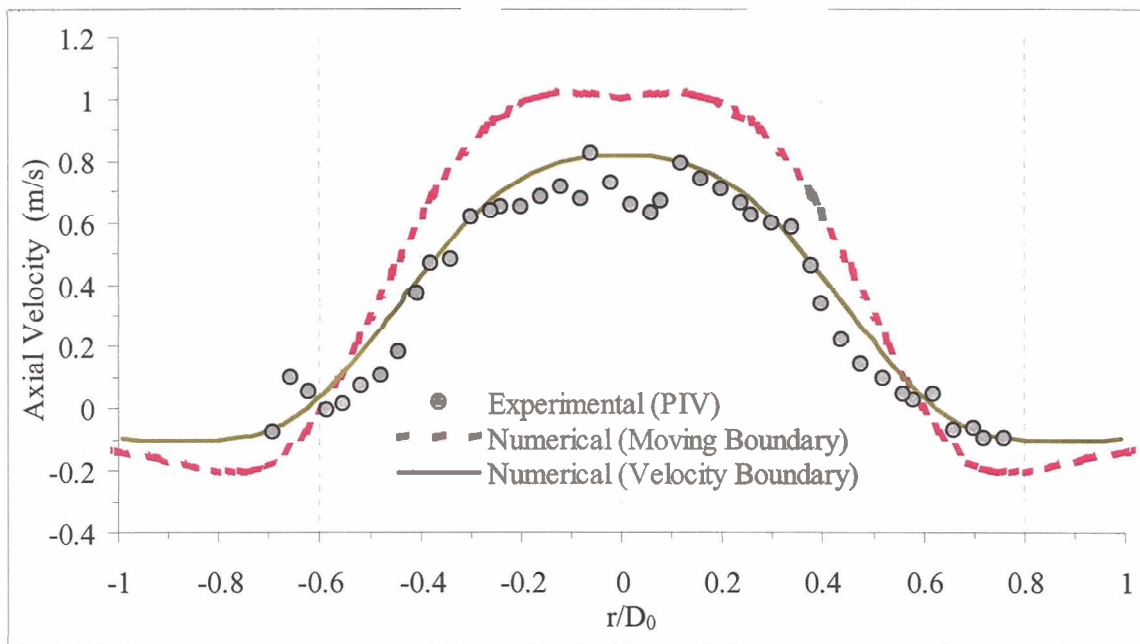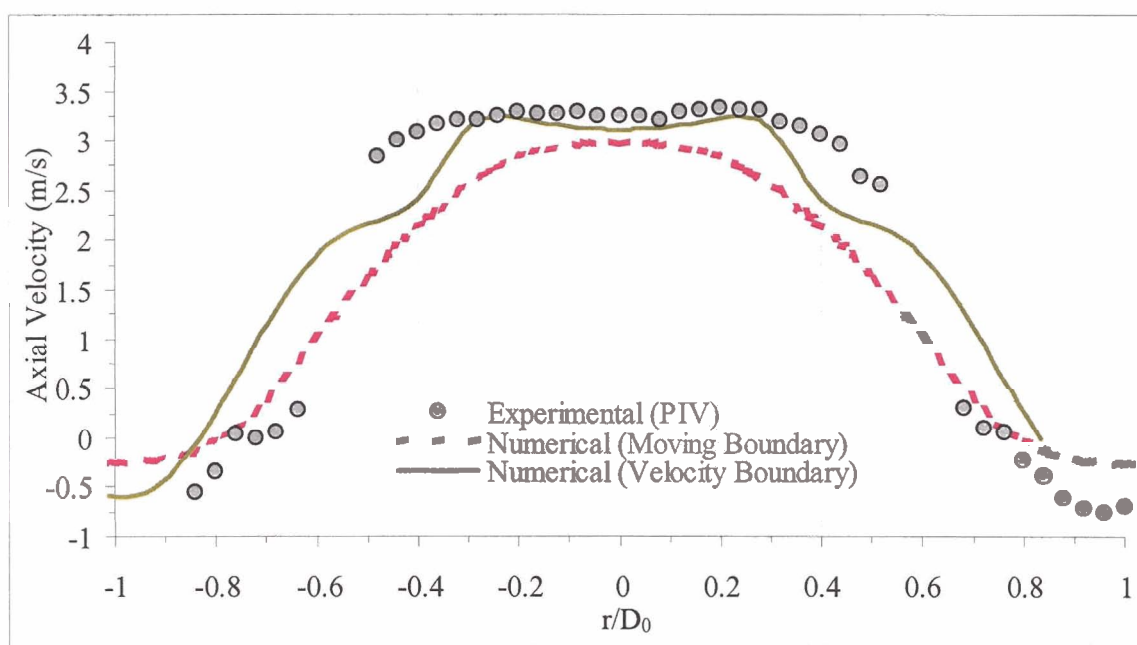

Figure 10 Laminar flow control case axial velocity profile at z=5mm, and t/T=14/16

Figures 11a and 11b show the instantaneous velocity profile at t/T = 5/16 and t/T=7/16 across the span of the jet at an axial distance of 5mm for the turbulent case. The velocity magnitude comparison between the numerically predicted values and the PIV experimental values are in good agreement.
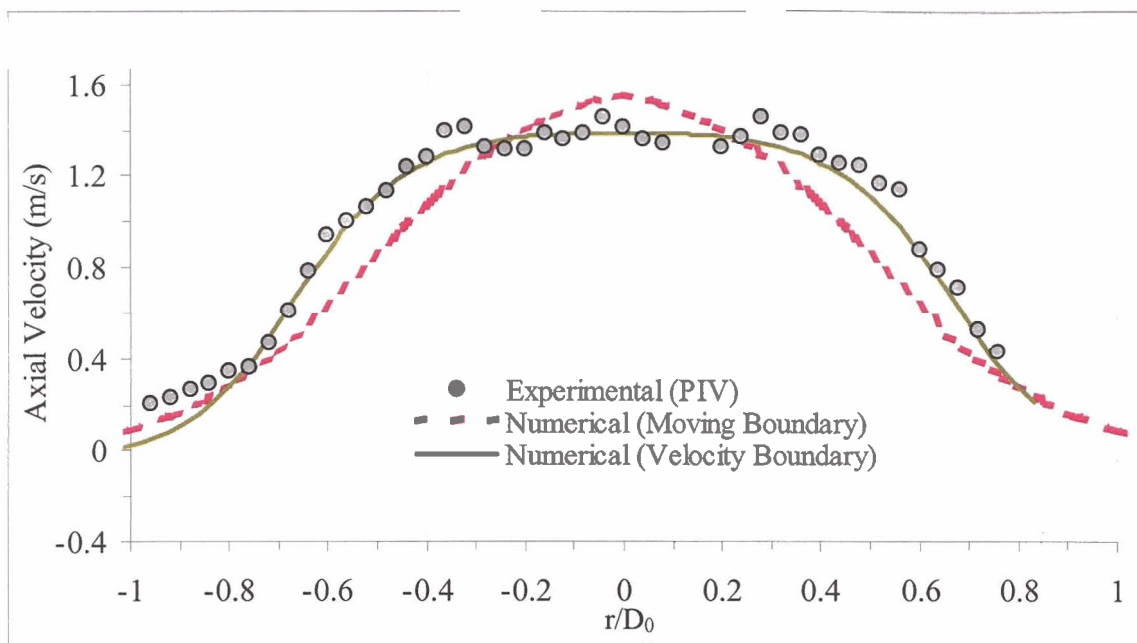
(a)

(b)

**Figure 11 Turbulent flow control case axial velocity at z=5mm, a) t/T = 5/16, b) t/T = 7/16**

Keeping all parameters equal, frequency, f, orifice diameter, D_o, actuator diameter,

D_D, and peak-to-peak center displacement, δ_C, the control case cavity height was doubled

(20mm) and halved (5mm) to test the moving boundary numerical model dependence if any on cavity height, H_c. Figures 12a and 12b show the instantaneous centerline axial velocity for the laminar and turbulent case respectively for the tested cavity heights. It can be seen that for the laminar case, cavity height does not have any effect on the model. For the turbulent case cavity height has only a slight shift on the profile but the magnitude is essentially the same.
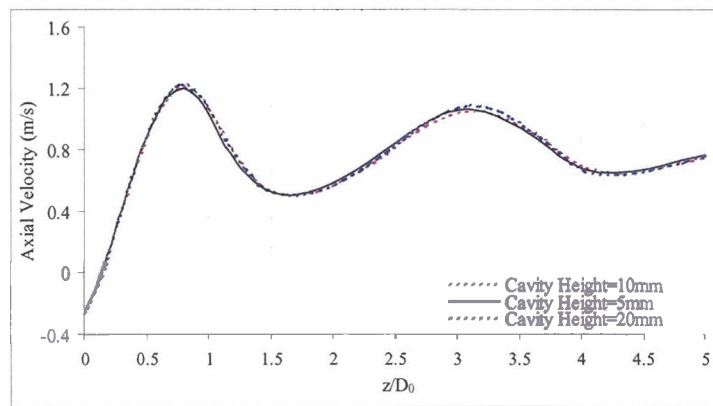
(a)
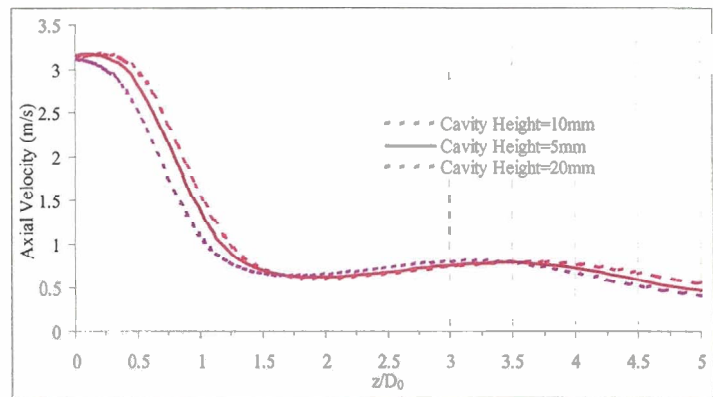
(b)

Figure 12 Control case cavity height dependence a) Laminar b) Turbulent

4.2 Bimorph Results

4.2.1 Bimorph Cavity I Results

The following section is for the Bimorph actuator in the cavity I configuration. The experimentally measured and numerically used peak-to-peak center diaphragm displacement, δ_C, for the Bimorph actuator is 0.396 mm as described in section 2.1.1.

For the numerical velocity profiles the actuator positions are defined as: (a) maximum volume at $t = 0$ occurs when the diaphragm is at its lowest point (furthest from orifice) and the cavity has maximum fluid volume; (b) maximum expulsion ($t = 0.25T$) corresponds to when the diaphragm is at level position and moving with maximum velocity towards the orifice; (c) minimum volume occurs halfway through the cycle ($t = 0.5T$) when the diaphragm is at the highest position (closest to orifice) and the volume of fluid in the cavity is at a minimum; (d) maximum ingestion ($t = 0.75T$) corresponds to when the diaphragm is at level position and moving with maximum velocity away from the orifice. Figures 13 through 16 show the velocity magnitude vector plots, dynamic pressure and static pressure for each of these stages for the logarithmic profile for the Bimorph actuator in the cavity I configuration.

Figure 13 shows the synthetic jet at t = 0 (Maximum cavity volume) that follows the completed ingestion part of the cycle. Vortices that developed inside the cavity during the ingestion cycle are evident in both the vector plot, Figure 13a, and dynamic pressure contour plot, Figure 13b. The fluid that is pulled inside the cavity creates a higher-pressure area at the back wall of the cavity where the incoming jet of air hits. This higher pressure is relatively low at only 16 Pa, which would require a highly sensitive dynamic pressure

transducer to experimentally measure it. From the vector plots of Figure 13a one can also see the remains of the slug of fluid that developed during the expulsion part of the cycle.

Figures 14a-14c shows the vector and pressure plots of the synthetic jet at the maximum expulsion position, t = 0.25T. At this point the diaphragm is at the neutral position and moving toward the orifice with maximum velocity. Figure 14a of the vectors plot clearly shows the shedding vortices of the synthetic jet. At this point the maximum observed velocity is 6m/s. The static pressure contour plot, Figure 14c, shows that a high pressure of 20 Pa is present inside the cavity. Figure 14c also shows a low pressure of –20 Pa at the corners of the orifice inlet.

At the minimum cavity volume, t = 0.5T, Figure 15a and 15b clearly show the formation of the fluid slug that has developed and nearly completely separated. The maximum velocity has decreased slightly from the maximum expulsion, t = 0.25T, of 6m/s to 5m/s. The static pressure plot, Figure 15c, shows that a vacuum of –7Pa has developed inside the cavity.

Finally for the maximum ingestion, t = 0.75T, Figure 16 shows reverse similarities to the maximum expulsion plots of Figure 14, with the same velocity magnitude and developing vortices in the opposite direction. The plot of the static pressure, Figure 16c, also shows that low pressure points develop as in the case of the maximum ingestion plot, Figure14c, but instead of the corners of the orifice inlet the low pressure is located at the orifice outlet. This low pressure is also lower at approximately –35 Pa. At this point there is still a vacuum inside the cavity.
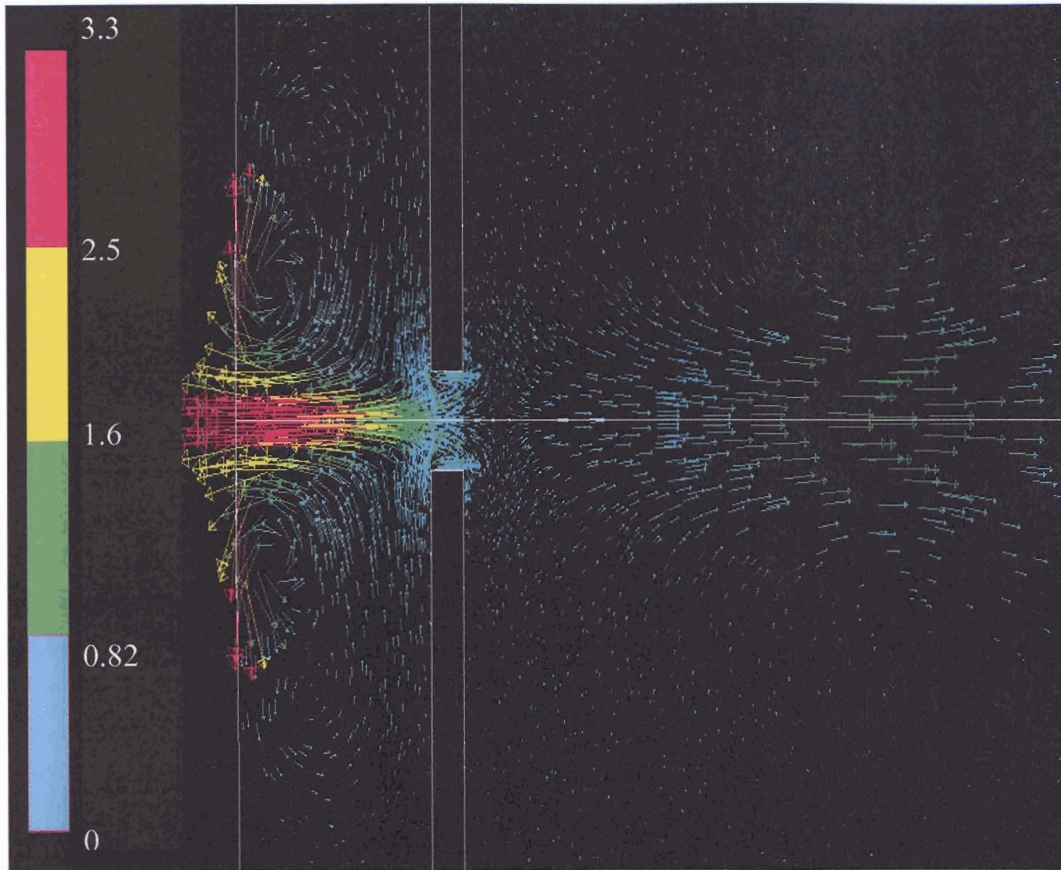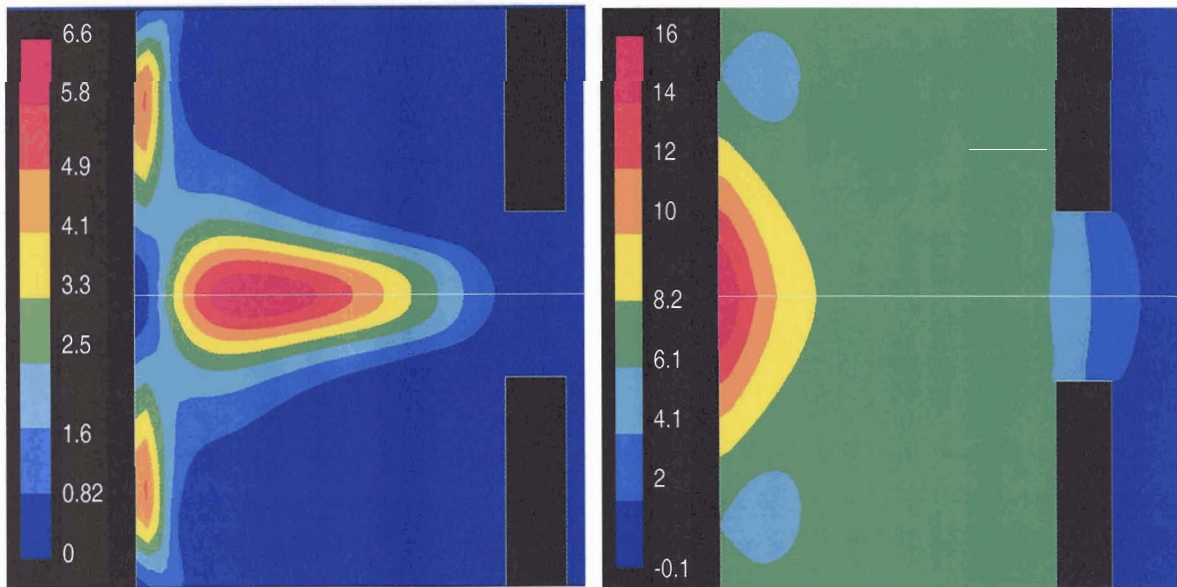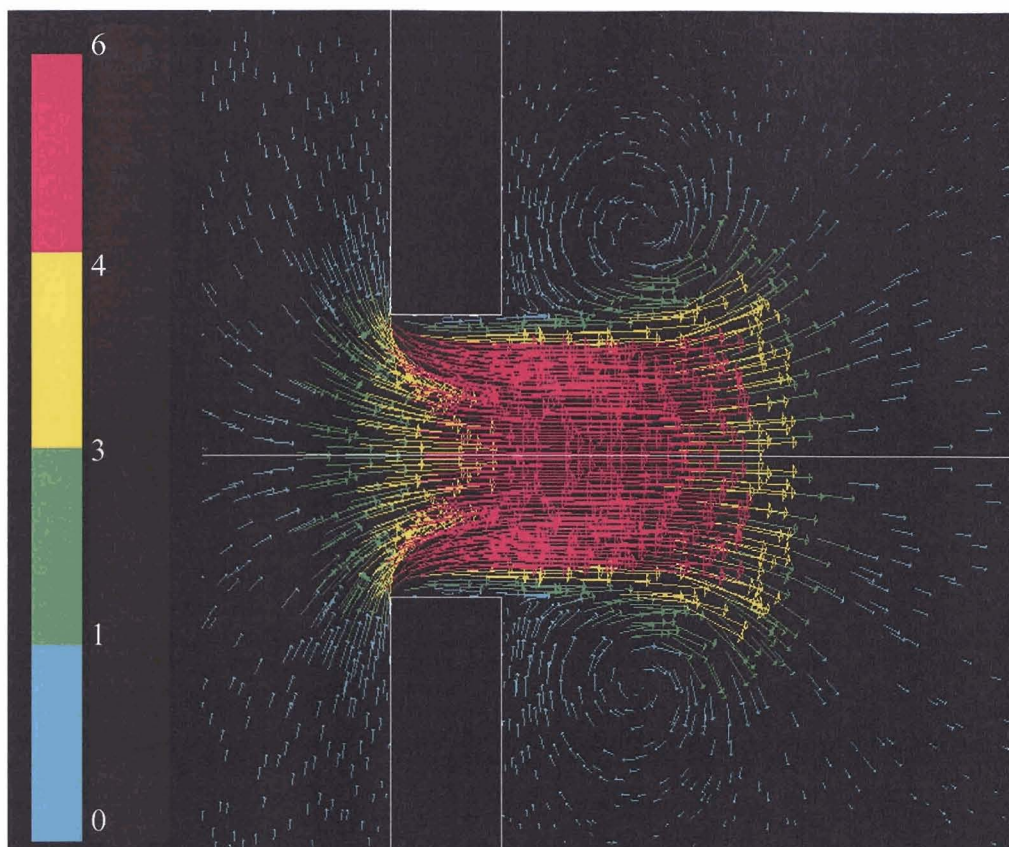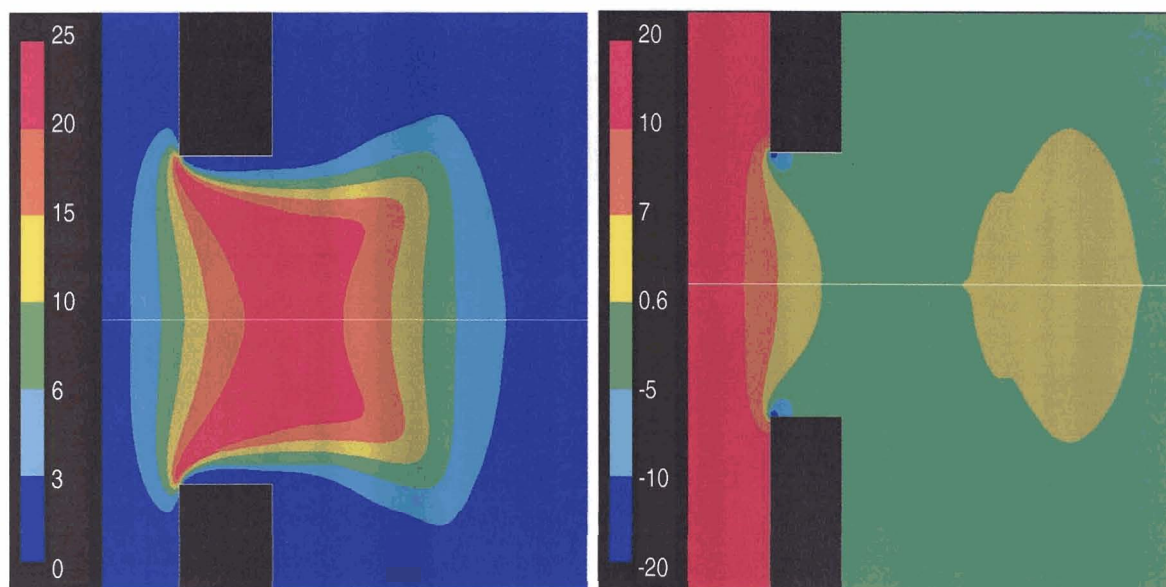
Figure 13 Bimorph Cavity I, Logarithmic Profile, t=0 Maximum Cavity Volume (a) Velocity Vectors (m/s); (b) Contour Plots of Dynamic Pressure (Pa); (c) Contour Plots of Static Pressure (Pa)

(a)

(b)

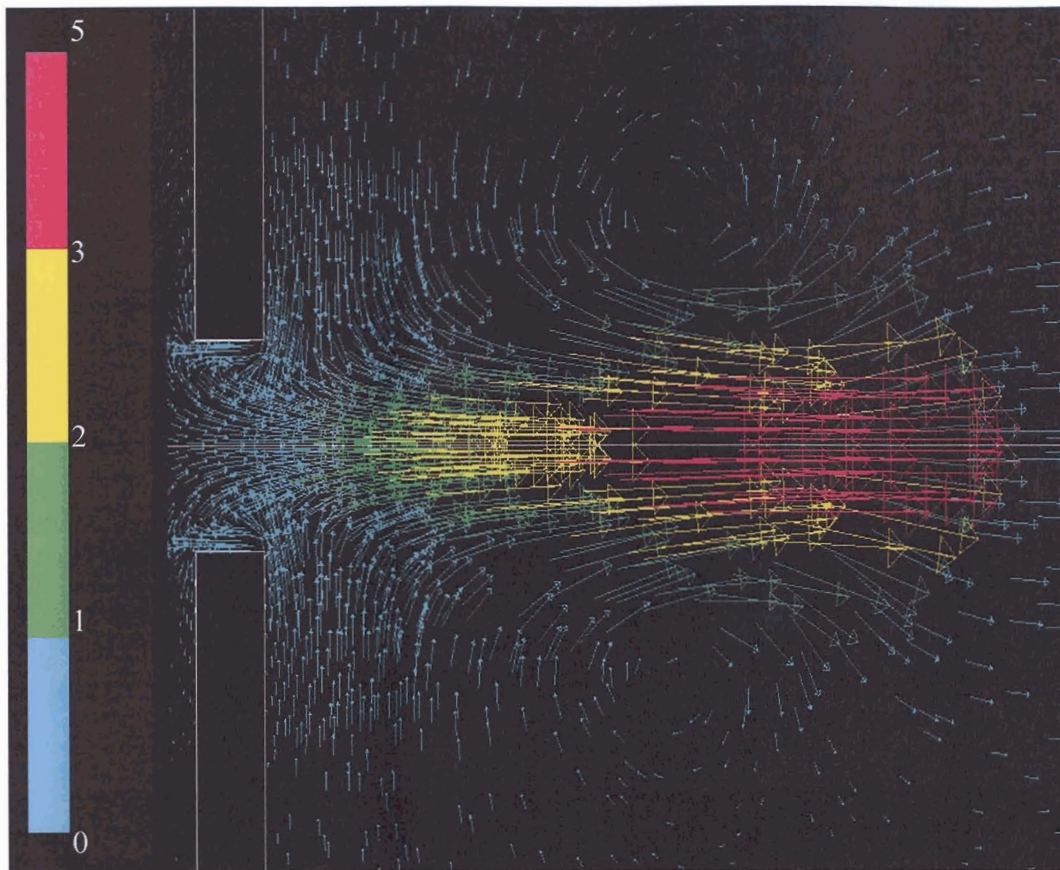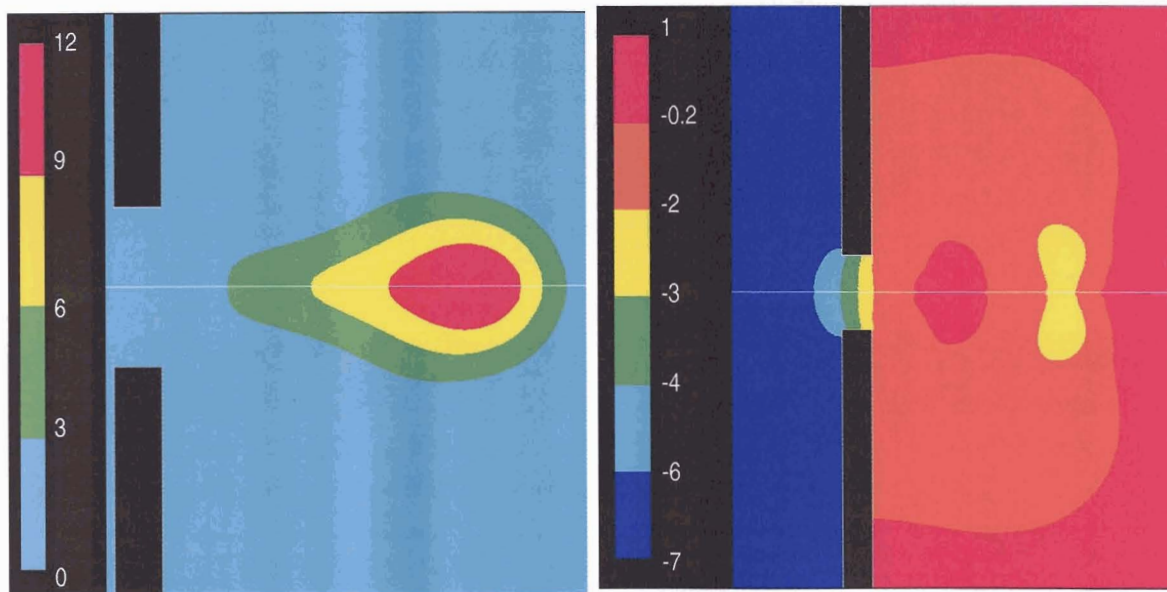**(c)**

Figure 14 Bimorph Cavity I, Logarithmic Profile, t=0. 25T Maximum Expulsion (a) Velocity Vectors (m/s); (b) Contour Plots of Dynamic Pressure (Pa); (c) Contour Plots of Static Pressure (Pa)
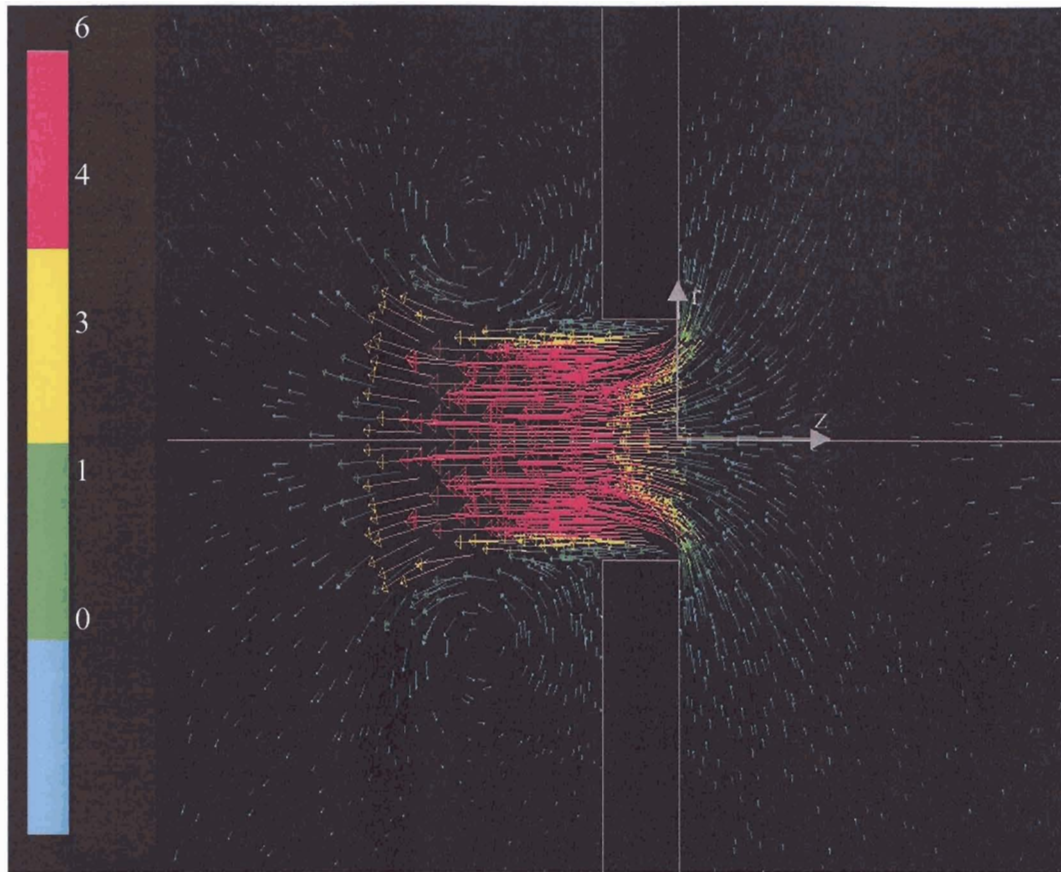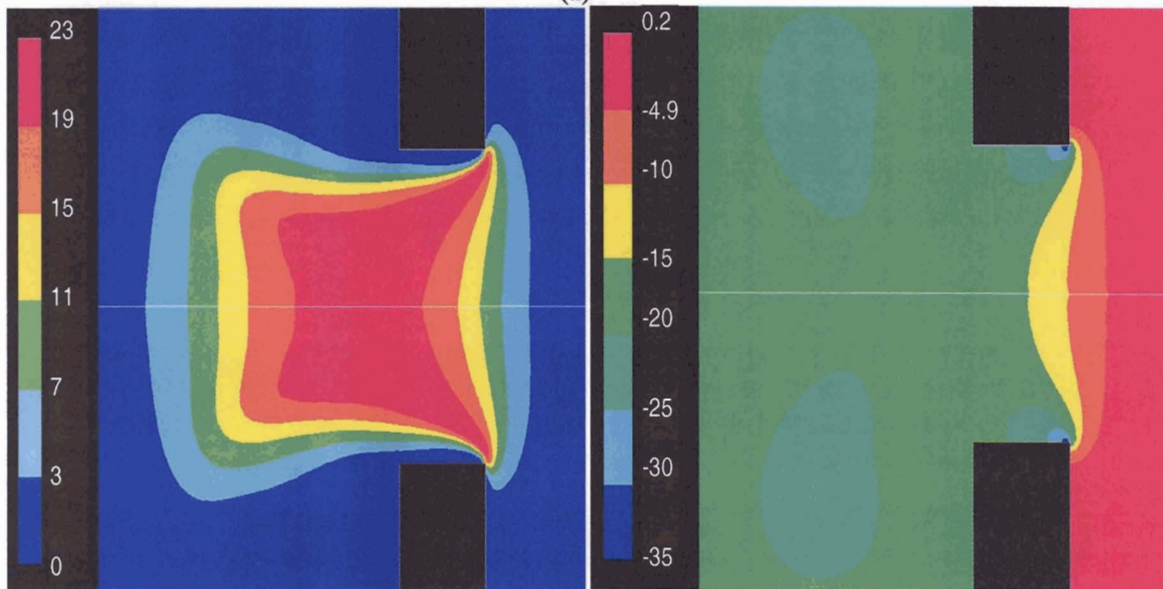
Figure 15 Bimorph Cavity I, Logarithmic Profile, t=0. 5T Minimum Cavity Volume (a) Velocity Vectors (m/s); (b) Contour Plots of Dynamic Pressure (Pa); (c) Contour Plots of Static Pressure (Pa)

Figure 16 Bimorph Cavity I, Logarithmic Profile, t=0.75T Maximum Ingestion (a) Velocity Vectors (m/s); (b) Contour Plots of Dynamic Pressure (Pa); (c) Contour Plots of Static Pressure (Pa)

Maximum measured experimental velocity[40], Figures 17a and 17b, is compared to numerical velocity at the various times described in Figures 14 to 16 versus radial position at an axial distance of 2mm, frequency of 50Hz, for the logarithmic and parabolic diaphragm profile displacement respectively. Figures 17a and 17b also include the time at which the maximum velocity which is noted to occur at t = 0.3T slightly after the maximum expulsion (t = 0.25T). Both tested actuator profiles, logarithmic and parabolic over predict the experimental results for the Bimorph actuator in cavity I. The logarithmic profile however gives a better approximation than the parabolic profile over predicting the maximum velocity by approximately 25% while the parabolic profile over predicts the maximum velocity by more than twice the experimentally measured maximum velocity.

(a)

(b)
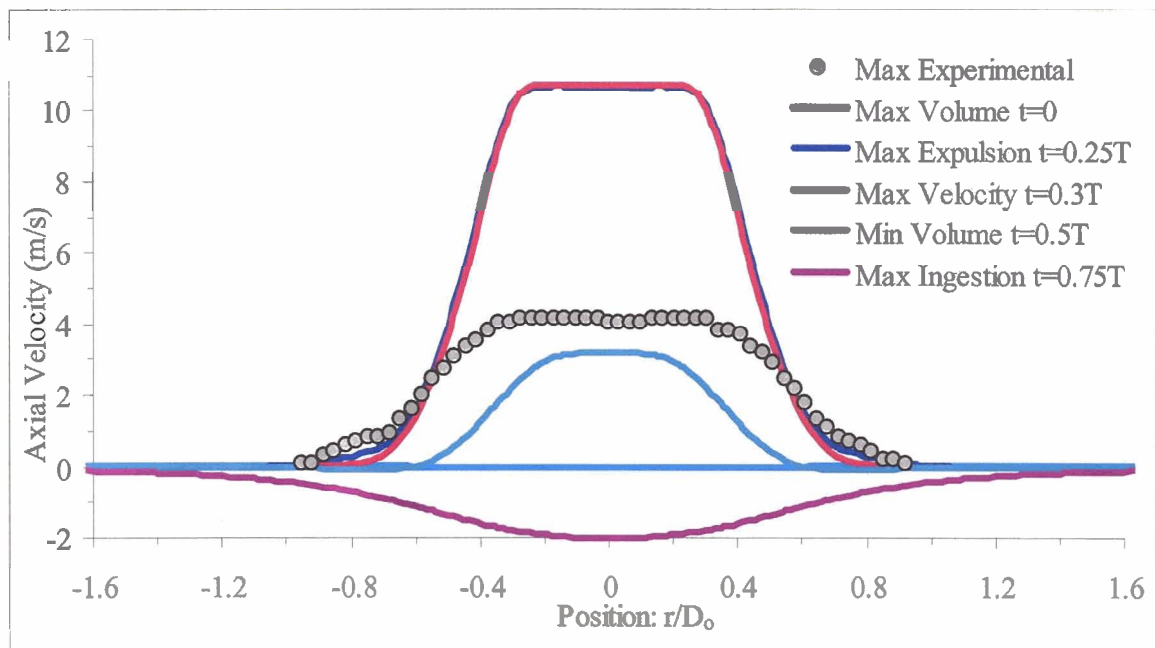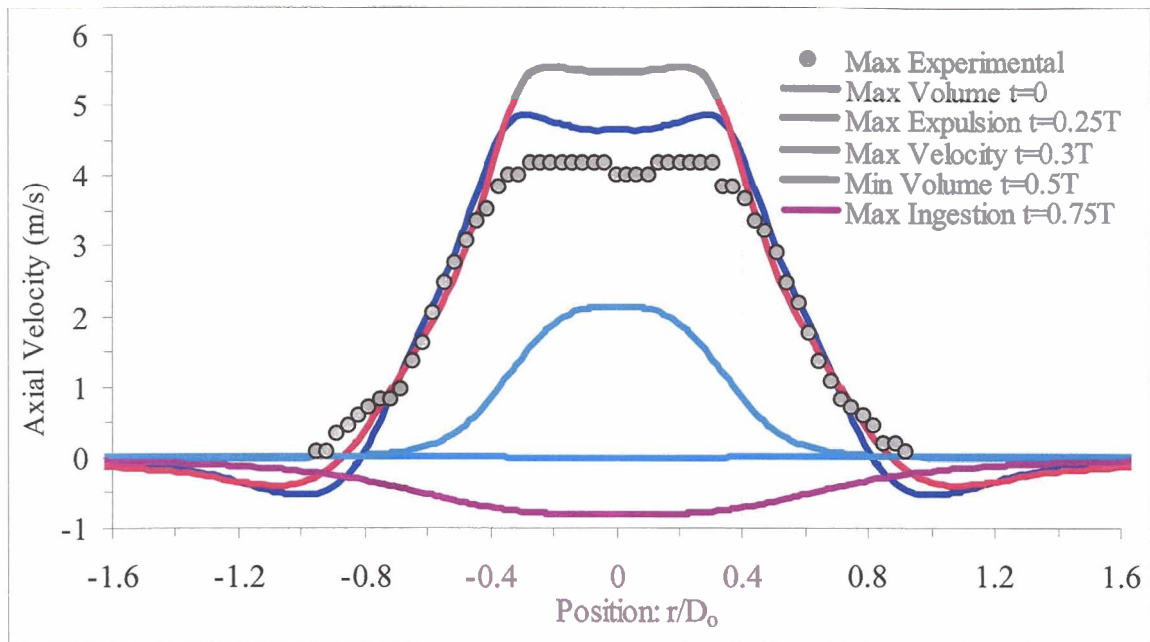
Figure 17 Bimorph Cavity I: Velocity vs. Radial Position at z=2mm for a) Logarithmic model, b) Parabolic model.

Figures 18a and 18b show a complete cycle for the center velocity (r = 0) at an axial distance of 2mm for the Bimorph actuator in cavity I at a frequency of 32Hz and 50Hz respectively. It can again be seen that for the Bimorph actuator a logarithmic profile displacement simulation gives a more accurate prediction than the parabolic profile when compared to the experimental results.
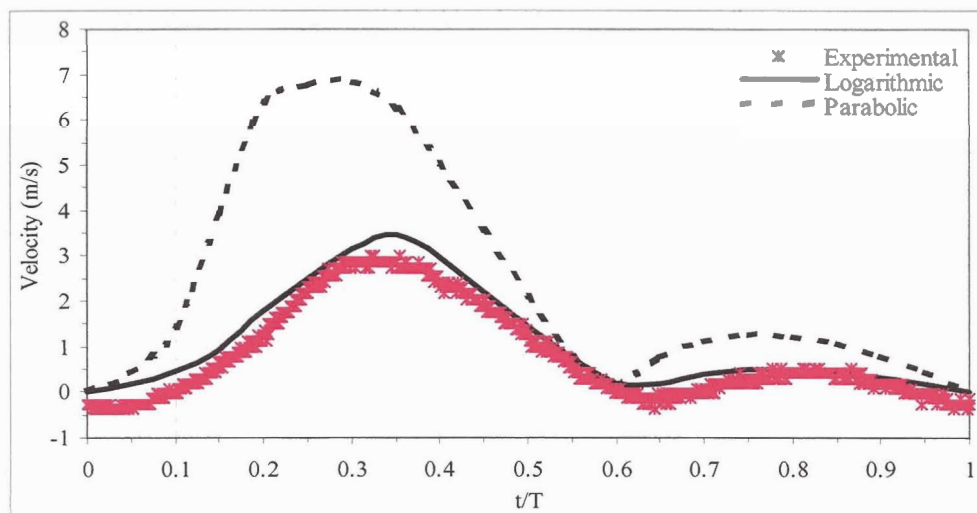
(a)
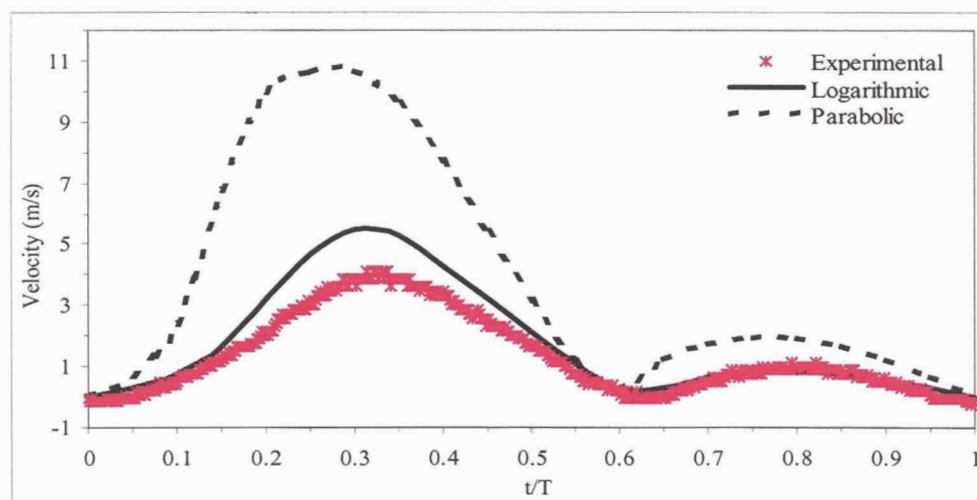
(b)

Figure 18 Bimorph Cavity I: Logarithmic and parabolic diaphragm profile center velocity vs. time comparison at z=2mm for a) 32Hz and b) 50Hz.

The maximum center velocity versus frequency at an axial distance of 2mm is shown in Figure 19. The logarithmic diaphragm profile clearly gives a better approximation than the parabolic profile for all tested frequencies diverging only toward the higher frequencies. This may be due to the driving frequency approaching the resonant frequency of the actuator.
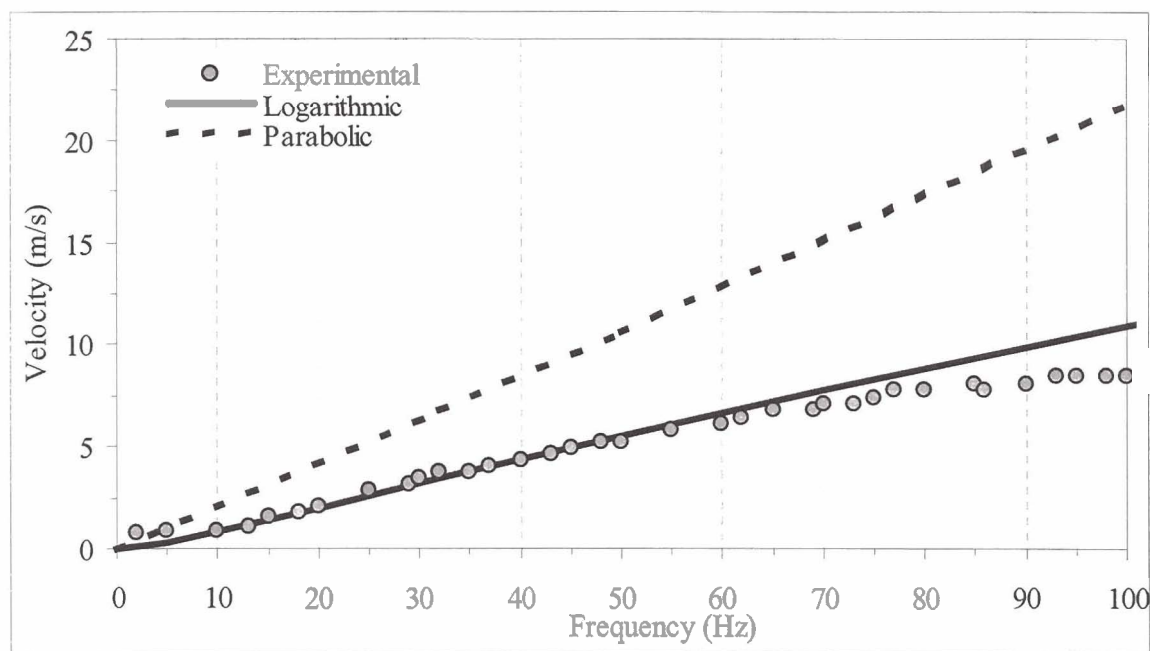
Figure 19 Bimorph Cavity I: Logarithmic and parabolic diaphragm profile max center velocity vs. frequency comparison at z=2mm.

4.2.2 Bimorph Cavity II Results

The following section is for the Bimorph actuator in the cavity II configuration. Figures 20 through 23 show the velocity vector and pressure plots at the four times, maximum volume (t = 0), maximum expulsion (t = 0.25T), minimum volume (t = 0.5T) and maximum ingestion (t = 0.75T), as described in section 4.2.1.

At the maximum volume, t = 0, Figure 20a shows that for the smaller orifice and cavity configuration the jet ingested inside the cavity has a slightly higher velocity magnitude (4.6 m/s) than the cavity I configuration (3.3 m/s). The vortices observed in cavity I are not as evident as in cavity II since there is not sufficient space in the cavity to allow the vortices of the faster jet to develop. Similar to the results of cavity I, the fluid that is pulled inside the cavity II configuration creates a higher-pressure area at the back wall of the cavity. Figure 20c shows that the pressure of the incoming slug of fluid that hits the back of the wall cavity is twice as much (32Pa) than the cavity I configuration.

Figures 21a through 21c shows the vector and pressure plots of the synthetic jet at maximum expulsion, t = 0.25T. At this point the diaphragm is at the neutral position and moving toward the orifice with maximum velocity. The jet at this point, for cavity II, has a higher maximum velocity (20 m/s) and does not spread as in the cavity I configuration. The width of the jet of fluid for the most part remains the size of the orifice with no shedding vortices. The range of the static pressure is also much higher for the cavity II configuration ranging from –170Pa at the corners of the orifice inlet to 210Pa in the inside of the cavity compared to –20Pa to 20Pa for the cavity I configuration.

At minimum cavity volume, t = 0.5T, Figure 22a and 22b clearly show the formation of the fluid slug that has developed and nearly completely separated. The maximum velocity has decreased significantly from the maximum expulsion, t = 0.25T, 20m/s to 5.5m/s. The vortices that develop for the cavity II configuration are bigger and less evident than the cavity I configuration. The static pressure plot, Figure 22c, shows a

small pressure gradient across the orifice that starts at −14 Pa inside the cavity and goes to 0 Pa at the orifice exit.

For maximum ingestion, Figure 23 at t = 0.75T shows the same velocity magnitude but in the opposite direction of the maximum expulsion at t = 0.25T. Unlike the maximum ingestion of cavity I for cavity II the leading edge of the ingested slug of air has already hit the back of the cavity wall. The plot of the static pressure, Figure 23c, also shows that low pressure points develop as in the case of the maximum ingestion plot, Figure 21c, but instead of the corners of the orifice inlet the low pressure is located at the orifice outlet. This low pressure of −380Pa is significantly lower than the cavity I configuration of −35Pa. At this point the majority of the inside of the cavity is a vacuum at approximately -180Pa.
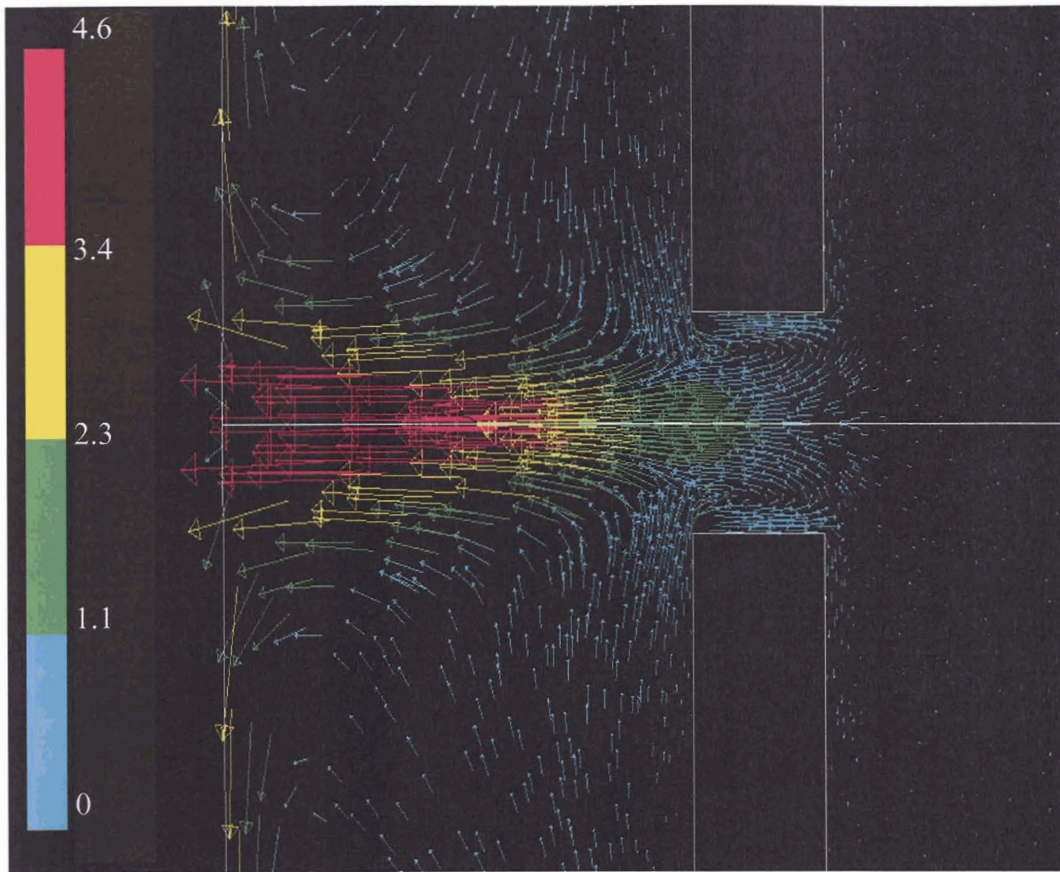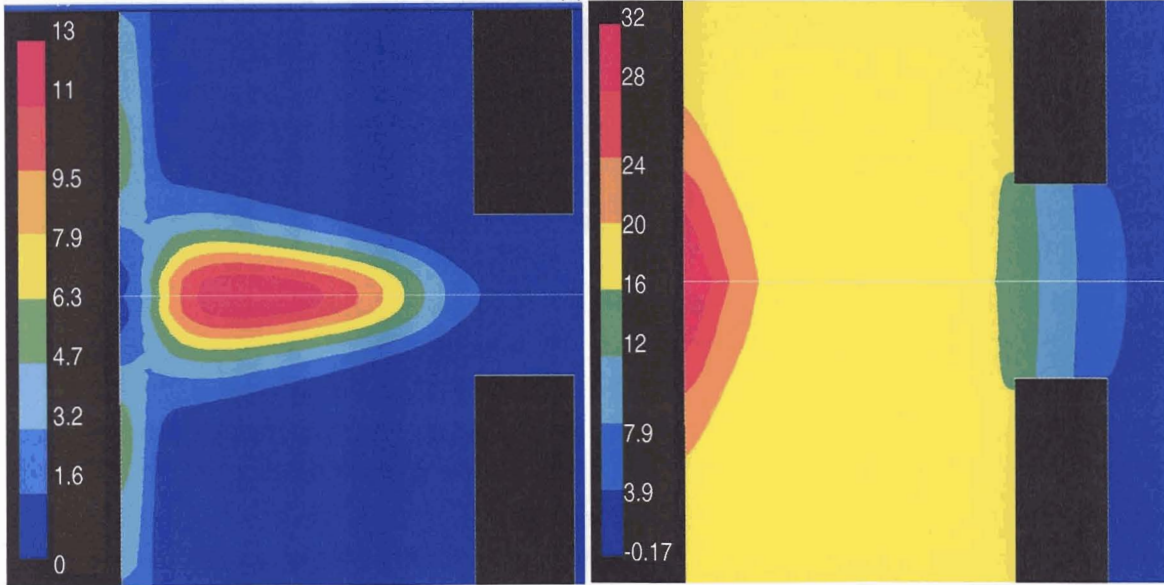
Figure 20 Bimorph Cavity II, Logarithmic Profile, Maximum Cavity Volume, t=0 (a) Velocity Vectors (m/s); (b) Contour Plots of Dynamic Pressure (Pa); (c) Contour Plots of Static Pressure (Pa)

(a)

(b)

(c)

Figure 21 Bimorph Cavity II, Logarithmic Profile, t=0.25T Maximum Expulsion (a) Velocity Vectors (m/s); (b) Contour Plots of Dynamic Pressure (Pa); (c) Contour Plots of Static Pressure (Pa)

Figure 22 Bimorph Cavity II, Logarithmic Profile, t=0.5T Minimum Cavity Volume (a) Velocity Vectors (m/s); (b) Contour Plots of Dynamic Pressure (Pa); (c) Contour Plots of Static Pressure (Pa)
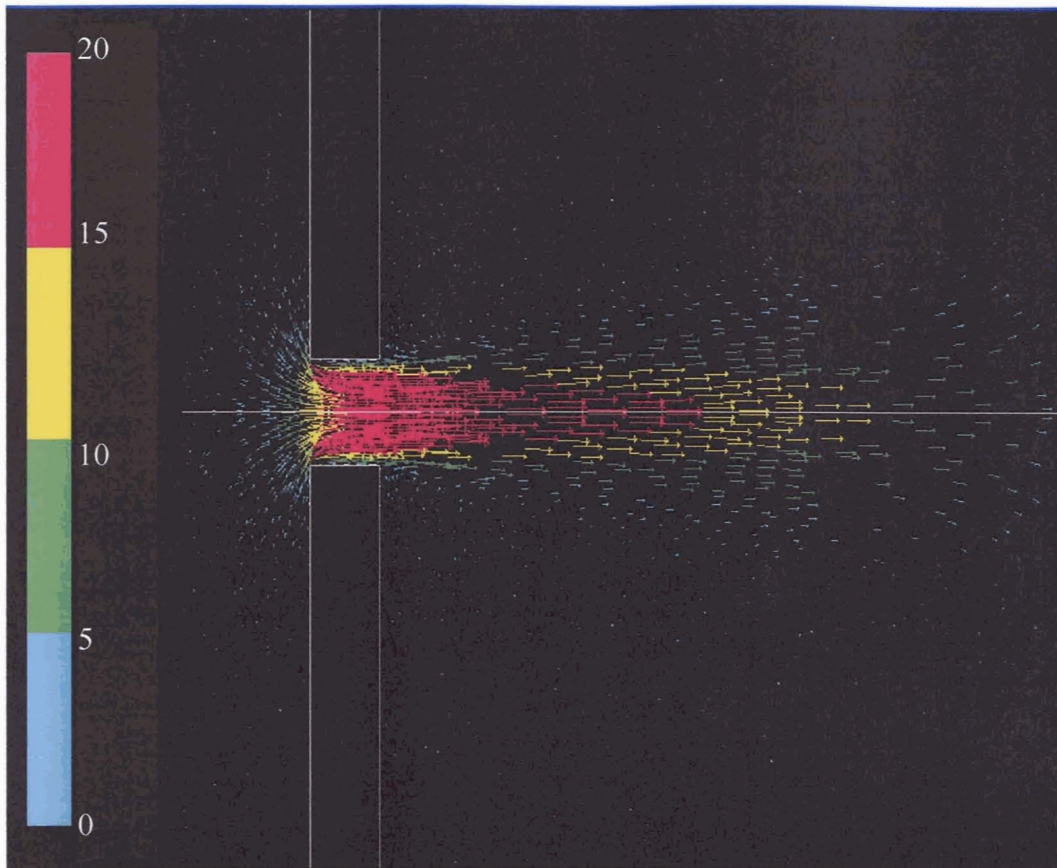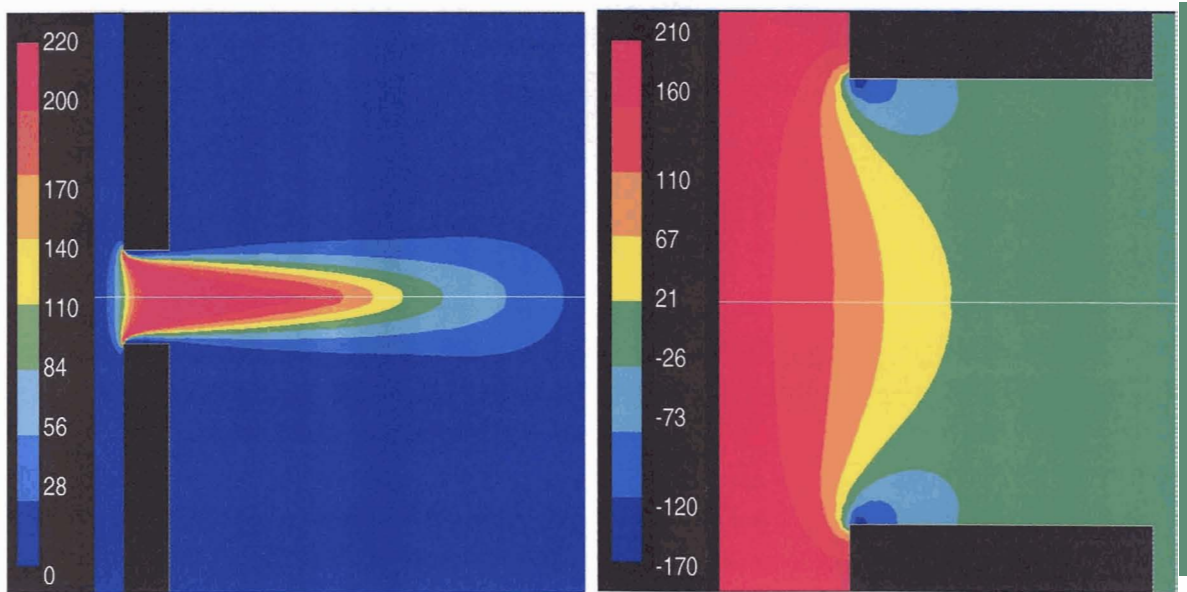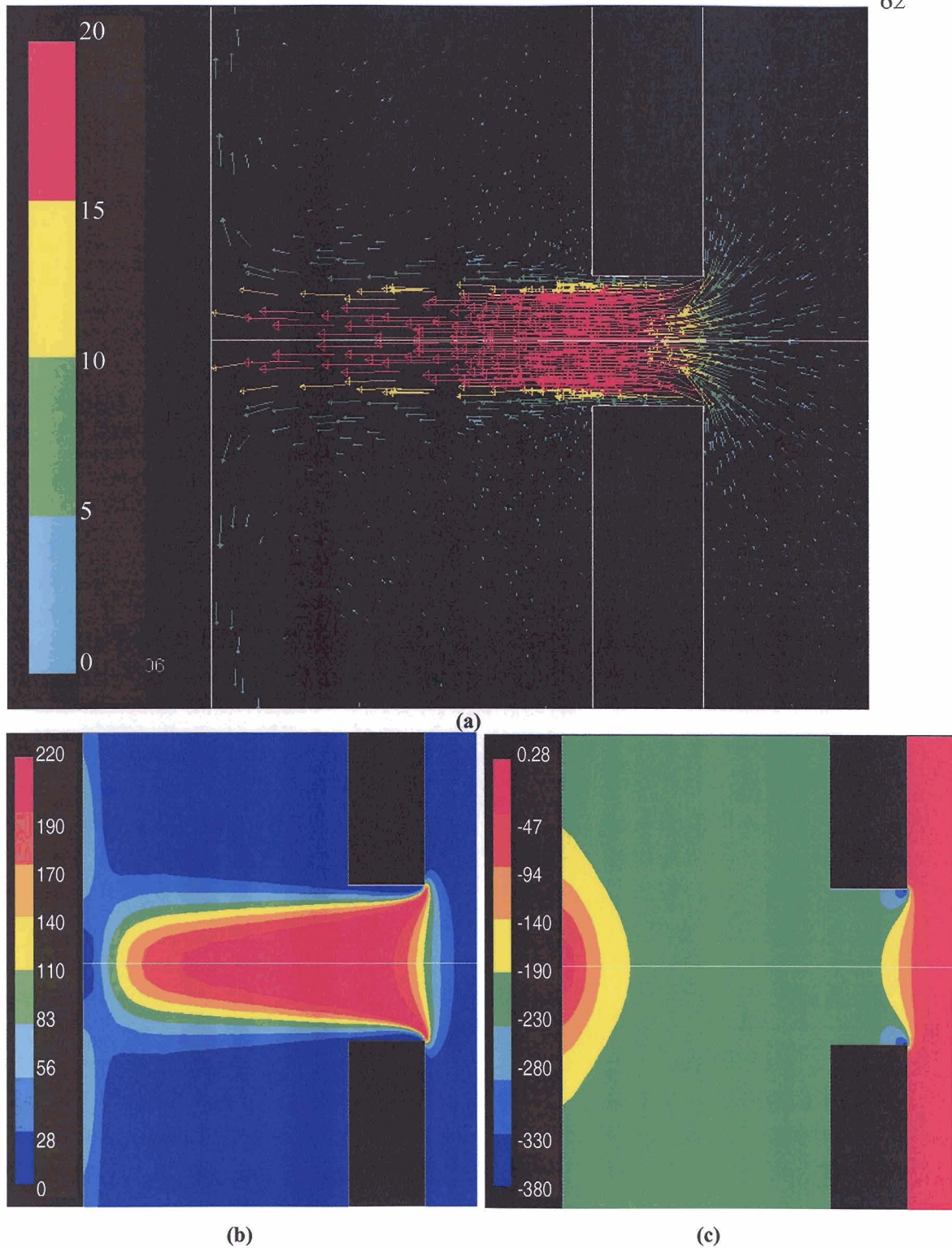
Figure 23 Bimorph Cavity II, Logarithmic Profile, maximum ingestion, t=0.75T (a) Velocity Vectors (m/s); (b) Contour Plots of Dynamic Pressure (Pa); (c) Contour Plots of Static Pressure (Pa)
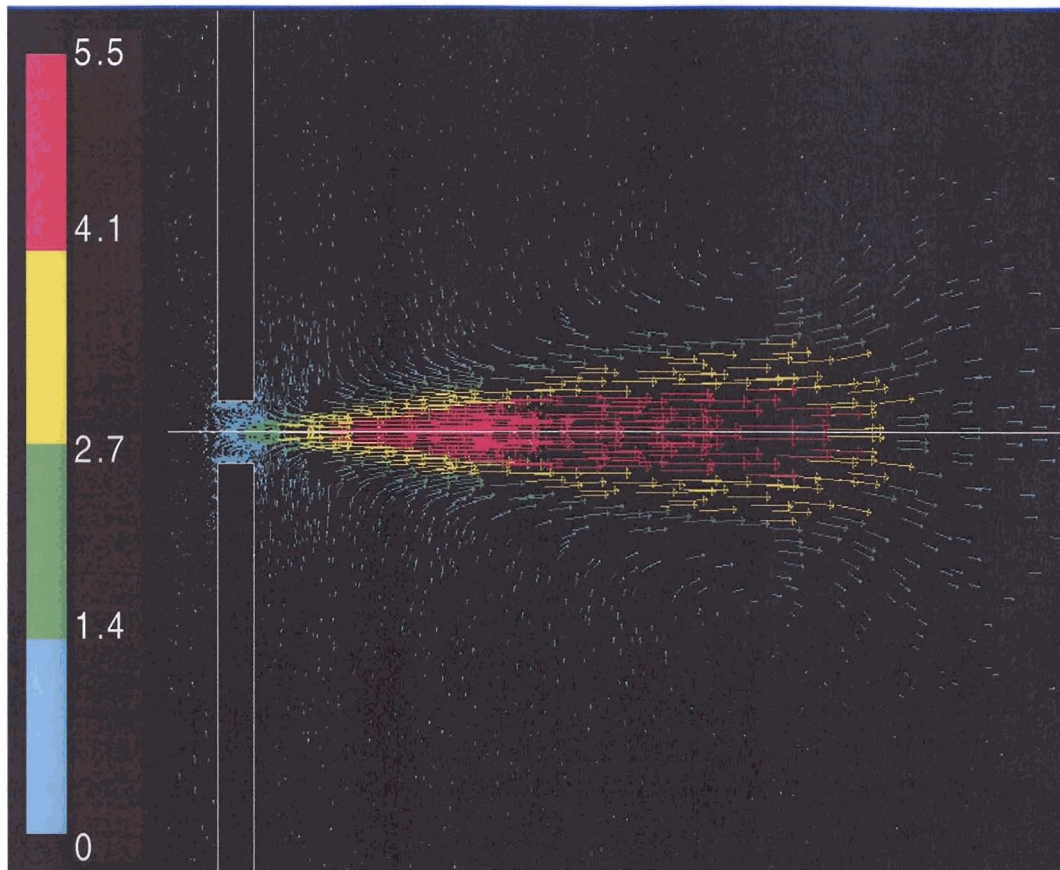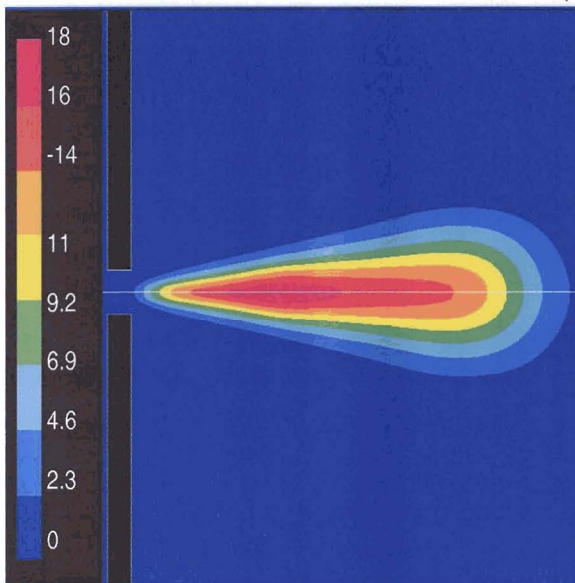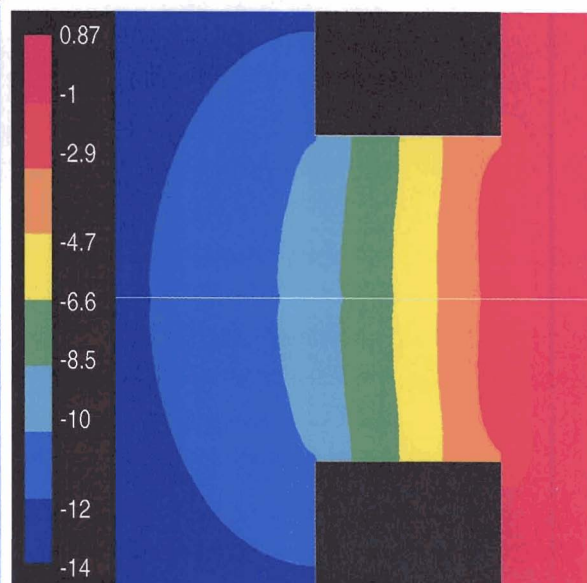
For the Bimorph Cavity II configuration, Figures 24a and 24b show the maximum measured experimental velocity and numerical velocity versus radial position at an axial distance of 2mm and a frequency of 50 Hz for the logarithmic and parabolic profile respectively. Similar to the Cavity I configuration the logarithmic profile for the Bimorph gives more accurate results than the parabolic profile.

The difference in the outer extremes of the numerical and experimental velocity magnitude (abs (r/D)>0.6) is due to the hot-wire inability of measuring flow direction. The higher maximum experimentally measured velocities observed in the outer portion of the jet most likely occurs during the ingestion cycle when the fluid flow is from the outer edges. If the negative numerical values attained during the ingestion cycle were entered as the absolute values in the velocity profile of maximum ingestion in Figures 24a and 24b, it would give a wider jet to resemble that of the experimental results.

A complete cycle for the center velocity (r = 0) at an axial distance of 2mm for 32Hz and 50Hz for the Cavity II configuration are shown in Figures 25a and 25b respectively. It can again be seen that for the Bimorph actuator a logarithmic profile displacement simulation gives a much more accurate prediction than the parabolic profile. The numerical logarithmic profile results match the 32Hz experimentally data and only over predicts the maximum measured experimental velocity at 50Hz by approximately 10%.

(a)

(b)
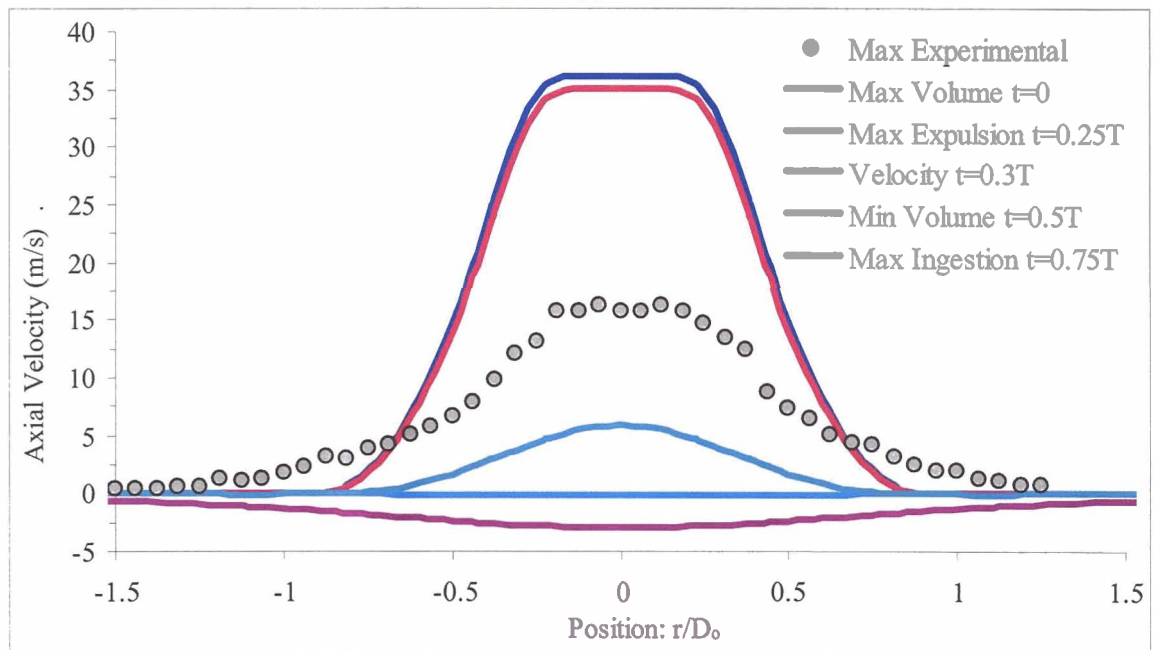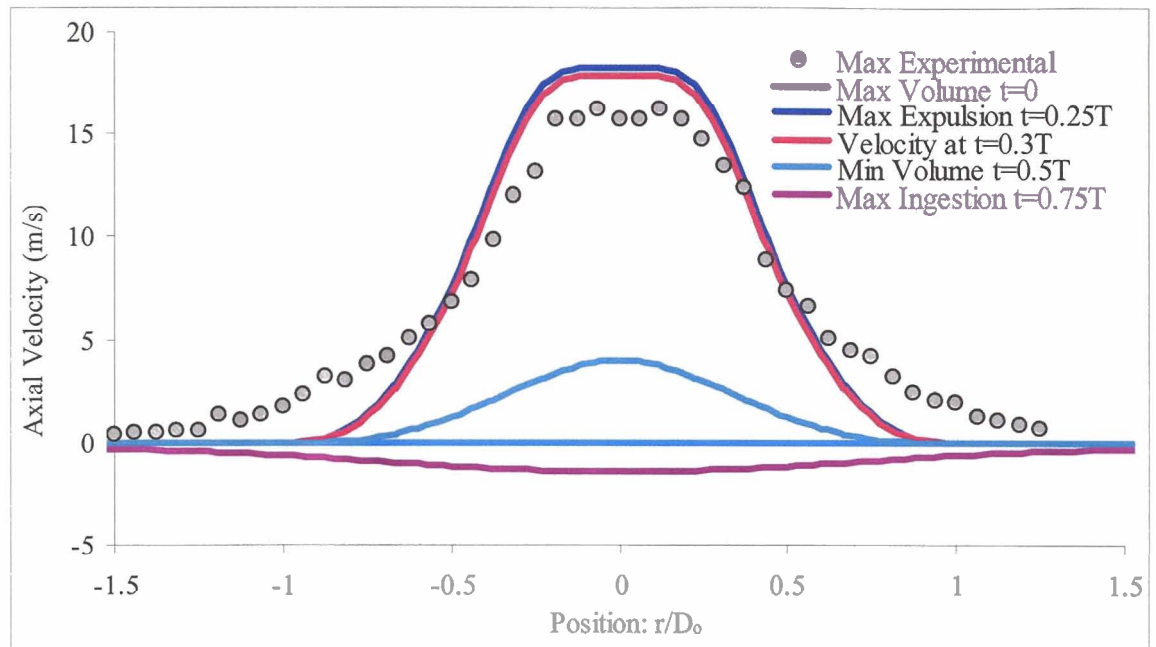
Figure 24 Bimorph Cavity II: Velocity vs. Radial Position at z=2mm for a) Logarithmic model, b) Parabolic model.
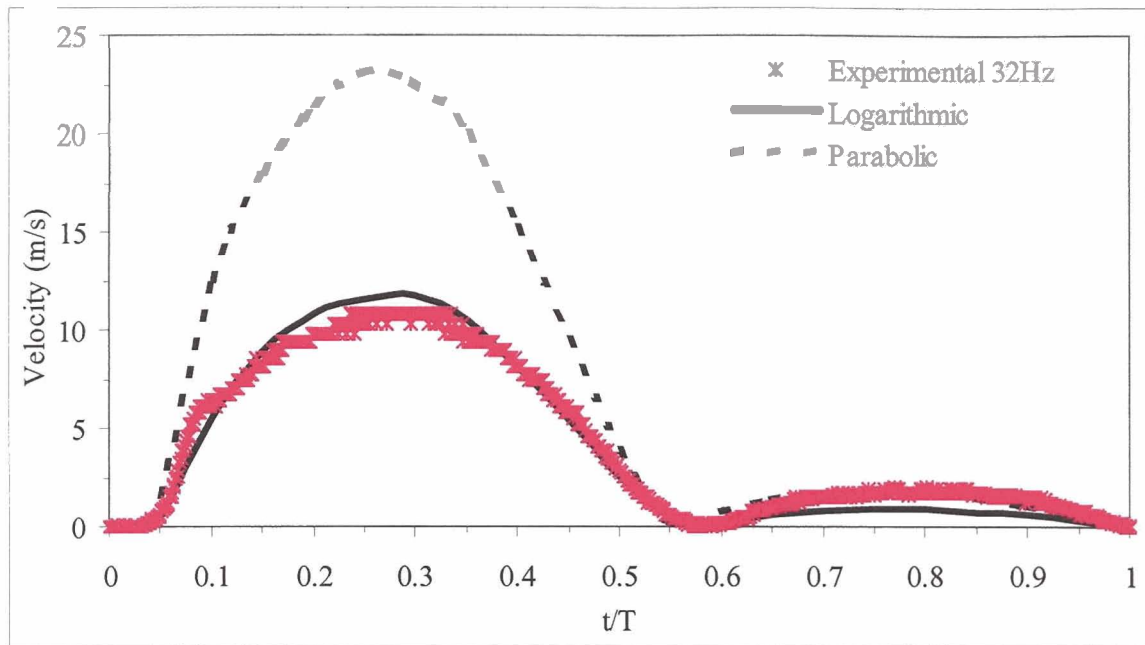
(a)
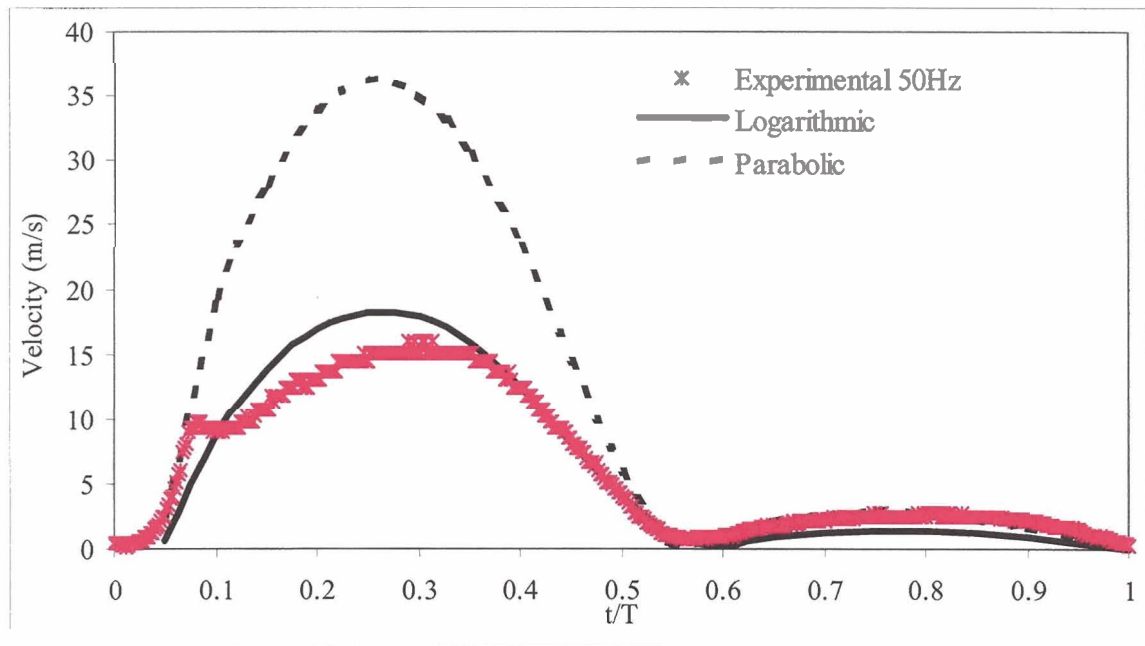
(b)

Figure 25 Bimorph Cavity II: Logarithmic and parabolic diaphragm profile center velocity vs. time comparison at z=2mm for a) 32Hz and b) 50Hz.

The maximum center velocity versus frequency at an axial distance of 2mm is shown in Figure 26. Similar to cavity I, the logarithmic diaphragm profile is a better approximation for the Bimorph in the cavity II configuration than the parabolic profile for all tested frequencies.
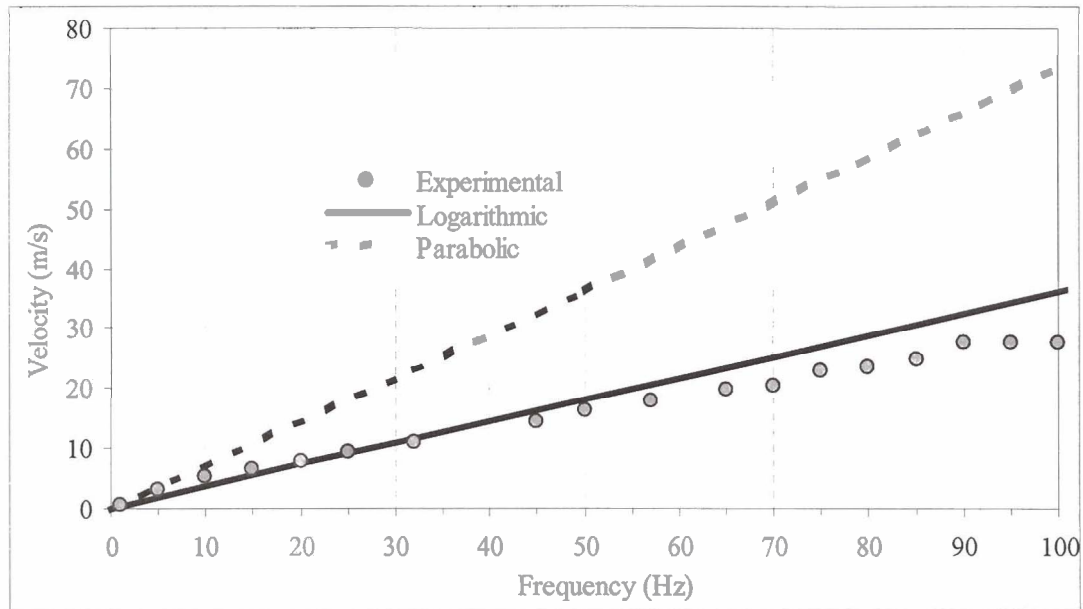
Figure 26 Bimorph Cavity II: Logarithmic and parabolic diaphragm profile max center velocity vs. frequency comparison at z=2mm.

4.3 Bimorph Cavity Height Variation Results

The cavity height dependence for the bimorph configuration was examined by maintaining all parameters the same and interchanging the cavity heights for cavity I and cavity II to produce two new configurations, cavity III and cavity IV shown in table 2, so that cavity I and cavity III have the same orifice diameter of 3.67mm while cavity II and cavity IV share corresponding orifice diameter of 2mm.

Table 2 Dimensions of tested cavities

	Cavity I	Cavity II	Cavity III	Cavity IV
(H_c) mm	9.55	5.5	5.5	9.5
(D_D) mm	60	60	60	60
(H_o) mm	1.6	1.6	1.6	1.6
(D_o) mm	3.67	2	3.67	2
δ_c	0.396	0.396	0.396	0.396
(f) Hz	50	50	50	50

A jet velocity comparison between the measured experimental and logarithmic displacement moving boundary numerical results for the Bimorph at the center (r = 0), and at an axial distance of 2mm for a frequency of 50Hz for the cavity configurations I and III is shown in Figures 27. A similar plot comparing the center jet velocity for the Bimorph in the cavity II and cavity IV is shown in Figure 28.
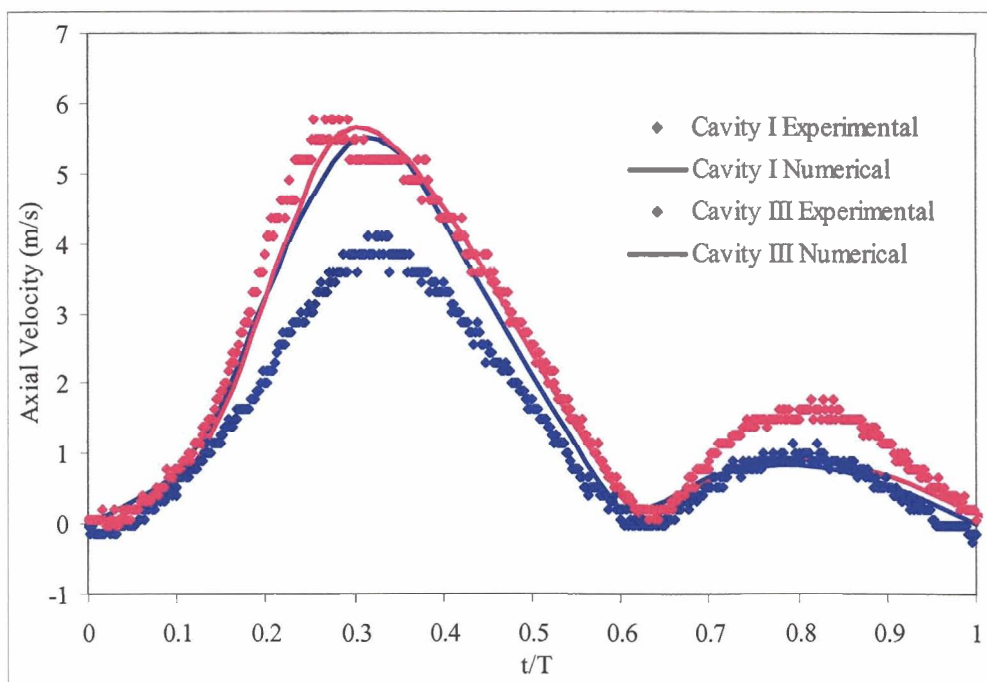
Figure 27 Bimorph logarithmic diaphragm profile cavity I and cavity III experimental and numerical results center velocity vs. time comparison at z=2mm for 50Hz.
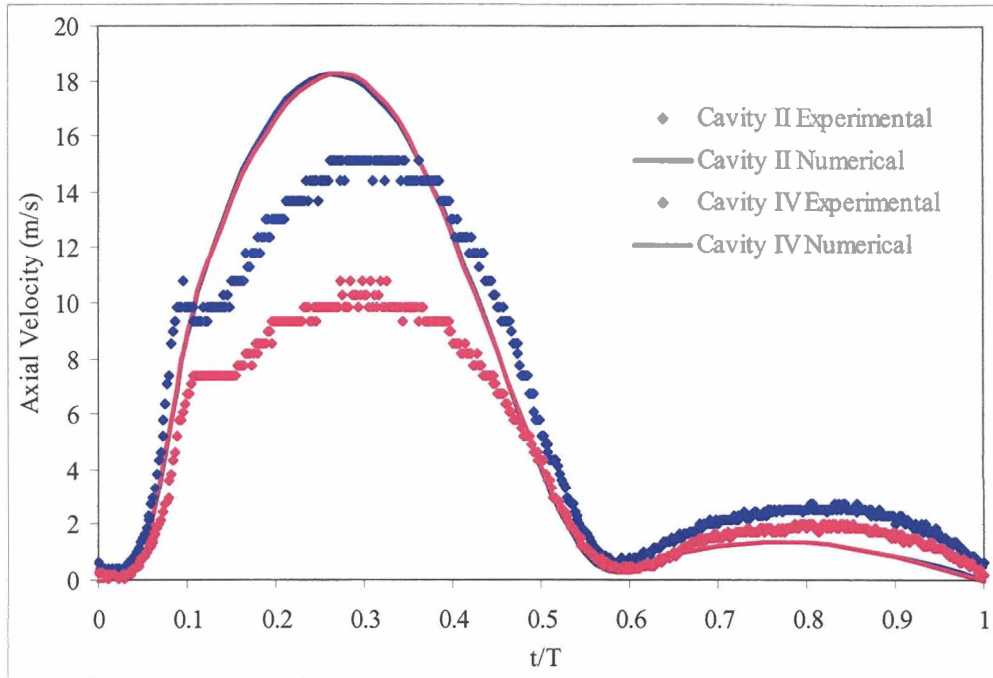
Figure 28 Bimorph logarithmic diaphragm profile cavity II and cavity IV experimental and numerical results center velocity vs. time comparison at z=2mm for 50Hz.

It is evident that a smaller cavity height gives higher experimental velocities for the two orifice diameters of 3.67mm (cavity I and cavity III) and 2mm (cavity II and cavity IV) this however is not the case for the numerical results. The experimental data shows that the center velocity at an axial distance of 2mm is approximately 30% larger for both orifice diameters small cavity configurations cavity II and cavity III when compared to the larger cavity height configurations of cavity I and cavity IV. Cavity height for the numerical model made no difference at all. The jet velocity independence of the cavity height for the numerical model which was also observed for the control case cavity can be most likely attributed to the fact that only the height and not the actual cavity volume is taken into account for the developed 2-dimensional numerical model.

Pressure and actuator displacement dynamic coupling is not taken into account meaning that the displacement of the diaphragm for the numerical model is non-reactive to the oscillating cavity pressure developed. Furthermore the model does not take into account the dynamic cavity pressure and diaphragm deflection interaction. The pressure developed inside the cavity will be important when considering the dynamic coupling that will result from the developed pressure and the diaphragm displacement interaction. Morgan Electro Ceramics [49] offers the following simplified center displacement empirical formulas for PZT flexural membrane elements dependent on the Diaphragm diameter, D_D, Ceramic Thickness, t_{Dc}, and peak-to-peak input voltage, $\cup$.

$$\delta_C = 10^{-10} \frac{D_D{}^2}{t_{Dc}{}^2} \cup \qquad \text{Equation 42}$$

Which for the current Bimorph actuator are: Diaphragm diameter, D_D = 0.0984m; Ceramic Thickness, t_{Dc} = 0.63mm; and peak-to-peak input voltage $\cup$ = 150V; gives a center displacement, δ_C = 0.366mm. Although equation 42 is for an entirely PZT layer the calculation approximation for the Bimorph actuator is fairly close to the actual measured center displacement of δ_C = 0.396 mm. The larger measured Bimorph displacement is due to the fact that the bimorph is composed of two PZT layers and not a single PZT layer. Based on the center approximation it is warranted to use the following simplified empirical formula also offered by Morgan Electro Ceramics [49] for PZT flexural membrane elements to approximate the diaphragms blocking pressure,

$$P_b = 8 \frac{t_{Dc}}{D_D{}^3} \cup \qquad\qquad \text{Equation 43}$$

For the given diaphragm diameter, ceramic thickness and peak-to-peak input voltage a blocking pressure, P_b = 793 Pa. From Figures 21c and 23c, for the static pressure at the maximum expulsion and maximum ingestion respectively for the cavity II configuration it can be seen that the calculated blocking pressure is comparable to the static pressure developed inside the cavity for the Bimorph in the cavity II configuration during maximum expulsion and maximum ingestion. In both cases, maximum expulsion and maximum ingestion the pressure developed inside the cavity opposes the movement of the oscillating diaphragm. During maximum expulsion the pressure inside the cavity predicted by the moving boundary model is 210 Pa, which is over 25% of the calculated blocking pressure. During maximum ingestion there is a vacuum inside the cavity that ranges from approximately 0 to –100 Pa localized at the center diaphragm to approximately –230 Pa around the actuators perimeter. These preliminary results suggest that the pressure developed inside the cavity will be significant when considering the displacement-pressure coupling of the actuator and cavity and will thus require further experimental and numerical investigation.

4.4 Thunder Results

4.4.1 Thunder Cavity I Results

The following section is for the Thunder actuator in the cavity I configuration. The experimentally measured and numerically used peak-to-peak center diaphragm displacement, δ_C, for the Thunder actuator is 0.07mm.

For the numerical velocity profiles the maximum volume at $t = 0$ occurs when the diaphragm is at its lowest point (furthest from orifice; $t = 0$), and the cavity has maximum fluid volume; maximum expulsion at $t = 0.25T$ corresponds to when the diaphragm is at level position and moving with maximum velocity towards the orifice; minimum volume occurs halfway through the cycle at $t = 0.5T$ when the diaphragm is at the highest position (closest to orifice) and the volume of fluid in the cavity is at a minimum; maximum ingestion at $t = 0.75T$, corresponds to when the diaphragm is at level position and moving with maximum velocity away from the orifice. The velocity magnitude vector plots, dynamic pressure and static pressure contours for each of these stages for the parabolic profile for the Thunder actuator are shown in Figures 29 through 32.

Maximum cavity volume at t = 0 in Figure 29 shows the synthetic jet that follows the completed ingestion part of the cycle. Vortices that developed inside the cavity during the ingestion cycle are evident in the vector plot, Figure 29a. Unlike the Bimorph actuator, both cavities, the fluid that is pulled inside the cavity I configuration for the Thunder actuator, does not create a localized higher-pressure area at the back wall of the cavity since the relatively slow jet (1.2 m/s) does not reach the back of the wall. Instead Figure 29c shows a higher pressure of approximately 2.3 Pa distributed within the cavity. From

the vector plots of Figure 29a the remains of the slug of fluid that developed during the expulsion part of the cycle, only about $2H_o$ (cavity height, 1.9mm) from the exit orifice, are evident.

At maximum expulsion at t = 0.25T, Figures 30a-30c shows the vector and pressure plots of the synthetic jet. At this point the diaphragm is at the neutral position and moving toward the orifice with maximum velocity. Shedding vortices that have just begun to develop are shown in a vector plot Figure 30a. The spreading of the synthetic jet begins within $1H_o$ (cavity height, 1.9mm) where the remains of the ingested slug is still visible, and the maximum observed velocity outside the cavity is 2m/s. The static pressure contour plot, Figure 30c, shows that a high pressure of 2.2Pa is present inside the cavity and shows a low pressure of –2.7Pa at the corners of the orifice inlet.
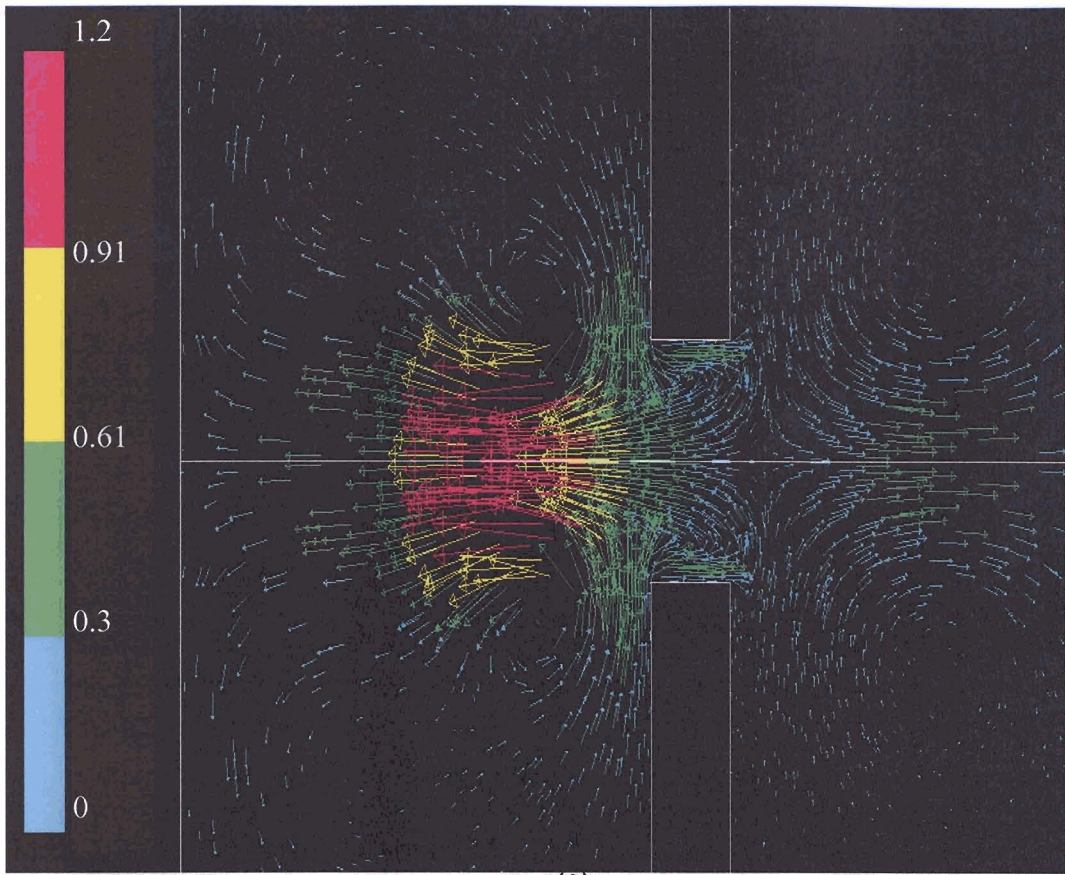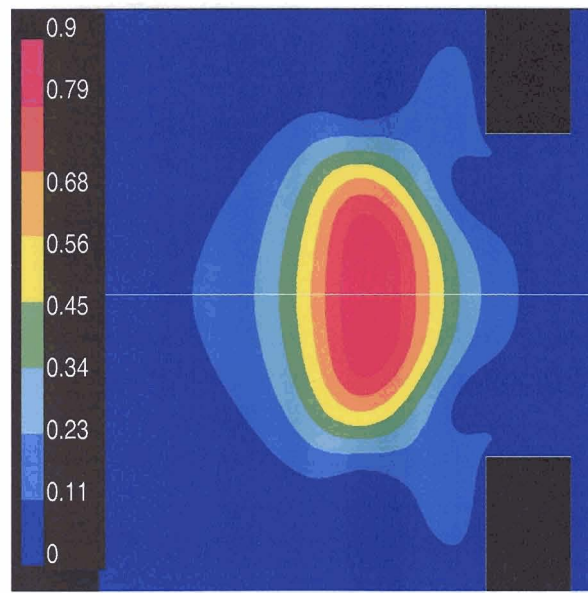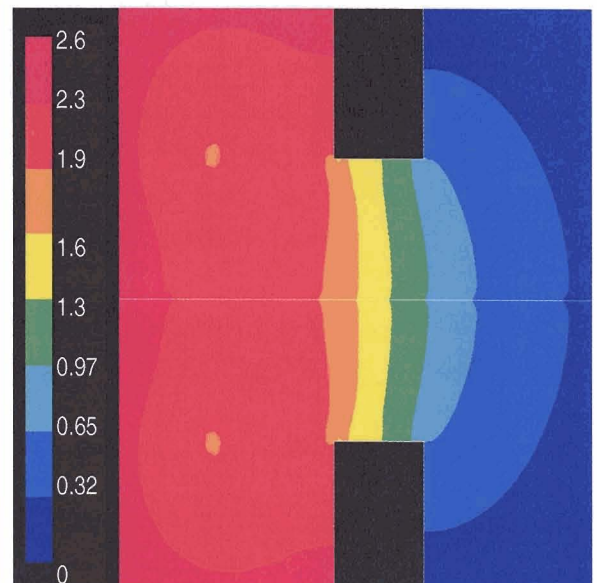
Figure 29 Thunder Cavity I, t=0 Maximum Cavity Volume (a) Velocity Vectors (m/s); (b) Contour Plots of Dynamic Pressure (Pa); (c) Contour Plots of Static Pressure (Pa)

Figure 30 Thunder Cavity I, t=0.25T, Maximum Expulsion, (a) Velocity Vectors (m/s); (b) Contour Plots of Dynamic Pressure (Pa); (c) Contour Plots of Static Pressure (Pa)

At minimum cavity volume, t = 0.5T, Figure 31a and 31b shows that the expelled slug of air has still not fully developed as did in the Bimorph actuator. The maximum velocity has decreased slightly from the maximum expulsion at t = 0.25T of 2m/s to 1.1m/s. The ingested slug of air is still clearly visible inside the cavity. The static pressure plot, Figure 31c, shows that a vacuum of –2.7Pa has developed inside the cavity.

Finally at the maximum ingestion, t = 0.75T, Figure 32, shows reverse similarities to the maximum expulsion plots of Figure 30, with the same velocity magnitude and developing vortices in the opposite direction. The plot of the static pressure, Figure 32c, also shows that low pressure points develop as in the case of the maximum ingestion plot, Figure 30c, but instead of the corners of the orifice inlet the low pressure of –4.9Pa is located at the orifice outlet.

For the Thunder Cavity I configuration Figures 33a and 33b show the maximum measured experimental velocity and numerical velocity versus radial position at an axial distance of 2mm and a frequency of 50 Hz for the logarithmic and parabolic diaphragm profile displacement respectively.
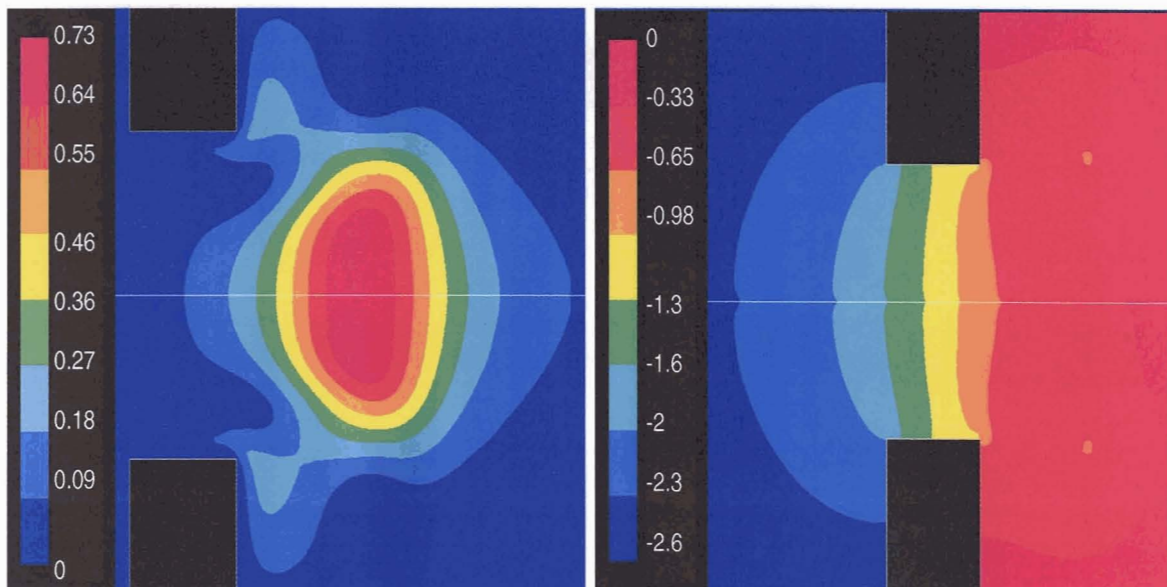
Figure 31 Thunder Cavity I, t=0.5T Minimum Cavity Volume (a) Velocity Vectors (m/s); (b) Contour Plots of Dynamic Pressure (Pa); (c) Contour Plots of Static Pressure (Pa)
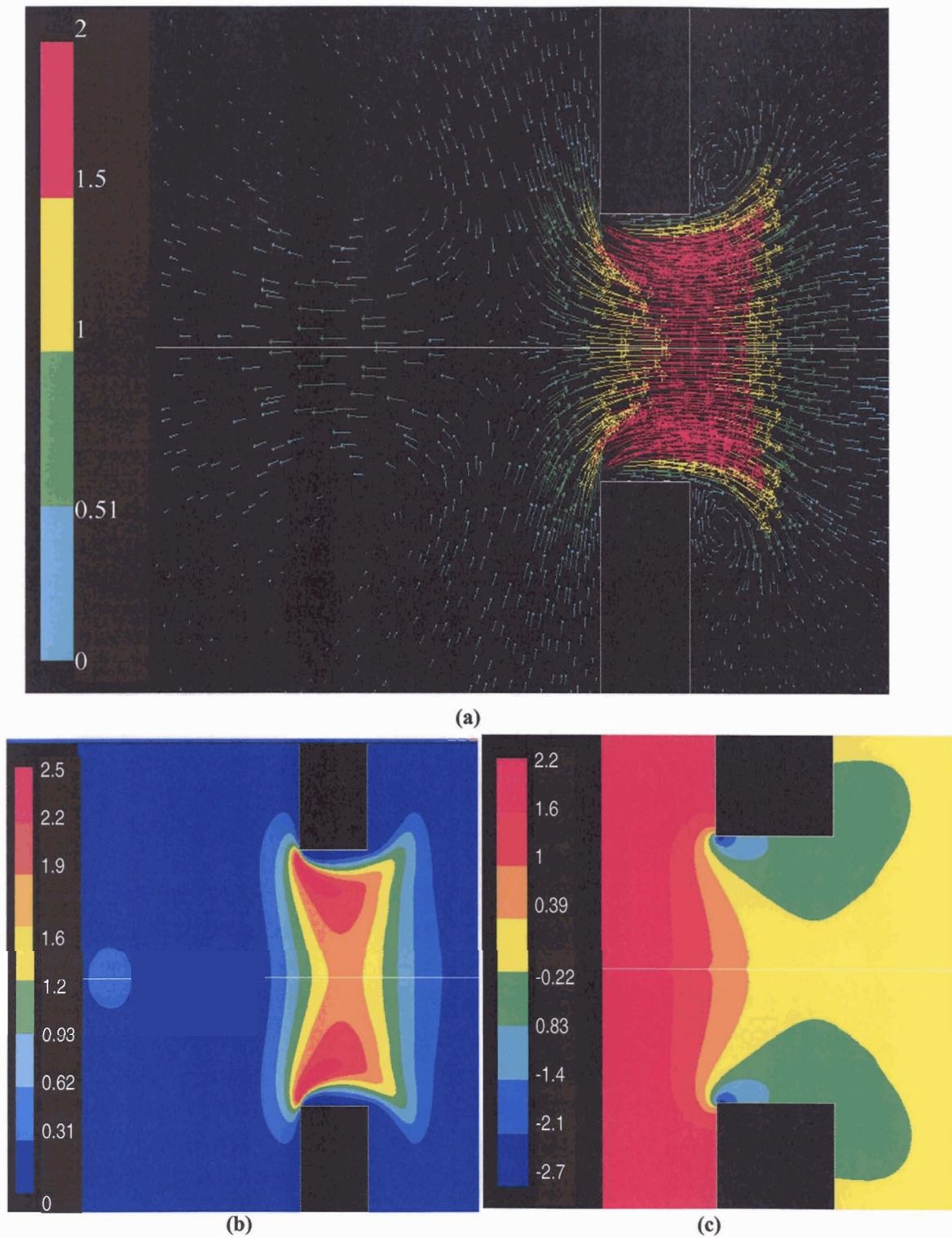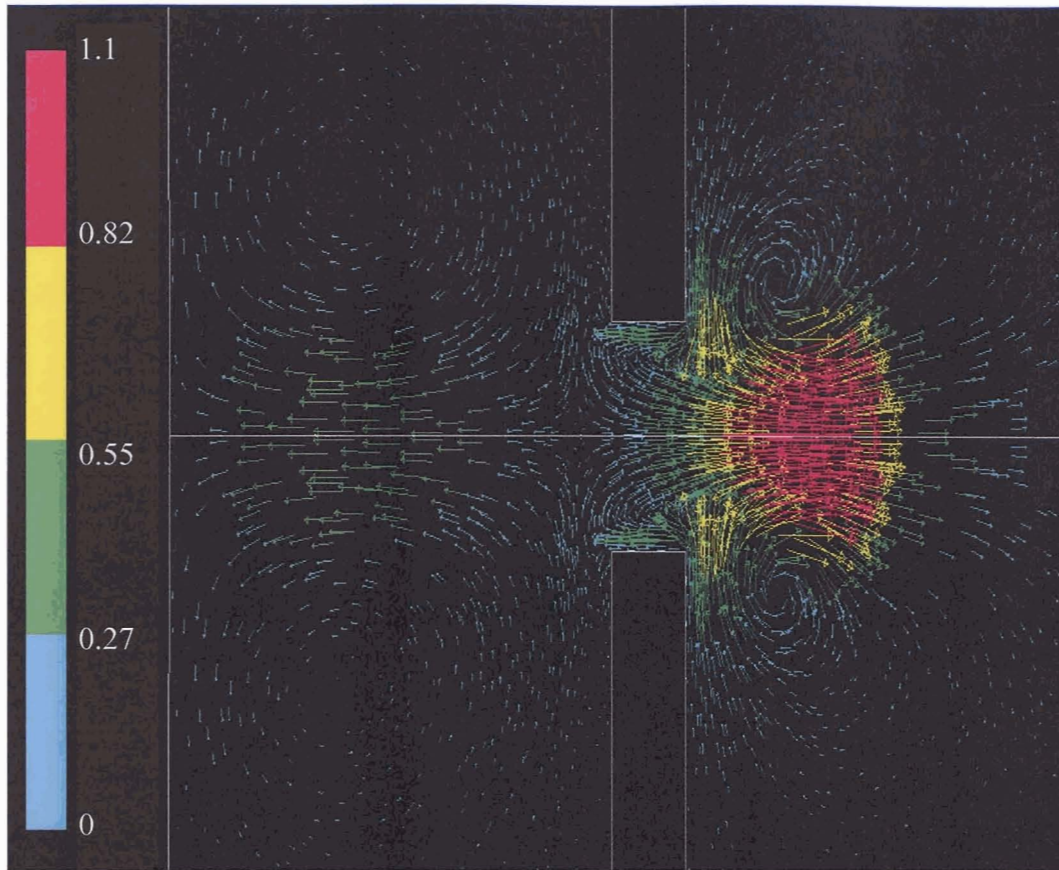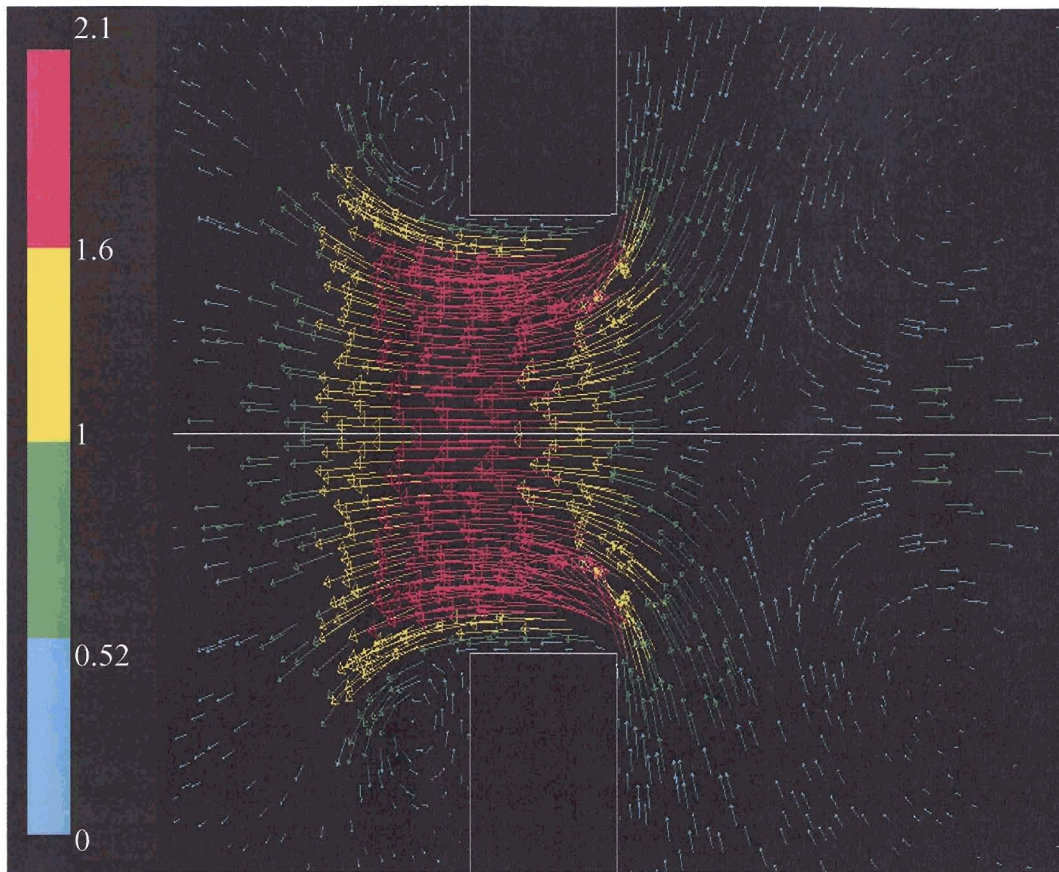
(a)
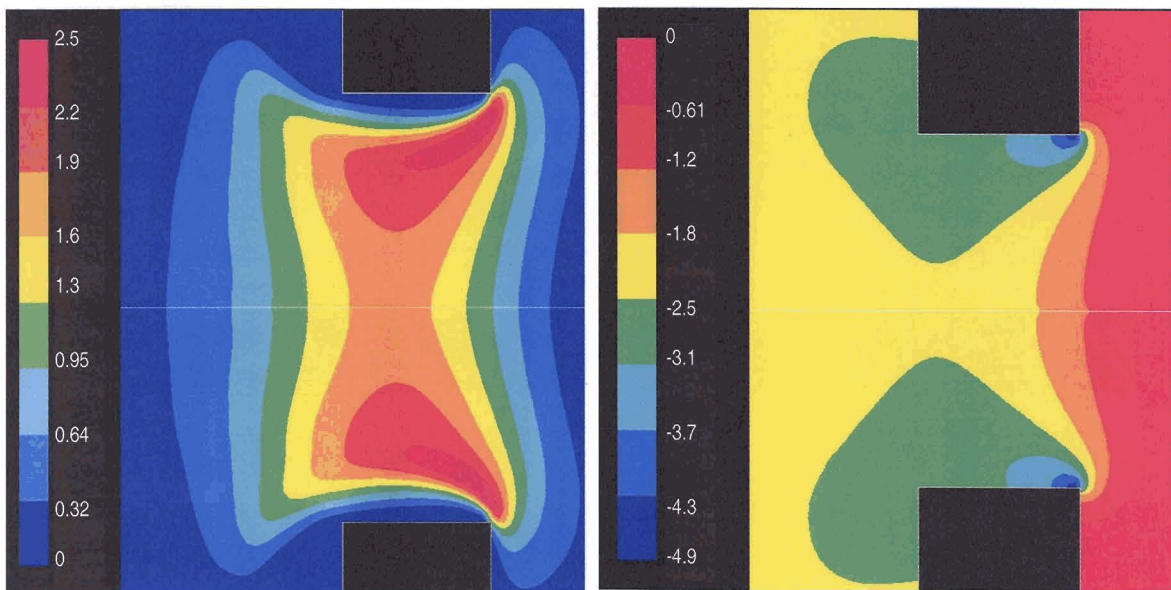
(b)

(c)

Figure 32 Thunder Cavity I, t=0.75T Maximum Ingestion (a) Velocity Vectors (m/s); (b) Contour Plots of Dynamic Pressure (Pa); (c) Contour Plots of Static Pressure (Pa)
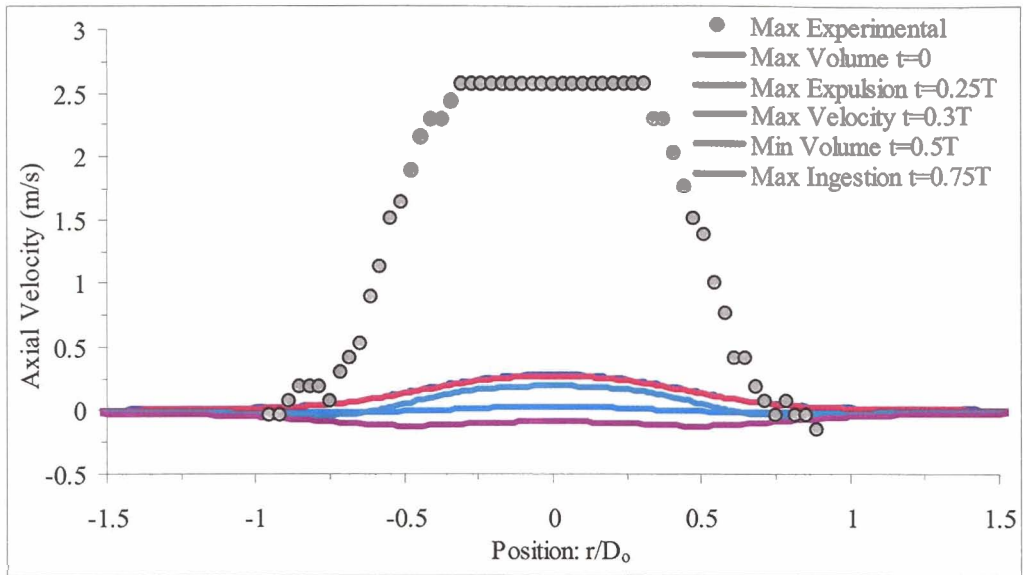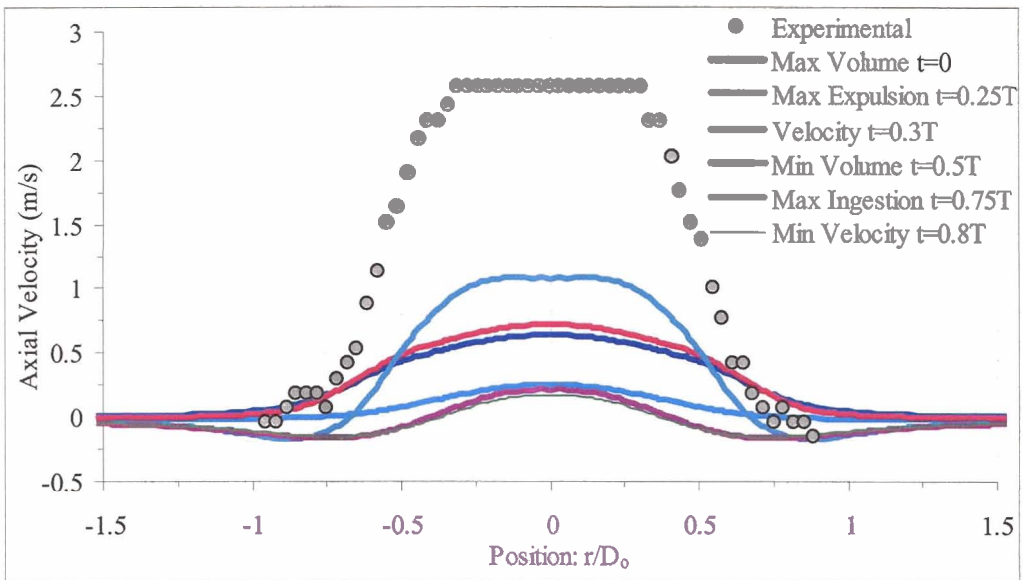
Figure 33 Thunder Cavity I: Velocity vs. Radial Position at z=2mm for a) Logarithmic model, b) Parabolic model.

It is apparent from Figures 33a and 33b that neither the logarithmic nor the parabolic model gives accurate results for the Thunder actuator, with both models under predicting the measured experimental results. One possible reason for this inaccuracy is thought to be due to the shape of the Thunder actuator. To test this hypothesis we account for the Thunder shape with two asymmetrical parabolic displacements models in which the peak-to-peak displacement, δ_C = 0.07 mm is entirely away from the orifice or toward the orifice. This modification to the diaphragm movement is accomplished by simply changing the cosine term in equation 4, for the velocity input to a negative sine term in the case when the diaphragm is moving away from the orifice as shown in Equation 44.

$$u(r,t) = \left[-f\pi\delta_C \sin(2\pi ft) + f\pi\delta_C \sin(2\pi ft)\left(\frac{r}{(D_D/2)}\right)^2 \right]$$ Equation 44

When is moving towards the orifice, a positive sine term as shown in Equation 45.

$$u(r,t) = \left[f\pi\delta_C \sin(2\pi ft) - f\pi\delta_C \sin(2\pi ft)\left(\frac{r}{(D_D/2)}\right)^2 \right]$$ Equation 45

In the case when the entire movement is away from the orifice the diaphragm begins at the level position or minimum volume at t = 0., It then moves away from the orifice and reaches the maximum ingestion, t = 0.25T, which corresponds to the position where the diaphragm is moving with maximum velocity away from the orifice, at t = 0.5T; the diaphragm reaches the lowest point maximum volume, with a center distance of 0.07mm below the level point. The maximum expulsion occurs at t = 0.75T when the diaphragm is moving with maximum velocity towards the orifice before returning to the level position or minimum volume at t = 1T.

In the case when the entire movement is toward the orifice the diaphragm, the level position maximum volume at t = 0 starts. It then moves toward the orifice and reaches the maximum expulsion point at t = 0.25T, at which the diaphragm is moving with maximum velocity toward the orifice. At t = 0.5T the diaphragm reaches the highest point or minimum volume, with a center distance of 0.07mm above the level point. The maximum ingestion occurs at t = 0.75T when the diaphragm is moving with maximum velocity away from the orifice before returning to the level position or maximum volume at t = 1T.

Velocity versus radial position plots for the case in which the diaphragm is moving away from the orifice [(-) Parabolic)] and when it is moving toward the orifice [(+) Parabolic] are shown in Figures 34a and 34b respectively. These Figures also show that both the (-) Parabolic and (+) Parabolic profile give higher velocity values that better approximation of the experimental values for the Thunder actuator in the cavity I configuration.
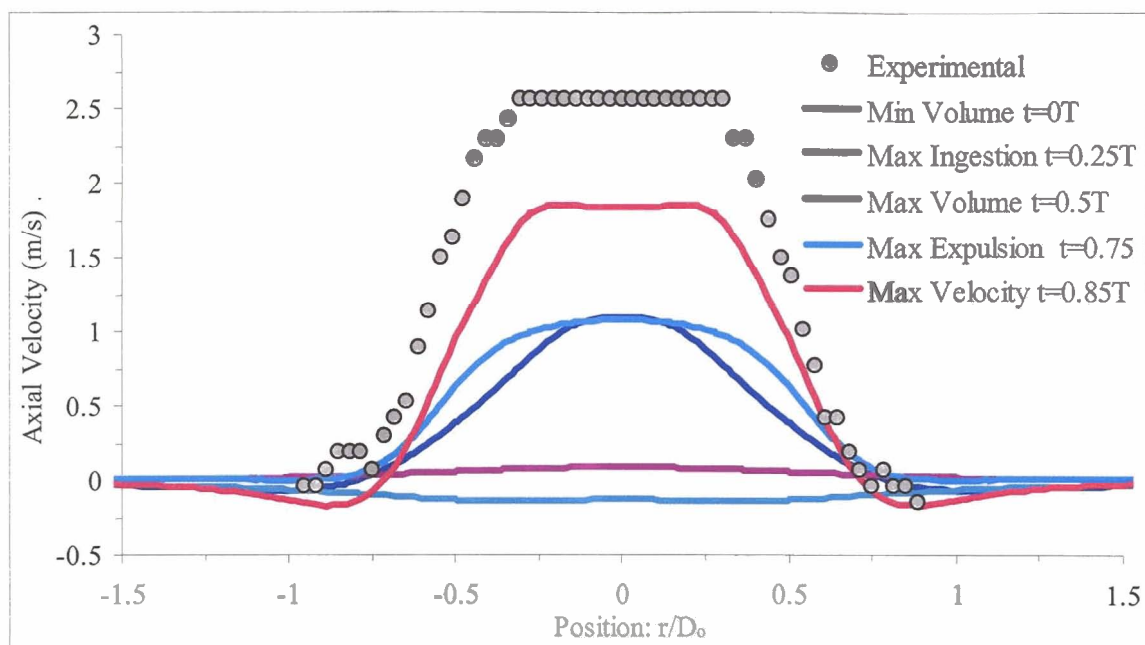
(a)
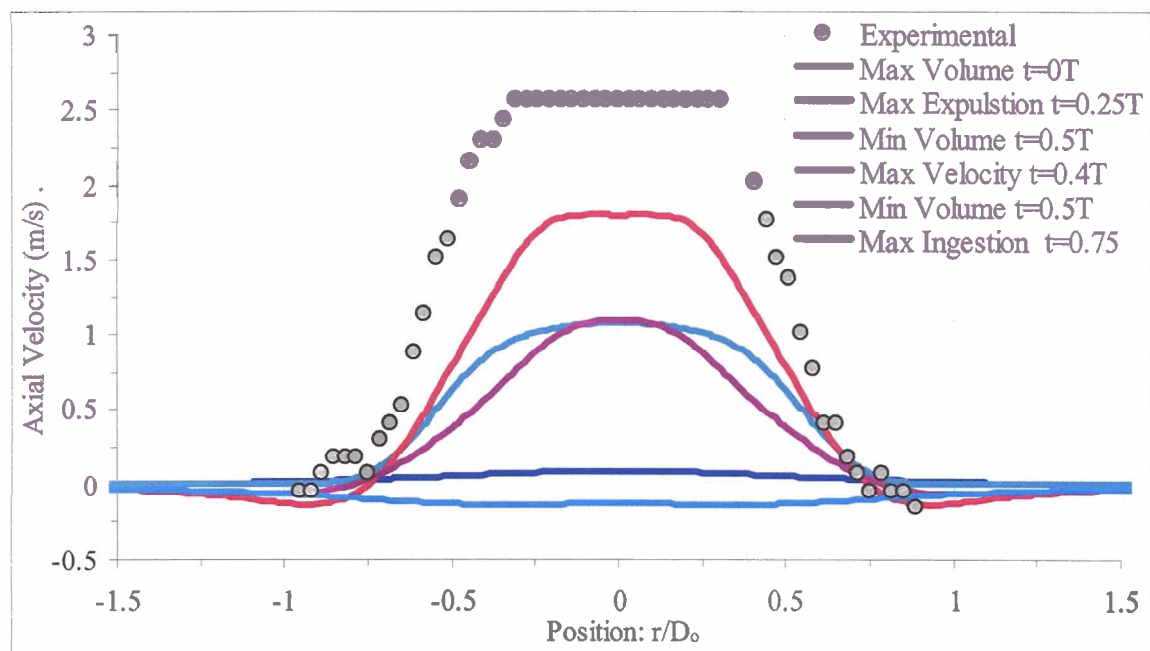
(b)

Figure 34 Thunder Cavity I: Velocity vs. Radial Position at z=2mm for a) Moving away from orifice Parabolic model and b) Moving toward orifice parabolic model.

A complete cycle for the center velocity (r = 0) at an axial distance of 2mm for 32 Hz and 50 Hz for the Cavity I configuration are shown in Figures 35a and 35b respectively. For both of these frequencies, the asymmetrical parabolic displacement profiles give a better approximation to the measured experimental velocity.
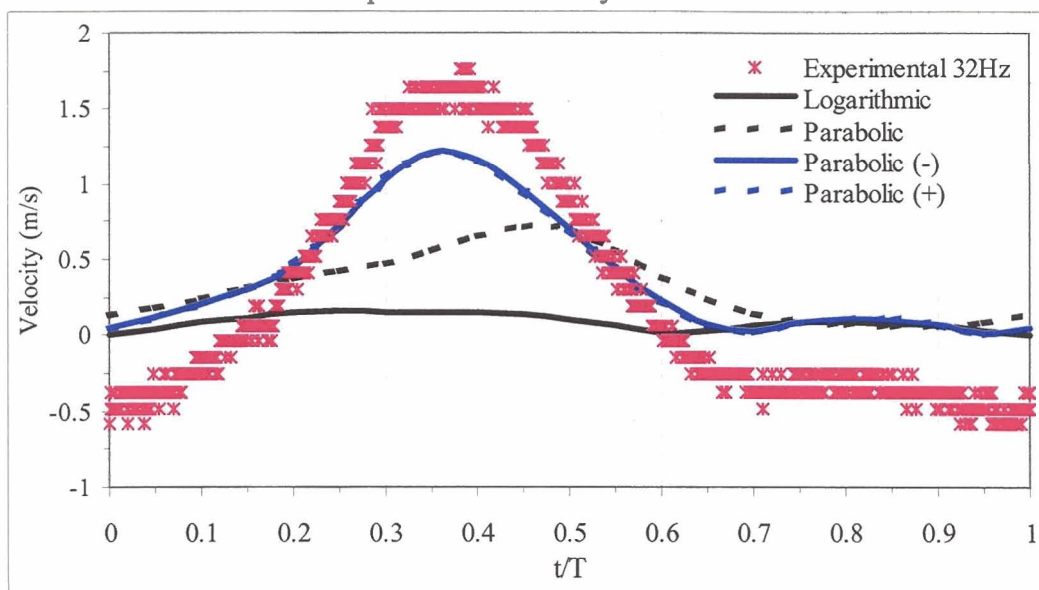
(a)
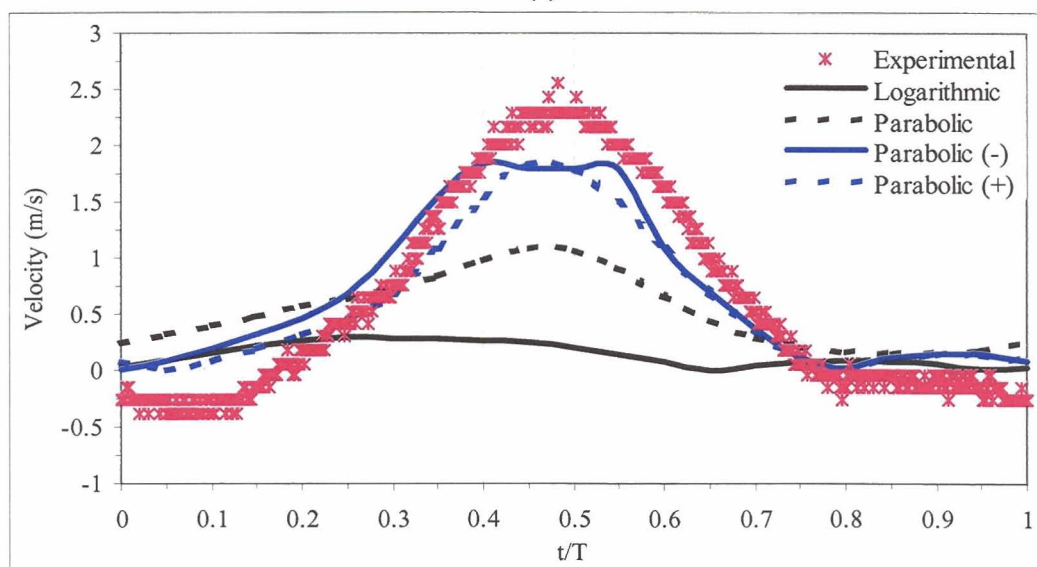
(b)

Figure 35 Thunder Cavity I: Logarithmic and parabolic diaphragm profiles center velocity vs. time comparison at z=2mm for a) 32Hz and b) 50Hz.

The maximum center velocity versus frequency at an axial distance of 2mm is shown in Figure 36 for the Thunder actuator in the cavity I configuration. Both the logarithmic and parabolic profile under predict the experimentally measured velocity values for all tested frequencies. The parabolic profile however is more accurate.
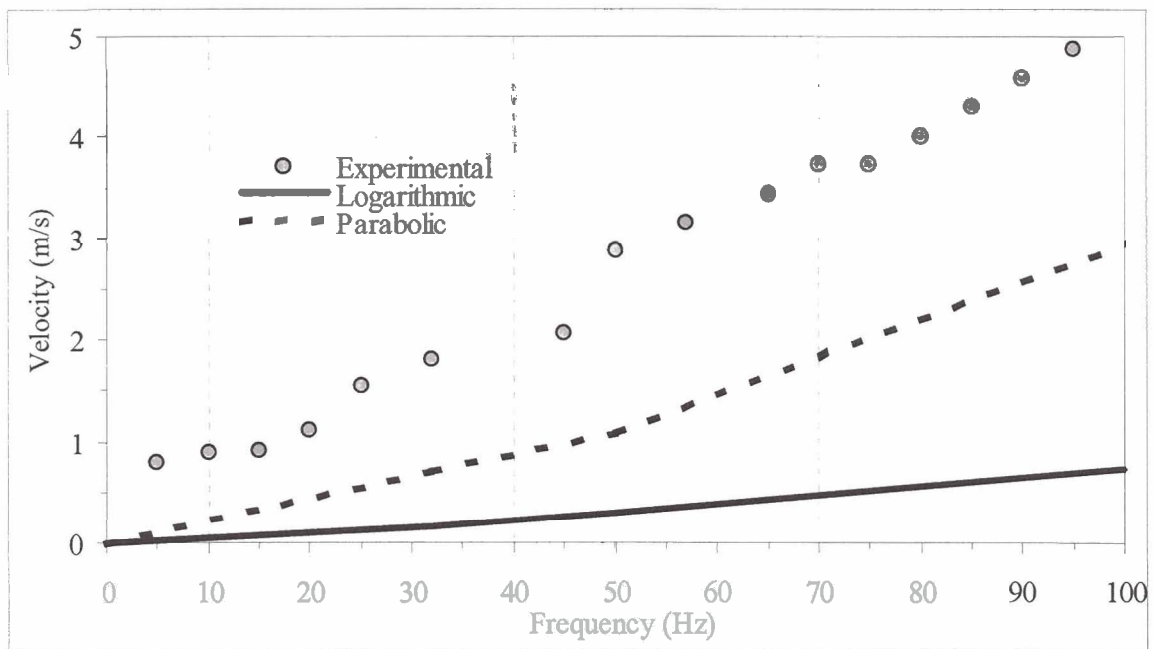
Figure 36 Thunder Cavity I: Logarithmic and parabolic diaphragm profile max center velocity vs. frequency comparison at z=2mm.

4.3.2 Thunder Cavity II Results

The following section is for the Thunder actuator in the cavity II configuration. Velocity vector and pressure plots for the parabolic velocity profile at the four times, Figures 37 through 40, show at maximum volume, t = 0, maximum expulsion t = 0.25T, minimum volume t = 0.5T, and maximum ingestion, t = 0.75T, as described in section 4.3.1.

At maximum volume t = 0, Figure 37a, shows that for the smaller orifice and cavity configuration the jet ingested inside the cavity has twice as high velocity magnitude, 2.5m/s than the cavity I configuration, 1.2m/s. Unlike cavity I, the fluid that is pulled inside the cavity II configuration for the Thunder actuator creates a localized higher-pressure area at the back wall of the cavity similar to the Bimorph actuator. Figure 37c shows that the pressure of the faster incoming slug of fluid that hits the back of the wall cavity is approximately 10Pa.

At maximum expulsion, Figures 38a-38c, shows the vector and pressure plots of the synthetic jet at t = 0.25T. At this point the diaphragm is at the neutral position and moving toward the orifice with maximum velocity. The jet at this point for the cavity II configuration has a higher maximum velocity, of 6.7m/s, and does not spread as in the cavity I configuration. The width of the jet of fluid for the most part remains the size of the orifice with the shedding vortices just beginning to form at the leading edge of the slug of air at approximately $3H_o$ away from the orifice exit. The range of the static pressure for the cavity II configuration ranges from −18Pa at the corners of the orifice inlet to 29Pa in the inside of the cavity.

At minimum cavity volume, t = 0.5T, Figure 39a and 39b show the formation of the fluid slug that has developed and nearly completely separated. The maximum velocity has decreased significantly from the maximum expulsion at t = 0.25T of 6.7m/s to 2.9m/s. The vortices that develop further from the orifice exit for the cavity II configuration are bigger and less evident than the cavity I configuration. The static pressure plot, Figure 39c, shows a small pressure gradient across the orifice that starts at −6.4Pa inside the cavity to

0Pa at the orifice exit. The static plot also captures the slightly lower pressure of the two vortices.

For the maximum ingestion, Figure 40 at t = 0.75T, the same velocity magnitude but in the opposite direction of the maximum expulsion at t = 0.25T is observed. Unlike the maximum ingestion of cavity I, for cavity II the leading edge of the ingested slug of air has already hit the back of the cavity wall. The vortices of the ingested slug of fluid are visible towards the leading edge of the slug. The plot of the static pressure, Figure 40c, also shows the low pressure points develop as in the case of the maximum ingestion plot, Figure 38c, but instead of the corners of the orifice inlet the low pressure is located at the orifice outlet. This low pressure of −46Pa is lower than the cavity I configuration of − 4.9Pa. At this point the majority of the inside of the cavity is a vacuum at approximately - 30Pa.
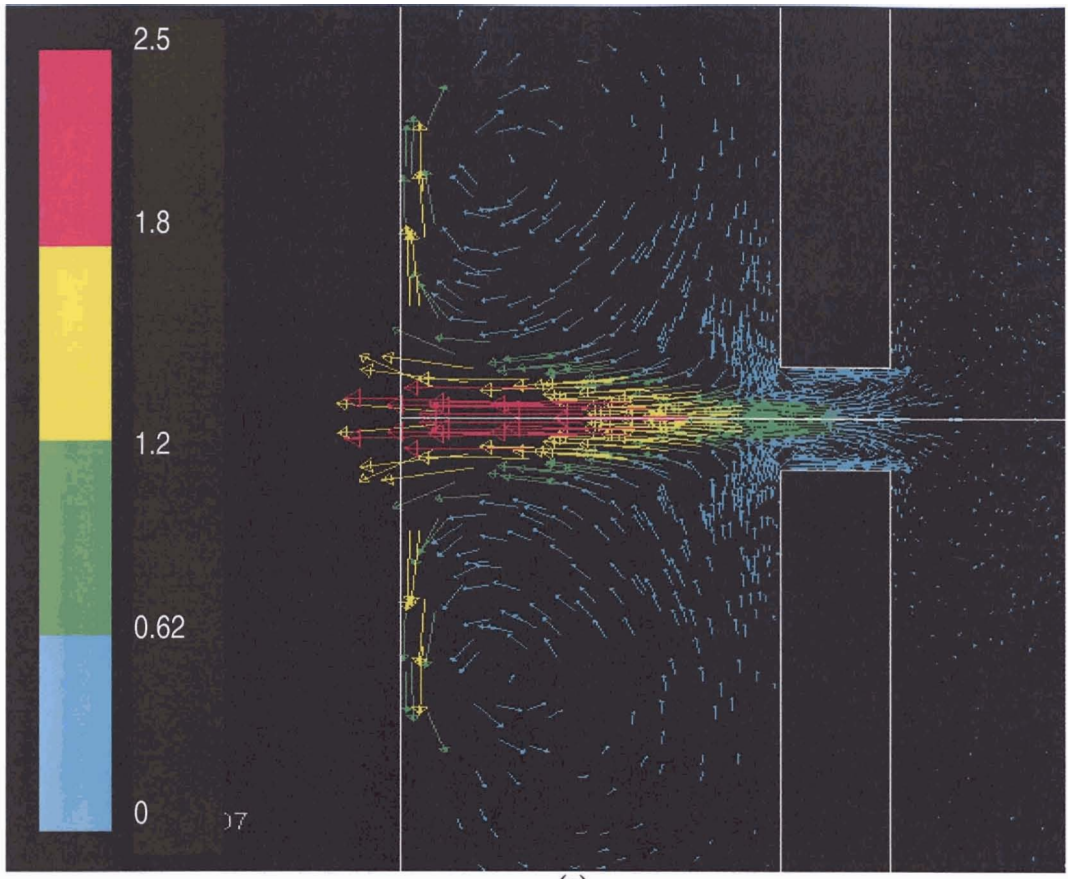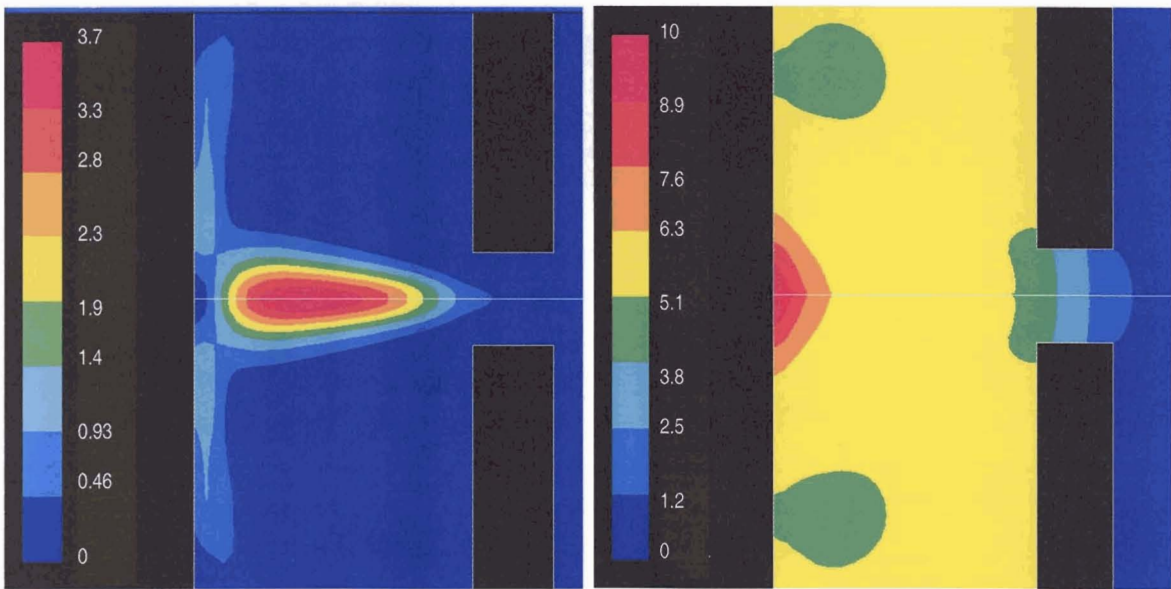
Figure 37 Thunder Cavity II, t=0 Maximum Volume(a) Velocity Vectors (m/s); (b) Contour Plots of Dynamic Pressure (Pa); (c) Contour Plots of Static Pressure (Pa)
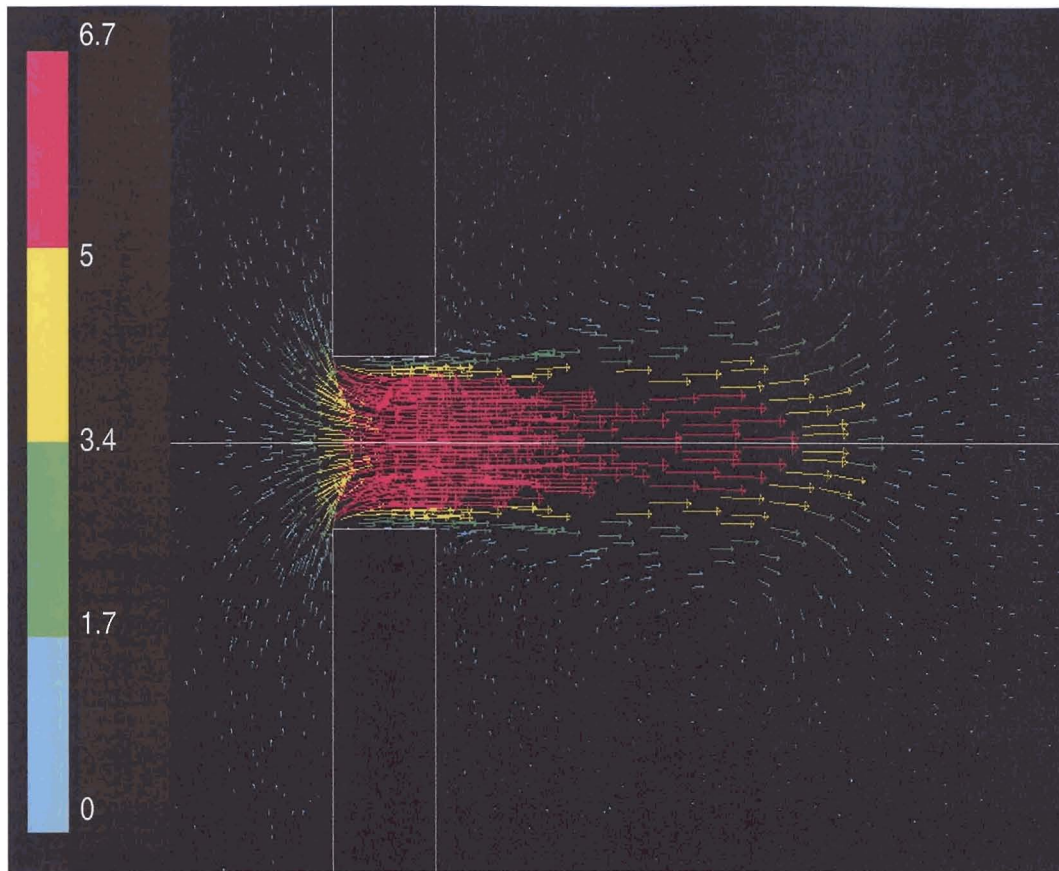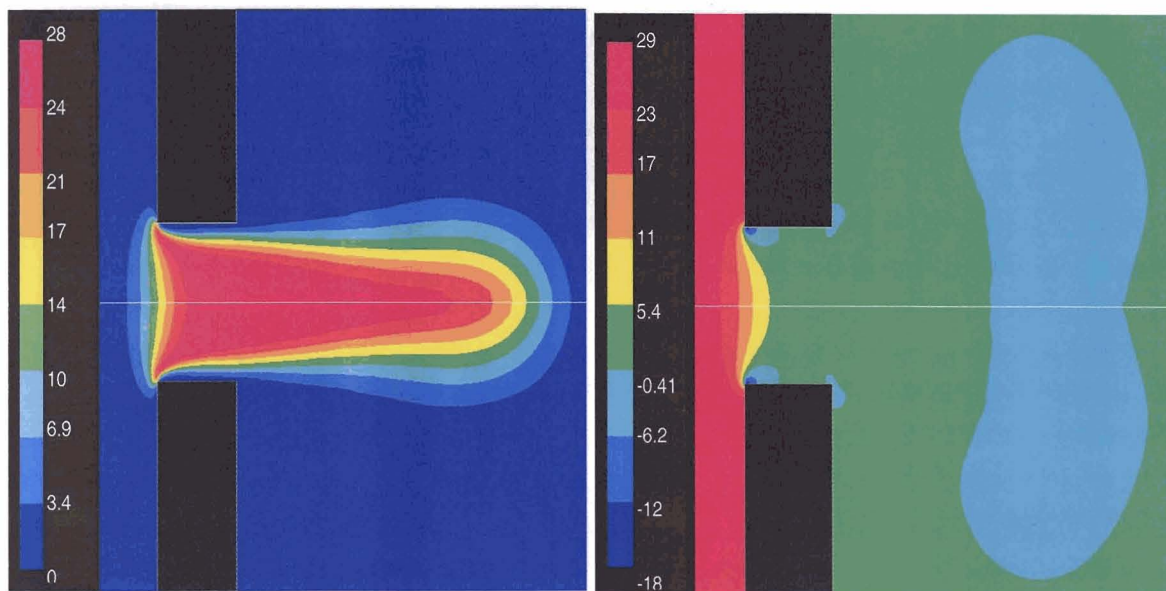
Figure 38 Thunder Cavity II, t=0.25T Maximum Expulsion (a) Velocity Vectors (m/s); (b) Contour Plots of Dynamic Pressure (Pa); (c) Contour Plots of Static Pressure (Pa)
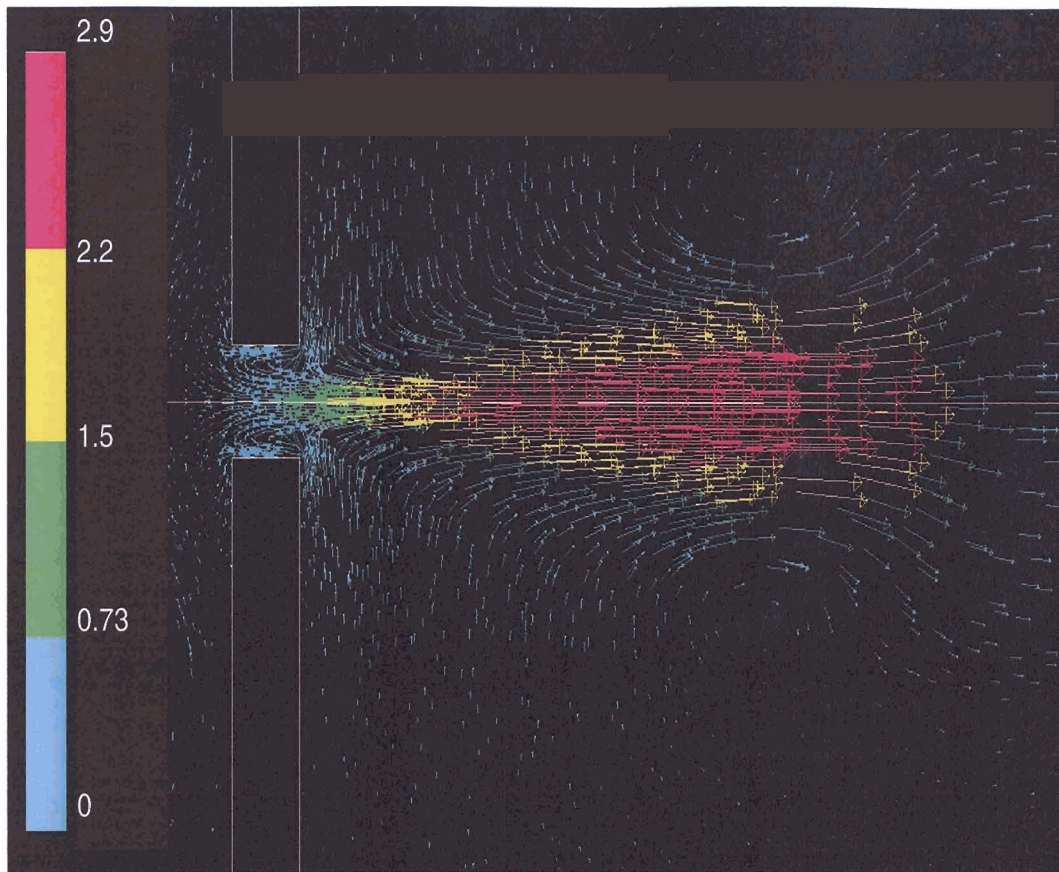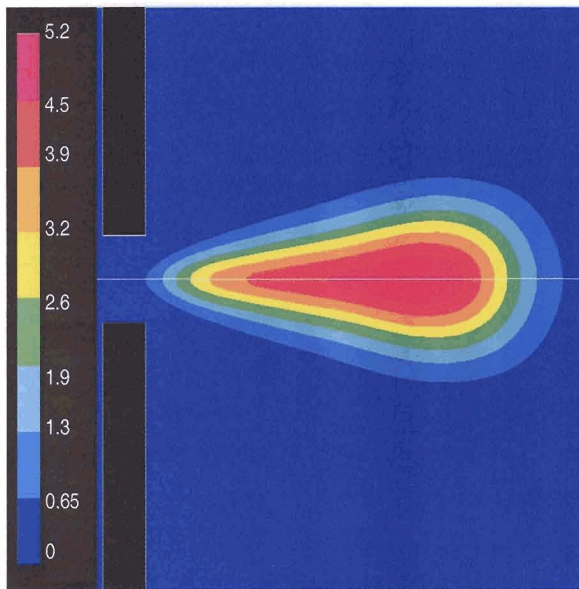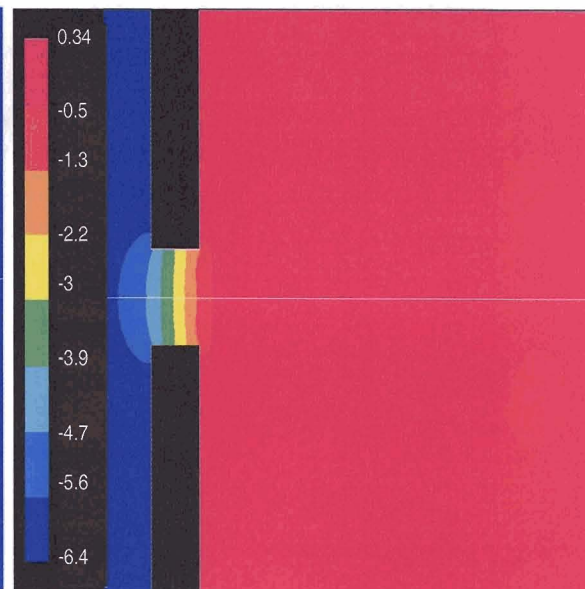
Figure 39 Thunder Cavity II, t=0.5T Minimum Volume (a) Velocity Vectors (m/s); (b) Contour Plots of Dynamic Pressure (Pa); (c) Contour Plots of Static Pressure (Pa)
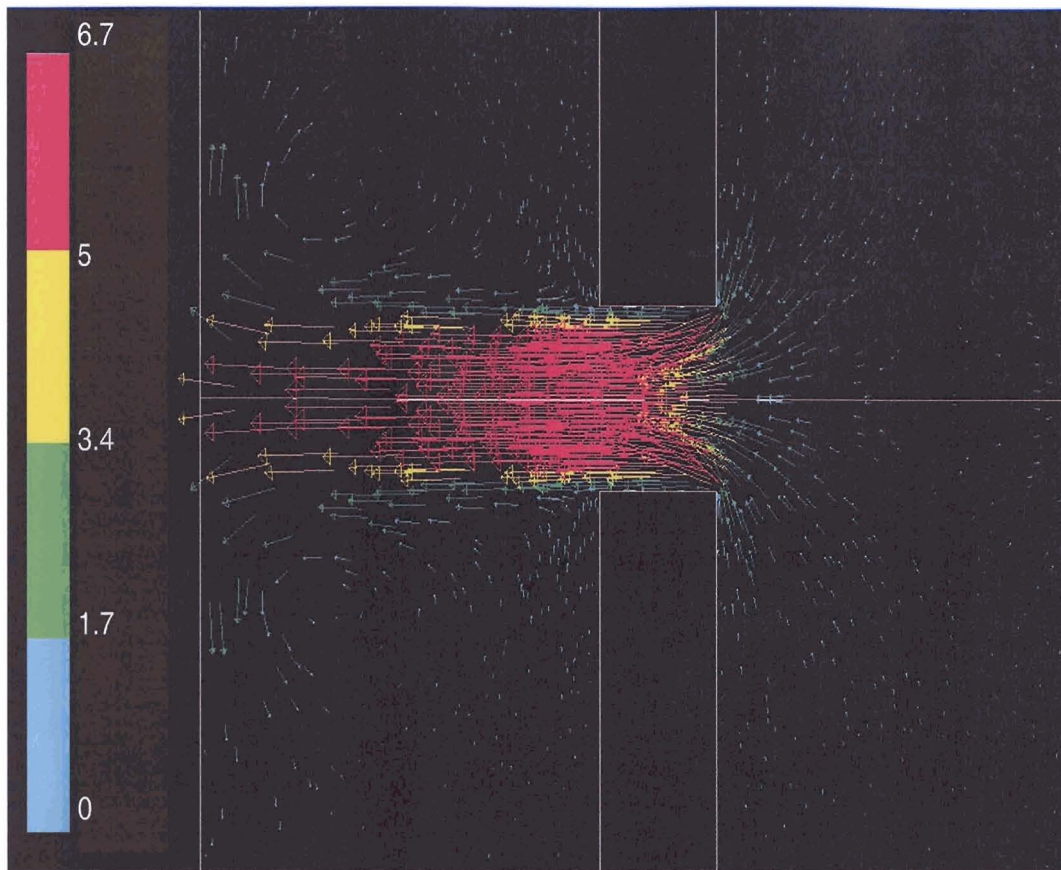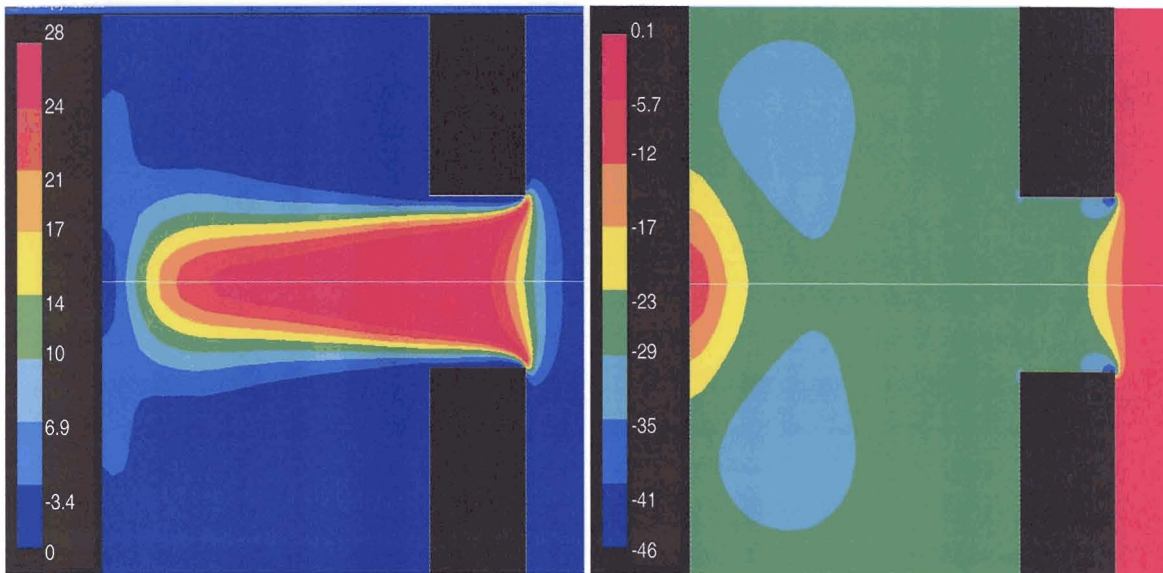
Figure 40 Thunder Cavity II, t = 0.75T Maximum Ingestion (a) Velocity Vectors (m/s); (b) Contour Plots of Dynamic Pressure (Pa); (c) Contour Plots of Static Pressure (Pa)

For the Thunder Cavity II, Figures 41a and 41b show the maximum measured experimental and numerical velocity versus radial position at an axial distance of 2mm, a frequency of 50Hz, for the logarithmic and parabolic diaphragm profile displacement respectively.
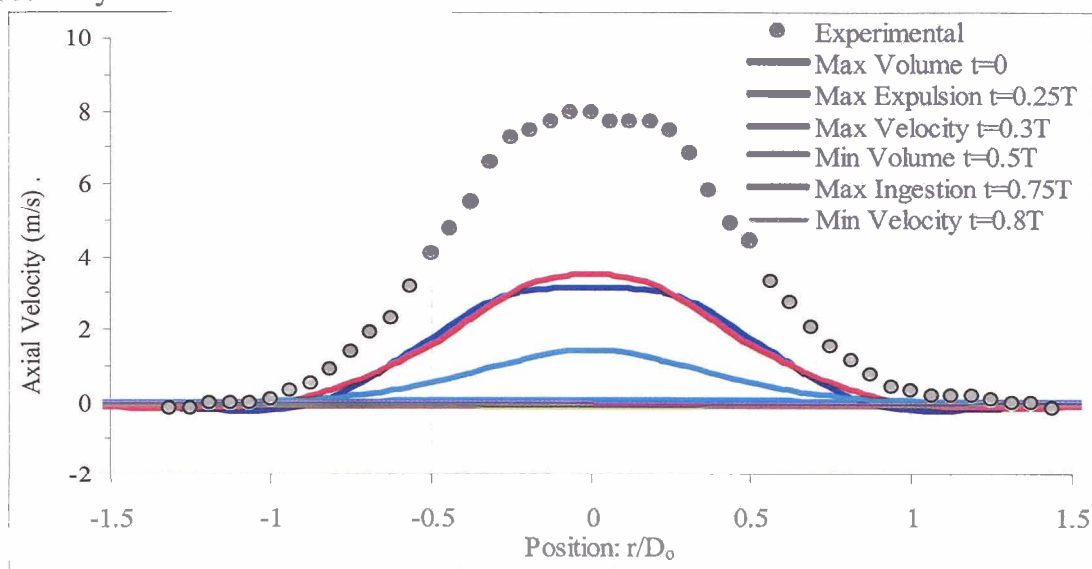
(a)
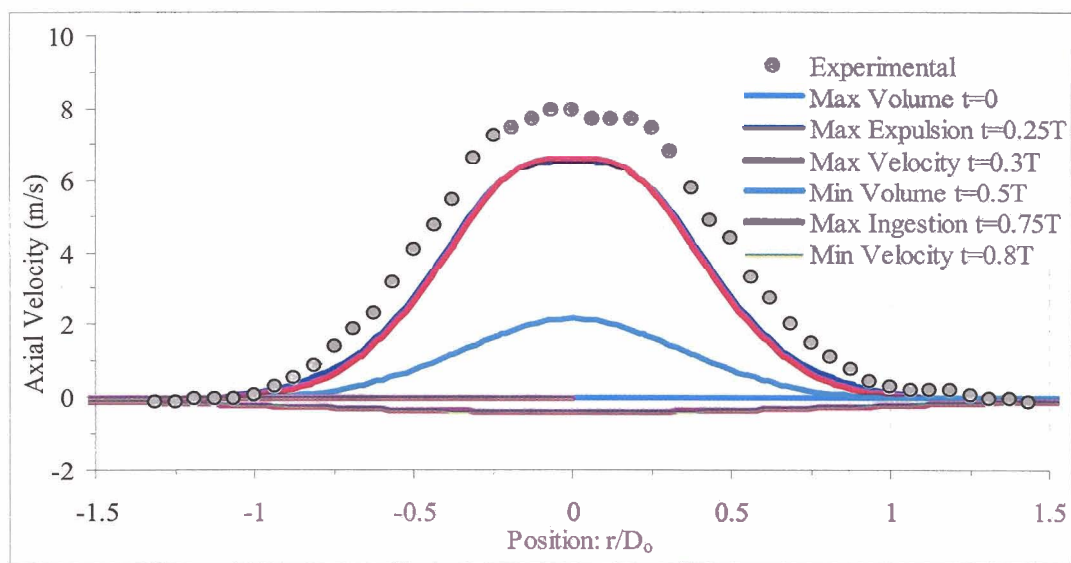
(b)

Figure 41 Thunder Cavity II: Velocity vs. Radial Position at z=2mm for a) Logarithmic model, b) Parabolic model.

Both diaphragm velocity profiles show that, logarithmic and parabolic numerical velocity values under predict the measured experimental value. The parabolic profile however gives a better approximation under predicting the experimental maximum velocity by approximately 13%, while the logarithmic profile under predicts the maximum velocity by 50%.

The two asymmetrical parabolic displacements models that account for the Thunder shape in which the peak-to-peak displacement, δ_C = 0.07mm, is entirely away from the orifice or toward the orifice. As tested in section 4.3.1 for cavity I, the model is also tested for the cavity II configuration. This modification to the diaphragm movement is accomplished by simply using Equations 44 and 45.

In the case when the entire movement is away from the orifice the diaphragm begins at the level position of minimum volume, t = 0, it then moves away from the orifice and reaches the maximum ingestion at t = 0.25T, which corresponds when the diaphragm is moving with maximum velocity away from the orifice. At t = 0.5T the diaphragm reaches the lowest point, maximum volume, with a center distance of 0.07mm below the level point. The maximum expulsion occurs at t = 0.75T when the diaphragm is moving with maximum velocity towards the orifice before returning to the level position at t = 1T or minimum volume.

In the case when the entire movement is toward the orifice the diaphragm begins at the level position maximum volume, t = 0, it then moves toward the orifice and reaches the maximum expulsion point, t = 0.25T, at which the diaphragm is moving with maximum

velocity toward the orifice, at t = 0.5T. The diaphragm reaches the highest point or minimum volume, with a center distance of 0.07mm above the level point. The maximum ingestion occurs at t = 0.75T when the diaphragm is moving with maximum velocity away from the orifice before returning to the level position at t = 1T or maximum volume.

Velocity versus radial position plots, Figures 42a and 42b respectively, show the for the case in which the diaphragm is moving away from the orifice [(-)Parabolic)] and when it is moving toward the orifice [(+)Parabolic]. As opposed to cavity I it appears that neither the (+)Parabolic nor the (-)Parabolic profiles give any better approximation to the experimental values of the Thunder actuator in the cavity II configuration giving the exact same values as the regular parabolic profile.
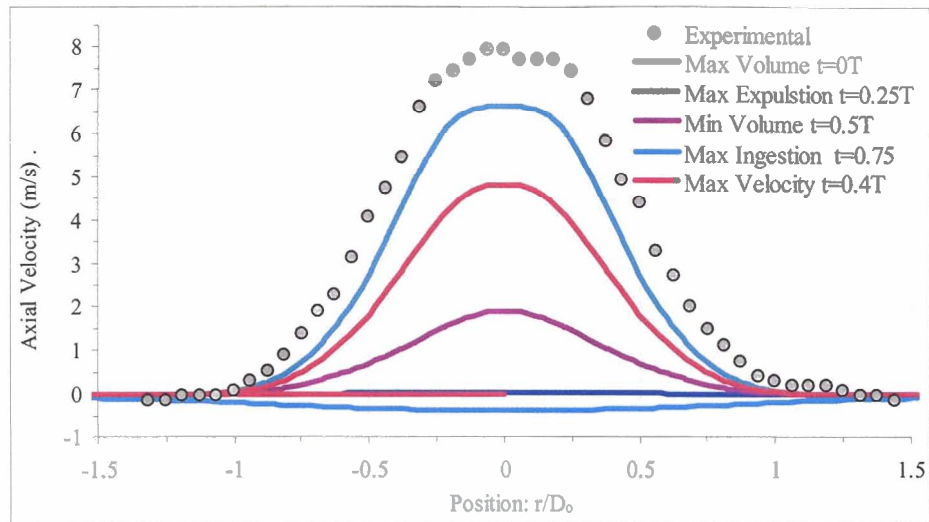
(a)
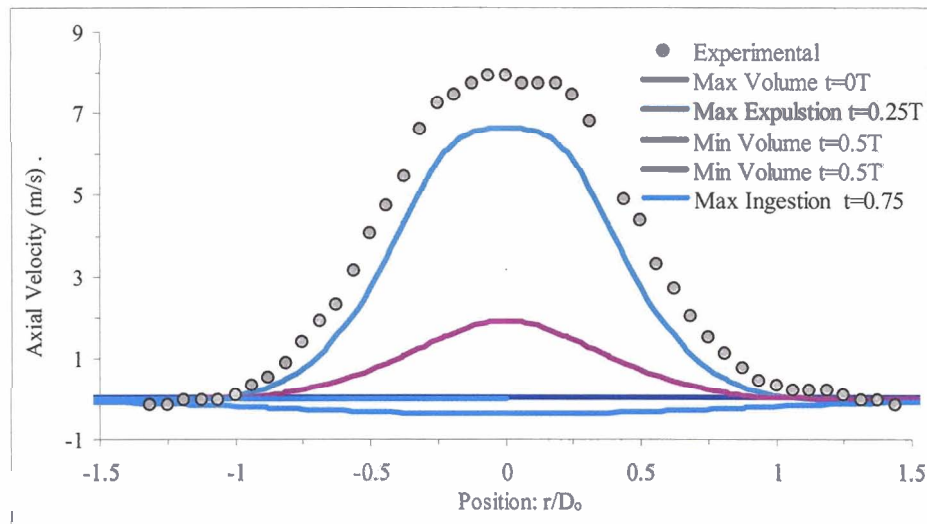
(b)

Figure 42 Thunder Cavity II: Velocity vs. Radial Position at z=2mm for a) Moving away from orifice Parabolic model and b) Moving toward orifice parabolic model.

A complete cycle for the center velocity (r = 0) at an axial distance of 2mm for 32Hz and 50Hz for the Cavity I configuration are shown in Figures 43a and 43b respectively.
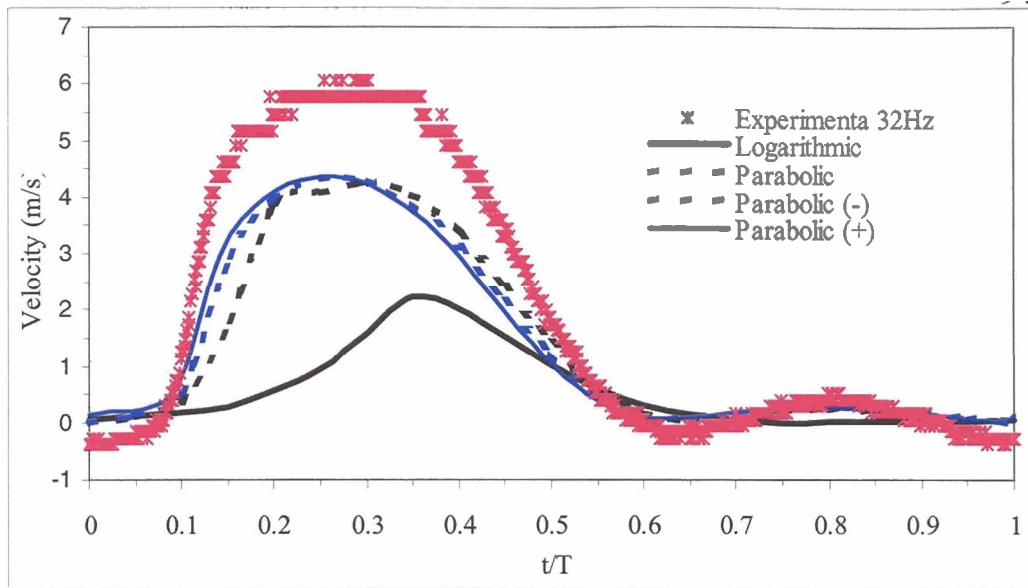
(a)
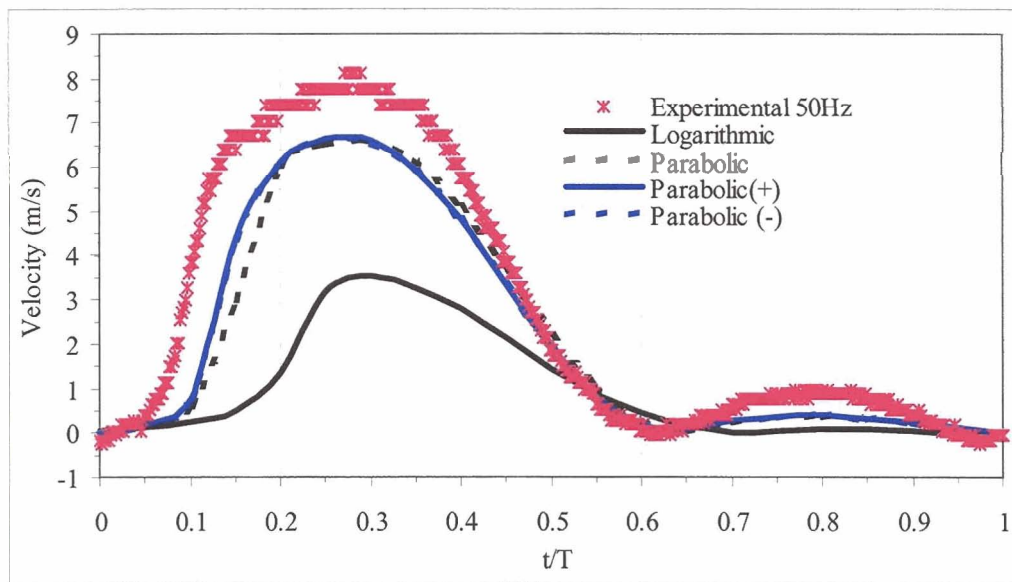
(b)

Figure 43 Thunder Cavity II: Logarithmic and parabolic diaphragm profiles center velocity vs. time comparison at z=2mm for a) 32Hz and b) 50Hz.

The maximum center velocity versus frequency at an axial distance of 2mm is shown in Figure 44 for the Thunder actuator in the cavity II configuration. Similar to the cavity I configuration both the logarithmic and parabolic profile under predict the experimentally measured velocity values for all tested frequencies. The parabolic profile

however is much more accurate for the Thunder in the cavity II configuration than in the

cavity I configuration under predicting the experimental values by less than 20%.
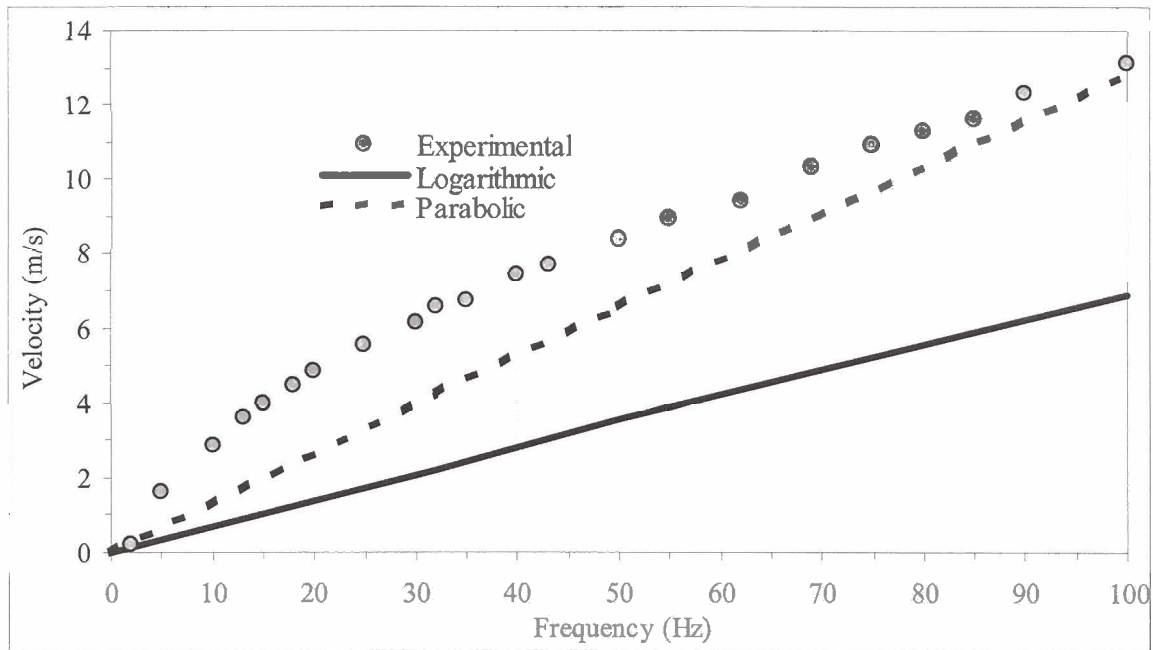
Figure 44 Thunder Cavity II: Logarithmic and parabolic diaphragm profile max center velocity vs. frequency comparison at z=2mm.

4.5 Governing Parameter Calculations

The calculated governing parameters described in section 2.4 for all tested cavity

configurations are shown below in Table 3.

Table 3: Governing parameter measured and calculated numerical values

Cavity Configuration	Orifice Diameter (mm)	Slug Length (mm)	Average Velocity (m/s)	Reynolds (Re)	Stokes (S)	Strouhal (St)	1/Strouhal (Re/S^2)
Control Case Laminar	5.0	6.0	0.6	207.6	23.3	2.6	0.38
Control Case Turbulent	5.0	10.0	1.0	346.0	23.3	1.6	0.64
Bimorph Cavity I Logarithmic	3.67	16.6	1.7	421.6	17.1	0.7	1.44
Bimorph Cavity I Parabolic	3.67	33.0	3.3	837.1	17.1	0.3	2.86
Bimorph Cavity II Logarithmic	2.0	30.4	3.0	420.8	9.3	0.2	4.84
Bimorph Cavity II Parabolic	2.0	42.6	4.3	589.6	9.3	0.1	6.78
Thunder Cavity I Logarithmic	3.7	2.6	0.3	66.0	17.1	4.4	0.23
Thunder Cavity I Parabolic	3.7	4.8	0.5	121.9	17.1	2.4	0.42
Thunder Cavity II Logarithmic	2.0	11.0	1.1	152.2	9.3	0.6	1.75
Thunder Cavity II Parabolic	2.0	21.3	2.1	294.8	9.3	0.3	3.39

For each cavity configuration the stroke length L_o defined by equation 30 was directly measured from the vector plots at the minimum volume, t = 0.5T, which corresponds to the end of the ejection cycle. The averaged spatial and time averaged velocity defined by equation 33 was used to determine the Reynolds number and subsequent dimensionless governing parameters. From the jet formation criterion of equation 39, for an axisymmetric orifice, Re/S^2 greater than 0.16, it can be seen that all

configuration are above the jet formation threshold. The Thunder in cavity I logarithmic

configuration has the lowest Re/ S^2 value at 0.23.

Chapter 5 Conclusions and Recommendations

5.1 Summary

In this study 2D-axisymmetrical numerical simulations of two synthetic jet cavities with a circular orifice were conducted. The numerical modeling utilized a moving boundary condition with two oscillating deflection profiles, parabolic and logarithmic, applied to the diaphragm. The code was validated through the use of a control case in a laminar and turbulent flow with a logarithmic actuator displacement profile.

The two synthetic jet cavities utilized on the simulations were of different cavity height and orifice diameter. For both of these cavities, a parabolic and logarithmic profile was tested with the turbulent RNG $\kappa - \varepsilon$ numerical model.

The actuators modeled where a typical Bimorph and a Thunder piezoelectric device. The initial conditions for the actuators needed for the numerical computations were measured through experiments, with a resulting center peak-to-peak displacement of 0.396mm and 0.07mm respectively when driven with a sinusoidal wave input. Numerical results for the three cavity configurations were compared to experimental results.

Although the velocity boundary numerical model gave overall better results than the current moving-boundary numerical model, the moving-boundary model is more accurate since it better approximates the movement of the diaphragm. From an optimizing viewpoint the moving boundary is more suitable to attempt to optimize the design since the displacement magnitude of the diaphragm can be measured directly from experiments.

It was observed that for the same peak-to-peak center displacement, the parabolic profile produces higher velocity values than the logarithmic profile. For the higher displacement control case and Bimorph actuator, a logarithmic profile gave comparable results to the experimentally measured values whereas the parabolic profile gave better numerical results for the relatively small displacement Thunder actuator. It is thus hypothesized that both tested actuators, Bimorph and Thunder, oscillate according to the specified logarithmic and parabolic profile respectively. It is also theorized that regardless of actuator used the displacement profile will depend on the amplitude of the actuator. For small displacement as was the case for Thunder the profile will be parabolic and for relatively large displacement actuators such as Bimorph the profile will be logarithmic with a transition phase somewhere in between. One way to test this hypothesis is to force the Bimorph displacement to match that of the Thunder and determining which profile, parabolic or logarithmic, gives better results.

Cavity height was briefly investigated for the control case cavity. It was found that doubling and halving the cavity height of the control case cavity did not make any difference to the velocity profiles for either laminar or turbulent model. Cavity height was also varied for the Bimorph actuator by exchanging the cavity height of cavities I and II while maintaining all other parameters the same. This exchange in cavity height also revealed that cavity height did not make a difference in the centerline velocity for the numerical model. Experimental results however do show that cavity height does have an effect on the jet velocity which suggests that the two dimensional model which only accounts for the cavity height and not the cavity volume. Another important effect that the

model fails to consider is the dynamic coupling of the actuator displacement and the pressure that develops inside which as shown in section 4.3. The pressure values obtained are comparable to the blocking pressure for the Bimorph in the cavity I configuration during maximum expulsion and maximum ingestion. A thorough investigation of the effects of cavity height and dynamic coupling of the actuator displacement and pressure will be necessary to make any final conclusions regarding the effects if any of cavity height or volume.

The results of this study showed that jet formation and development had unique characteristics for each actuator and cavity configuration. The smaller orifice, cavity I, configuration produced a faster, longer, thinner jet with larger vortices than the bigger orifice, cavity II, configuration. During max expulsion, t = 0.25T, and max ingestion, t = 0.75T, a low pressure area localized at the corners of the orifice inlet and exit respectively were observed. All cavity configurations passed all three known jet formation criterions that include; Smith et al. Lo/Do > 1, Wu and Breuer Re > 50, and Utturkar et al. Re/S^2 > 0.16.

5.2 Recommendations

A thorough investigation of the effects of cavity height and dynamic coupling of the actuator displacement and pressure will be necessary before the current developed CFD model can be implemented for optimization purposes. Experimental and physics based work is in progress to describe the shape and displacement of piezoelectric actuators. This work can be coupled with CFD codes to provide results comparable to experimental work.

Since only one turbulence model was tested in this study, further testing should include the different turbulent models available. Variations of the FLUENT detail parameters such as turbulence dissipation and under relaxation parameters are also necessary to fine-tune the current model. Furthermore more computation power to develop a 3D model to account for actuator shape and complex actuator deformation will be ideal in attempting to optimize the synthetic jet cavity design.

Appendix ASizing Functions

Control Case Cavity
    Size Function 1:
        Source: Orifice Edge
            Start size: 0.0001
            Growth Rate: 1.1
    Size Function 2:
        Source: Orifice Vertex
            Start size: 0.0001
            Growth Rate: 1.04
    Size Function 3:
        Source: Cavity Vertex
            Start size: 0.05
            Growth Rate: 1.05

Cavity I
    Size Function 1:
        Source: Orifice Edge
            Start size: 0.0001
            Growth Rate: 1.05
    Size Function 2:
        Source: Orifice Vertex
            Start size: 0.0001
            Growth Rate: 1.04
    Size Function 3:
        Source: Cavity Vertex
            Start size: 0.05
            Growth Rate: 1.05

Cavity II
    Size Function 1:
        Source: Orifice Edge
            Start size: 0.0001
            Growth Rate: 1.1
    Size Function 2:
        Source: Orifice Vertex
            Start size: 0.0001
            Growth Rate: 1.03
    Size Function 3:
        Source: Cavity Vertex
            Start size: 0.05
            Growth Rate: 1.05

Appendix B Cavity Mesh Parameters

Control Case Cavity
Total Mesh nodes: 7398
Total Mesh Faces: 14302
Domain Extents:
  x-coordinate: min (m) = 0.000000e+00, max (m) = 1.150000e-01
  y-coordinate: min (m) = 0.000000e+00, max (m) = 5.000000e-02
Volume statistics:
  minimum volume (m3): 9.593898e-12
  maximum volume (m3): 3.706291e-06
   total volume (m3): 8.014007e-04
  minimum 2d volume (m3): 4.037358e-09
  maximum 2d volume (m3): 1.225074e-05
Face area statistics:
  minimum face area (m2): 1.684287e-08
  maximum face area (m2): 2.749890e-04

Cavity I
Total Mesh nodes: 16504
Total Mesh Faces: 32206
Domain Extents:
  x-coordinate: min (m) = 0.000000e+00, max (m) = 9.515000e-02
  y-coordinate: min (m) = 1.000000e-06, max (m) = 6.000100e-02
Volume statistics:
  minimum volume (m3): 7.632626e-13
  maximum volume (m3): 7.562529e-07
   total volume (m3): 9.770701e-04
  minimum 2d volume (m3): 1.239401e-09
  maximum 2d volume (m3): 2.117581e-06
Face area statistics:
  minimum face area (m2): 4.166116e-09
  maximum face area (m2): 1.332419e-04

Cavity II
Total Mesh nodes: 17400
Total Mesh Faces: 34008
Domain Extents:
  x-coordinate: min (m) = 0.000000e+00, max (m) = 1.071000e-01
  y-coordinate: min (m) = 1.000000e-06, max (m) = 5.000100e-02
Volume statistics:
  minimum volume (m3): 2.211151e-13
  maximum volume (m3): 6.484106e-07
   total volume (m3): 8.009865e-04
  minimum 2d volume (m3): 8.904167e-10
  maximum 2d volume (m3): 2.406125e-06
Face area statistics:
  minimum face area (m2): 1.820004e-09
  maximum face area (m2): 1.157742e-04

Appendix C Viscous Model Options

1) **Inviscid:**
2) **Laminar:**
3) **Sparlart—Allmaras:**
   - One-equation model that solves a modeled transport equation for the kinematic eddy (turbulent) viscosity. No length scale related to local shear layer thickness
   - Specifically designed for aerospace applications involving wall-bounded flows (relatively new)
   - Uses Boussinesq Approx: model treats density as a constant value in all solved equations, except for the buoyancy term in the momentum equation

4) **Turbulent kinetic energy—Dissipation rate ($\kappa - \varepsilon$) Model: 3 Options**
   - 2 Equations. Simplest "complete models" of turbulence
   - Solution of two separate transport equations allows the turbulent velocity and length scales to be independently determined
   - **Standard $\kappa - \varepsilon$ (proposed by Launder and Spalding)**
     - o Semi-empirical model (κ model transport equation derived from exact ε equation)
     - o High-Reynolds-number model (assumes complete turbulent)
     - o Valid only for fully turbulent flows.
   - **RNG $\kappa - \varepsilon$ "renormalization group"**
     - o Derived using statistical technique (renormalization group theory).
     - o Has an additional term in its ε equation that significantly improves the accuracy for rapidly strained flows
     - o Effect of swirl included in turbulence.
     - o Has analytical formula for turbulent Prandtl numbers.
     - o Provides an analytically-derived differential formula for effective viscosity that accounts for low-Reynolds-number effects (Needs appropriate treatment of the near-wall region)
     - o Differential Viscocity: Option for a differential formula for effective viscosity
   - **Realizable $\kappa - \varepsilon$**
     - o Model satisfies certain mathematical constraints on the Reynolds stresses, consistent with the physics of turbulent flows (2 other models do not)
     - o Contains a new formulation for the turbulent viscosity.
     - o A new transport equation for the dissipation rate, ε, from exact equation for voticity fluctuation.
     - o More accurately predicts the spreading rate of both planar and round jets
     - o Initial studies have shown that the realizable model provides the best performance of all the $\kappa - \varepsilon$ models.

- o Includes effects of mean rotation in turbulent viscocity—not desired for multiple reference frame.

5) Kinetic energy—specific turbulence dissipation ($\kappa - \omega$) 2 Options

- **Standard $\kappa - \omega$** (based on the Wilcox $\kappa - \omega$ model)
  - o Shear flow corrections: Specifies whether corrections that improve the accuracy in predicting free shear flows should be included
  - o Predicts free shear flow spreading rates that are in close agreement with measurements for far wakes, mixing layers, and plane, round, and radial jets

- **Shear Stress Transport (SST) $\kappa - \omega$** (developed by Menter)
  - o Blends the robust and accurate formulation of the $\kappa - \omega$ model in the near-wall region with the free-stream independence of the k- ϵ model in the far field through a blending function
  - o Incorporates a damped cross-diffusion derivative term in the ω equation
  - o Transitional Flows: specifies whether or not a low-Reynolds-number correction to the turbulent viscosity should be included. (Both Models)
  - o Turbulent viscosity is modified to account for the transport of the turbulent shear stress

6) Reynolds-averaged Navier-Stokes (RANS)

- Reynolds stress model (RSM) is the most elaborate turbulence model that **FLUENT** provides with 5 equations to solve. No isotropic eddy-viscocity hypothesis ("Most important dynamical quantity affecting the mean motion"--- Gad-el-Hak (p85))
- Requires 50-60% more CPU time per iteration compared to the $\kappa - \varepsilon$ and $\kappa - \omega$ and 15-20% more memory is needed

7) Large Eddy Simulation: (3D only)
- A manipulation of the exact Navier-Stokes equations to remove only the eddies that are smaller than the size of the filter, which is usually taken as the mesh size
- Has been made available for you to try if you have the computational resources and are willing to invest the effort
- Transform the Navier-Stokes equations in such a way that the small-scale turbulent fluctuations do not have to be directly simulated

Appendix D Oscillating Diaphragm UDF Code

```
#include "udf.h"
DEFINE_GRID_MOTION(logarithmic, domain, dt, time, dtime)
{  Thread *tf = DT_THREAD (dt);
  face_t f;
  Node *v;
  real NV_VEC (velocity), NV_VEC (axis);
  real NV_VEC (origin), NV_VEC (rvec);
  real loco;
  real freq;
  real amp;
  real diam;
  int n;
  SET_DEFORMING_THREAD_FLAG (THREAD_T0 (tf));
  freq=50;
  amp=.000396;
  diam=.060001
  loco = 3.141592654 * amp * freq * cos(3.141592654 * 2*freq * time);
  Message ("time = %f, omega = %f\n", time, loco);
  NV_S (velocity, =, 0.0);
  NV_D (axis, =, 0.0, 1.0, 0.0);
  NV_D (origin, =, 0.0, 0.0, 0.0);
  begin_f_loop (f, tf)
    {  f_node_loop (f, tf, n)
      {  v = F_NODE (f, tf, n);
          if (NODE_POS_NEED_UPDATE (v))
          { NODE_POS_UPDATED (v);
velocity[0] = loco * (1-(4*NODE_Y (v)*NODE_Y (v))/(diam*diam)+((8*NODE_Y
(v)*NODE_Y (v))/(diam*diam))*(log((2*NODE_Y (v))/diam)));
          NV_V_VS (rvec, =, NODE_COORD (v), +, velocity, *, dtime);
          NV_V (NODE_COORD (v), =, rvec);  } } }
  end_f_loop (f, tf);}
```

CODE Explanation:

#include "udf.h" #include "*filename*" The file name must reside in current directory. The only exception to is the udf.h file, which is read automatically by **FLUENT**.

DEFINE_GRID_MOTION(logarithmic, domain, dt, time, dtime) This Macro unlike "DEFINE_CG_MOTION()" which allows only for rigid movement (i.e. no relative motion between the nodes in the chosen dynamic zone) DEFINE_GRID_MOTION() has

the capability to control each node independently as a function of node location so that there is relative motion between the nodes (deformation).

Arguments in Macro:

logarithmic = name of UDF (user defined function)

domain = data type is a structure that acts as a container for data associated with a collection of node, face, and cell threads in a mesh

dt = dynamic thread

time = current time

dtime = time step

Thread *tf = DT_THREAD (dt); The Thread data type is a structure that acts as a container for data that is common to the group of cells or faces that it represents.

face_t f; "face_t f" is the data type for a face ID. It is an integer index that identifies a particular face within a given thread.

Node *v; Declare a pointer named v that points to a node value. A pointer is a variable that contains an address in memory where the value referenced by the pointer is stored. In other words, a pointer is a variable that points to another variable by referring to the other variable's address. Pointers contain memory addresses, not values. Pointer variables must be declared in C using the * notation.

real NV_VEC (velocity), NV_VEC (axis); real NV_VEC (origin), NV_VEC (position); real loco; real freq; real amp; real diam; int n; Declare "Velocity", "axis", "origin" and "rvec" as vectors. Declare "loco", "freq", "amp" and "diam" as real variables. Declare variable n as an integer

 SET_DEFORMING_THREAD_FLAG (THREAD_T0 (tf)); Set deforming flag on adjacent cell zone. Allows for relative motion among nodes on diaphragm.

freq = 50; amp = 0.000396;

loco = 3.141592654 * amp * freq * cos(3.141592654 * 2*freq * time);

Set frequency, freq, center peak to peak diaphragm amplitude, amp, and Actuator diameter, diam. Set "loco" equal to the diaphragm velocity dependency on time. All inputs are in SI units (hz, m and m/s).

NV_S (velocity, =, 0.0); s denotes a scalar. (0 at t = 0)

NV_D (axis, =, 0.0, 1.0, 0.0);

 NV_D (origin, =, 0.0, 0.0, 0.0); D denotes a sequence of three vector components of which the third is always ignored for a two-dimensional calculation. (1 for y direction movement)

```
begin_f_loop (f, tf)
f_node_loop (f, tf, n)
v = F_NODE (f, tf, n); Loop through face node values and set each node equal to v

if (NODE_POS_NEED_UPDATE (v))
NODE_POS_UPDATED (v);  Determine if node position needs update or not.

velocity[0] = loco * (1-(4*NODE_Y (v)*NODE_Y (v))/(Diam*Diam)+((8*NODE_Y
(v)*NODE_Y (v))/(Diam*Diam)*(log((2*NODE_Y (v))/Diam)); Incorporate spatial
dependence to achieve proper diaphragm movement by looping through each node on
diaphragm.  V = Loco at y = 0 and V = 0 at y = +-Diam/2. Without this spatial inclusion
every node on face (diaphragm) would move an equal distance similar to a Piston.

NV_V_VS (position, =, NODE_COORD (v), +, velocity, *, dtime);
The utility nv_v_vs adds a vector to another vector that is multiplied by a scalar. Here we
add the velocity vector times the time step to give a displacement quantity and set it equal
to rvec.

NV_V (NODE_COORD (v), =, position); Update v node to new position.

end_f_loop (f, tf); End Code
```

Literature Cited

1. Gad-el-Hak, M., *Flow Control. Passive, Active and Reactive Flow Managemen,t* pp. 1-32, Cambridge University Press, London, United Kingdom, 2000.

2. Amitay, M., and Glezer, A, "Synthetic Jets," *Annu. Rev. Fluid Mech.,* A34, 503–529, 2002.

3. Amitay, M., Kibens, V., Parekh, D., and Glezer, A., "The Dynamics of Flow Reattachment over a Thick Airfoil Controlled Synthetic Jet Actuators," *AIAA 99-1001,* 1999.

4. Amitay, M., Smith, B., and Glezer, A, "Aerodynamic Flow Control Using Synthetic Jet Technology", *AIAA 1998-0208,* 1998.

5. Shaefller, N., Hepner, T., Jones, G., and Kegerise, M., "Overview of Active Flow Control Actuator Development at NASA Langley Research Center", *AIAA 2002-3159,* 2002.

6. Cattafesta, L., Garg, S., Shukla, D., "Development of Piezoelectric Actuators for Active Flow Control", *AIAA Journal, Vol. 39, No. 8,* 2001.

7. Chen, F., and Beeler, G., "Virtual Shaping of a Two-dimensional NACA 0015 Airfoil Using Synthetic Jet Actuator", *AIAA-2002-3273,* 2002.

8. Chen, F., Yao, C., Beeler, G., Bryant, R., and Fox, R., "Development of Synthetic Jet Actuators for Active Flow Control at NASA Langley", *AIAA 2000-2405,* 2000.

9. Crook, A., Sadri, A.M., and Wood, N.J., "The development and Implementation of Synthetic Jets for the Control Separated Flow", *AIAA 99-3176,* 1999.

10. Gilarranz, J.L., and Rediniotis, O.K., "Compact, High-Power Synthetic Jet Actuators for Flow Separation Control", *AIAA-2001-0737,* 2001.

11. Holman R., Gallas, Q., Carroll, B., and Cattafesta, L., "Interaction of Adjacent Synthetic Jets in an Airfoil Separation Application" *AIAA 2003-3709,* 2003.

12. Hong, G., Lee, C., Mallison., S., "A piezoelectrically actuated micro synthetic jet for active flow control", *Sensors and Actuators A,* 108, pp 168–174, 2003.

13. Jenkins, L., Gorton, A., and Anders, S. "Flow Control Device Evaluation for an Internal Flow with an Adverse Pressure Gradient", *AIAA 2002-0266,* 2002.

14. Jones, G., Englar, R., "Advances in Pneumatic-Controlled High-Lift Systems Through Pulsed Blowing", *AIAA 2003-3411,* 2003.

15. Kiddy, J., Chen, P., and Niemczuk, J., "Active Flow Control Using Microelectromechanical Systems", *AIAA SDM Conference,* 2000.

16. Morel-Fatio, S., Pines, D., "UAV Performance Enhancements with Piezoelectric Synthetic Jet Actuators", *AIAA 2003-394,* 2003.

17. Smith, B., and Swift, G., "A Comparison Between Synthetic Jets and Continuous Jets", *Experiments in Fluids,* 34 467-472, 2003.

18. Smith, B., and Swift, G., "Synthetic Jets at Large Reynolds Number and Comparison to Continuous Jets", *AIAA 2001-3030,* 2001.

19. Whitehead, J.A. and Gursul, I,. "Aerodynamics and Propulsion of Synthetic Jet Based Micro Air Vehicles", *AIAA 2003-4004,* 2003.

20. Bryant, R., Effinger, R., IV, Isaiah A, Jr., Copeland, B., Covington, E., III, and Hogge, J., "Radial Field Piezoelectric Diaphragms", *Journal of Intelligent Material Systems and Structures,* 15, 527 – 538, 2004

21. Hyer, M., and Schultz, M., "A Morphing Concept Based on Unsymmetric Composite Laminates and Piezoceramic MFC Actuators", *AIAA-2004-1806,* 2004.

22. Mossi, K., Bryant, R., "Characterization of Piezoelectric Actuators for Flow Control Over a Wing", *Actuator,* pp. 181–185, Germany 2004

23. Mossi, K., Bryant, R., "Synthetic Jets for Piezoelectric Actuators" *Materials Research Society,* pp. 407–412, 2004

24. Mossi, K., Selby, G., and Bryant, R., "Thin-Layer Composite Unimorph Ferroelectric Driver and Sensor Properties", *Materials Letters,* 35, pp 39– 49, 1998.

25. Mallinson, S.G., Reizes, J.A., Hong, G., and Wesbury, P.S., "Analysis of Hot-Wire Anemometry Data Obtained in a Synthetic Jet Flow", *Experimental Thermal and Fluid Science,* 28, 265–272, 2004.

26. Muller, M., Bernal, L., Miska, P., Washabaugh, P., Chou, T.K., Parviz, B., Zhang, C., and Najafi, K., "Flow Structure and Performance of Axysimmetric Synthetic Jets", *AIAA-2001-1008,* 2001

27. Yao, C., Chen, F.J., Neuhart, Dan., and Harris Jerome, "Synthetic Jet Flow Field Database for CFD Validation", *AIAA 2004-2218,* 2004.

28. Ye, T., Mittal, R., Udaykumar, H.S., and Shyy, W., "An Accurate Cartesian Grid Methods for Viscous Incompressible Flows with Complex Immersed Boundaries", *Journal of Computational Physics,* 156, 209 – 240, 1999.

29. Zhong, S., Garcillan, L., Porkusevski, Z., and Wood, N., "A PIV study of synthetic jets with different orifice shape and orientation", *AIAA, 2004-2213,* 2004

30. Rumsey, C.L., Gatski, B., Sellers, W.L., Vatsa, V., and Viken A., "Summary of the 2004 CFD Validation Workshop on Synthetic Jets and Turbulent Separation Control", *AIAA 2004-2217,* 2004.

31. Timoshenko, S., *Theory of Plates and Shells,* Second Edition, New York: McGraw-Hill, 1959.

32. Utturkar, Y., Holman, R., Mittal, R., Carroll, B., Sheplak, M., and Cattafesta, L., "A jet formation Criterion for Synthetic Jet", *AIAA 2003-0636,* 2003

33. Wu, K. and Breuer, K, "Dynamics of Synthetic Jet Actuator Arrays for Flow Control", *AIAA 2003-4257*, 2003

34. Yamaleev, N., Carpenter, M., "A Reduced-Order Model for Efficient Simulation of Synthetic Jet Actuators", *NASA/TM-2003-212664*, 2003.

35. Ye, T., Mittal, R., Udaykumar, H.S., and Shyy, W., "An Accurate Cartesian Grid Methods for Viscous Incompressible Flows with Complex Immersed Boundaries", *Journal of Computational Physics*, 156, 209-240, 1999.

36. Fugal, S., Smith, B,. and Spall, R., "A Numerical Study of 2-D Synthetic Jet Formation", Proceedings of HT-FED 2004, HT-FED2004-56854

37. Kotapati, R., and Mittal Rajat., "Time-Accurate Three-Dimensional Simulations of Synthetic Jets in Quiecent Air", *AIAA 05-0103*, 2005.

38. Mallinson, S.G., Kwok, C.Y., and Reizes, J.A., "Numerical Simulation of Micro-Fabricated Zero Mass-Flux Jet Actuators", *Sensors and Actuators A*, 105, 229-236 2003

39. Mittal, R,. and Rampunggoon, "Interaction of a Synthetic Jet with a Flat Plate Boundary Layer"., *AIAA 2001-2773*, 2001.

40. Mittal, R., "On the Virtual Aeroshaping Effect of Synthetic Jets", *Physics of Fluids*, Vol. 14 (4), 2002.

41. Rathnasingham, R, Breuer, K. S. "Coupled fluid-structural characteristics of actuators for flow control" *AIAA J.*, 35, 832-837, 1997.

42. Ravi, B.R., and Mittal, R, "Study of Three Dimensional Synthetic Jet Flowfields Using Direct Numerical Simulation", *AIAA 2004-0091*, 2004.

43. Rizzetta, D. P., Visbal, M. R., and Stanek, M. J., "Numerical Investigation of Synthetic Jet Flowfields," *AIAA 98-2910*, 1998.

44. Suryanarayana, A.N., Sankar, B., Gallas, Q., Wang, G., Sheplak, M., and Cattafesta, L., "Two-Port Electroacoustic Model of an Axisymmetric Piezoelectric Composite Plate", *AIAA 2003-0635*, 2003.

45. Tang, H., and Zhong, S., "Development of a Prediction Model for Synthetic Jets in Quiescent Conditions", *AIAA 2005-104*, 2005.

46. Timoshenko, S., *Theory of Plates and Shells*, Second Edition, New York: McGraw-Hill, 1959.

47. FLUENT Inc. www.fluent.com

48. Mane, P., "Characterization of Piezoelectric Synthetic Jets", MS Thesis, In Progress.

49. http://www.captron.com.au/Piezoelectric/piezoelectric.html